AECL EACL

AECL-11234, PR-PHY-8

Progress Report
Physical and Environmental Sciences
Physics Division

1994 January 1 to December 31

September 1995 septembre

AECL

PHYSICS DIVISION

Progress Report

1994 January 1 - December 31

edited by M. Harvey

The results and conclusions given here are not classified or restricted in any way; however, some of the information is of a preliminary nature. Readers interested in using the information in their own research are invited to consult with the contributors for further details. Copies of AECL publications referred to in this report may be purchased by writing to the Scientific Document Distribution Office, Chalk River Laboratories, Chalk River, ON, K0J 1J0.

Chalk River, Ontario

1995 September

AECL-11234

AECL

PROGRESS REPORT

PHYSICAL AND ENVIRONMENTAL SCIENCES

PHYSICS DIVISION

1994 January 1 - December 31

PR-PHY-8

Chalk River Laboratories
Chalk River, Ontario K0J 1J0

1995 September

AECL-11234

CONTENTS

AECL

PHYSICAL AND ENVIRONMENTAL SCIENCES
PHYSICS DIVISION

STAFF LIST

1994 JANUARY 1 - December 31

Vice-President, Physical Sciences	G. Dolling*
Vice-President, Physical and Environmental Sciences	C.J. Allan**
Executive Assistant, Physical Sciences	M.E. Humphries*
Executive Administrative Assistant, Physical Sciences	T. Ingram*
Executive Administrative Assistant, Physical and Environmental Sciences	G. McAuley**
Director, Physics Division	M. Harvey
Administrative Assistant, Physics Division	J. Vaudry

* Prior to 1994 March 31, Physics Division was part of the Physical Sciences Organizational Unit

** From 1994 April 1 Physics Division was part of the newly created Physical and Environmental Sciences Unit.

PHYSICS DIVISION SUMMARY

This report marks the change from biannual to annual reports recording technical developments in Physics Division. During this period, AECL has continued with its restructuring program, with Physics Division now included in an expanded Physical and Environmental Sciences Unit. The Division itself remains unchanged, with major activities on neutron scattering, the Sudbury Neutrino Observatory and developments and applications of accelerator technology.

A highlight of 1994 was the award of the Nobel Prize in Physics to Bertram Brockhouse, jointly with Cliffort Schull of the USA. Dr. Brockhouse did his seminal work in neutron scattering during the period 1952 to 1962 first at NRX and then at NRU before moving to McMaster University. As if to emphasize that the group Dr. Brockhouse founded is still flourishing, Dr. Tom Holden was awarded the Innovative Achievement Award of the Canadian Nuclear Society for his pioneering work in applying neutron scattering to industrial problems in materials science. In this report we record the many facets of neutron scattering in condensed matter science, molecular science, materials science and accompanying theory. This work has been done in collaboration with over seventy external researchers (twenty-four students) from twenty-three university and industrial research organizations. In addition, there were nineteen participants at the Workshop on Neutron Diffraction in May (1994) and thirty-four in the Neutron Applications in Materials Science and Engineering Workshop in August (1994). All together testament to the growth of neutron scattering.

In preparation for construction of the detector for the Sudbury Neutrino Observatory, the AECL group has continued with their neutron activation analyses to qualify the acrylic of which the heavy-water container is made. Work has also progressed on techniques to determine the radioactive background in the detector through a purification process of the light and heavy water. The AECL group has also joined the software group in preparation for data taking and ultimate interpretation. Data taking is expected to start in early 1997.

The accelerator physics group has initiated a program to upgrade the PHELA and IMPELA accelerators so that they can be operated unattended. Such a mode of operation is necessary to address the long radiation times needed for materials and fuels research in support of the CANDU® business. A study is under way to determine modifications necessary to convert an IMPELA® to a free electron laser (FEL), with identification of the customers who would use the far-infrared radiation.

In the Laser Plasma Beatwave Experiment, accelerating gradients of 17 GeV/m have been demonstrated. This achievement has been a tour-de-force that has required superior alignment and operation of the electron accelerator, laser and detection systems, together with an understanding of the non-linear aspects of beam-plasma interactions.

A small but active program has been developed using rf-technology to study materials properties. This program has collaborations with university groups both in Canada and the US, as well as others at Chalk River Laboratories.

M. Harvey, Director, Physics Division
B.M. Powell, Manager, Neutron and Condensed Matter Science Branch
J. Ungrin, Manager, Accelerator Physics Branch

SECTION 1

ACCELERATOR PHYSICS BRANCH

Edited by J. Ungrin

CONTENTS

1.1 ACCELERATOR PHYSICS BRANCH - STAFF LIST

BRANCH MANAGER: J. Ungrin

Professional Staff

F.P. Adams
R.J. Burton
S.T. Craig
M.S. de Jong
N.A. Ebrahim
C.R.J. Hoffmann
R.M. Hutcheon
J.Y. Sheikh
T. Taylor

Technical Staff

S.B. Alexander
A.D. Davidson
R.W. Davis
G. Frketich
I.L. McIntyre
W.L. Michel
G.F. Morin *(1)*
J.F. Mouris
L.W. Shankland
B.H. Smith
D.L. Smyth

Mechanical Laboratory

R.J. Bakewell
R.J. Kelly
J.F. Weaver

Laboratory Services

K.T. McKee

Secretarial Staff

M.A. Trecartin *(2)*
M.E. Carey *(3)*

Students

S.A. Covell *(4)*

Casual/Part-time

M.D. Lucuta *(5)*
M.J. Tooley *(6)*

(1) Transferred to Reactor Physics Branch, 1994 December 31.
(2) Retired 1994 January 31.
(3) Joined branch on 1994 February 01.
(4) Summer student; 1994 July 04-September 02.
(5) Terminated 1994 April 01.
(6) Terminated 1994 April 01.

1.2 SUMMARIES

Electron Linear Accelerator Development

The PHELA accelerator is being maintained as a branch facility, and has been used for the irradiation of reactor-materials samples. The PHELA control system is being upgraded and computerized to permit "hands-off" operation.

Laser Acceleration of Particles

Analytical and numerical models have been developed to describe the amplitude growth of relativistic electron plasma waves, the resonant nature of the beatwave excitation of electron plasma waves and relativistic wave-particle dynamics.

The theoretical models give an excellent description of the experimental observations.

Synchrotron Radiation Source for Canada

The Committee on Materials Research Facilities (CMRF) has now issued its final report on major materials research facilities in Canada's future.

A Synchrotron Radiation Workshop was held at the Saskatchewan Accelerator Laboratory on 1994 November 7-11, and a final report of the Workshop has been issued.

Superconducting Cyclotron

Transfer of source code and data files from the CYBER 990 mainframe computer to personal computers was completed before shutdown of the 990. The code and data files required to set up the cyclotron were altered successfully for the PC environment, and are running.

Foil-changer components were redesigned to extend the radial range, which accommodates injection into the cyclotron of ions lighter than ^{6}Li.

The particle-tracking code SUPERGOBLIN was modified to study beams that might be captured in the cyclotron via mass change at the stripper foil, thereby obtaining the necessary change in charge-to-mass ratio for beam capture.

Applications of Radiofrequency Waves to Materials

The high-temperature dielectric constant measurement system has been fully automated, and its use as a general analytical tool for ceramics (scanning dielectric analysis (SDA)) is being explored.

1.3 INDIVIDUAL REPORTS

I.3.1 Electron Linear Accelerator Development

F.P. Adams, J.Y. Sheikh, A.D. Davidson, I.L. McIntyre, L W. Shankland and B.H. Smith

PHELA is a high-power 3 GHz linac housed in a shielded tunnel in Bldg. 610. The accelerator is used for a range of commercial and nuclear reactor-related irradiations, and for the development of dosimetry procedures. A second accelerator, BEDROCS, which is currently off-line, is available for lower-energy irradiations.

The PHELA accelerator is being maintained as an irradiation and accelerator-test facility, and produces an electron beam at an energy of up to 13 MeV at a power level of up to 4 kW. Recent irradiations have required more stringent standards for beam stability and system reliability. Replacements are being fabricated for radiation-damaged beam-steering magnets, and an improved beam-line and support system, which is currently being constructed, should increase and measurement reproducibility. A new beam position monitor allows the detection of beam position changes of ±50 μm. This simple device, which uses six thermocouples to measure beam heating of a segmented ring, avoids the problem of measuring pulsed beam currents or rf signals. A closed-loop control system that controls the current to the steering magnets upstream of the monitor has been designed and constructed, but the stability observed has been adequate for the experiments carried out to date.

A new low-level rf driver manufactured by PROCOMM has been installed on PHELA to replace the 20-year-old travelling-wave tube (TWT) amplifier. The TWT amplifier had become unreliable, and used an obsolete tube for the generation of rf output power. The new driver is a hybrid design using modern, solid-state devices and small, inexpensive gridded tubes that are readily available. The new driver amplifier is capable of producing up to 500 W of power at 3000 MHz, and provides remote control of the rf drive power and frequency adjustment within ±1.0 MHz. Its operation over the last 750 h has been stable and without any problems.

The addition of a 80486-based computer, running LabView software under Microsoft Windows, has greatly improved the accelerator operation, by providing flexible algorithms for control of an experiment. This system has allowed the implementation of an automatic frequency control (AFC) system. The computer also reads the thermocouple in the beam-position monitor, and graphically displays any beam displacement. LabView has proven very useful for meeting varied beam delivery requirements, such as synchronized pulse generation and data collection, or closed-loop control of target temperature by varying the beam pulse rate. Automating these functions has eliminated the tasks which previously generated most of the operator workload. With this new system, stable continuous operation for periods up to 16 h has been possible without any operator intervention.

The control system originally installed on PHELA is a hard-wired, relay-based system that is used for on/off control of system cooling, steering magnet supplies, and other subsystems. This system incorporates circuits for both machine protection and the personnel safety system. It is becoming old, and over the years has required significant maintenance and operator intervention to stay operational. Recent interest in the irradiation with electron beams of materials to simulate the effects of long-term neutron irradiation has increased the need for stable, long accelerator runs. To minimize the manpower and time requirements for these experiments has necessitated various modifications and upgrades to the existing accelerator and control system. The existing control system is being upgraded by the addition of an OMRON Programmable Logic Controller (PLC)-based control system, with unattended operation the long-term goal. A similar unit has been used very successfully on a previous application at Chalk River Laboratories. In the new arrangement, all the machine-control and machine-protection functions will be moved to the PLC, but the personnel-safety functions will remain in a hard-wired relay control system. The PLC will also take over machine-oriented functions such as AFC and beam-position monitoring, which are independent of experiments, leaving the more flexible LabView control system to handle experiment-oriented tasks such as data collection, beam-pulse control and target-temperature monitoring. A remote rack, for thermocouple modules and various other I/O modules, will be installed in the accelerator tunnel. This rack will communicate with the main PLC via an RS-485 link, eliminating a number of cables that would otherwise be required between the tunnel and the control room. The total number of I/O points for the system will be around 150. The PLC is equipped with a touch-screen panel that can display up to 1000 programmable screens. Operators can control the machine via switches/push buttons programmed on the screens. Screens can be designed for each function of the machine, or can be linked to perform a variety of functions.

The PLC can be programmed either by using a hand-held programmer or by using a Ladder Support Software (LSS) package designed for Programmable Controllers. LLS runs on any IBM-compatible computer, and can be used to program, monitor and control the PLC. The package provides displays of various lists when the computer is operated off-line, and can be used to monitor operating conditions of the PLC, and to read and write data. PLC programs can be developed in a mnemonic or ladder logic form. The PLC is being programmed off-line using the LSS package. Testing to simulate the accelerator control system will be completed off-line before the PLC is installed in the accelerator control room.

Over the course of the year, the accelerator was used largely for irradiations involving nuclear-reactor related materials. Over 1100 h were devoted to the irradiations of samples to simulate the effect of long-term neutron irradiation. In addition, a technique has been developed to investigate the thermal properties of reactor fuels using the pulsed electron beam from PHELA.

1.3.2 Electron Beam Dynamics

The principal objectives of the electron beam dynamics programme are the development, the maintenance and the exploitation of the computer codes required to design state-of-the-art electron linear accelerator systems.

1.3.2.1 PARMELA

T. Taylor

An up-to-date PC-version of the internationally-adopted electron beam dynamics simulation code, PARMELA, was obtained from Los Alamos National Laboratory (LANL). The code was modified to accept three-dimensional electromagnetic fields calculated using the Maxwell solver, MAFIA. The PC-version of PARMELA is now able to represent, among other things, the influence of the quadrupolar fields arising from the cavity-to-cavity coupling slots in a standing-wave, electron linear accelerator.

The code was verified by modelling a nine-cell, on-axis coupled, S-band, standing-wave, electron linear accelerator with various coupling-slot configurations. The introduction of coupling-slots rotated by 90° across the accelerating cavities generated an elliptical beam spot, with an aspect ratio of about 1.5, while the introduction of coupling-slots aligned across the accelerating cavities, although generating a symmetrical beam spot, caused an emittance degradation of roughly 25%. These results are consistent with earlier experimental observations.

1.3.2.1.1 PHELA Upgrade

T. Taylor

Extensive PARMELA simulations were undertaken for a 41- cell upgrade of the on-axis coupled, S-band, standing-wave PHELA structure. The revised design is intended to generate a low-emittance 1 kW beam of 25 MeV electrons, as well as the present 4 kW beam of 11 MeV electrons. Achieving an acceptable energy spectrum over such a wide energy range proved to be a considerable challenge.

Initially, the beam energy was varied by simultaneously adjusting the gradient in all of the cells. The injector was designed to be synchronous at an intermediate energy with the same average accelerating gradient in all of the cells. The intermediate energy was chosen to maximize the product of the rf efficiencies of the two modes. The resultant full-width-at-tenth-maximum (FWTM) of the energy spectrum for the high-energy mode was almost 50%. The lengths of the first few cells were adjusted arbitrarily, to increase the product of the efficiencies still further. The FWTM of the 25 MeV energy spectrum was reduced by almost a factor of two, but only at the expense of transmission, which was reduced by nearly 25%. In an attempt to minimize the frequency of voltage breakdowns, the calculations were repeated with the same **peak** accelerating gradient in all of the cells. This can be realized by reducing the rf coupling into the shorter cells. The quality of the spectrum in the high-energy mode was consistently poor.

Subsequently, calculations were made for an accelerator structure with a fixed gradient in the first few cells and a variable gradient in the balance of the cells. Preliminary results for a synchronous injector having the same **peak** accelerating gradient in all of the cells suggest an

energy spectrum with a FWTM of less than 10% for both the 11 MeV and the 25 MeV modes. The transmission was also somewhat higher than with any of the other approaches. Practical means of addressing the rf engineering problems inherent in the design are being developed.

1.3.2.2 TOSCA

S. Craig

TOSCA is a 3-D, finite-element, magneto and electrostatics analysis program that includes facilities for non-linear and/or anisotropic materials, as well as particle tracking. To retain magnet design expertise within the Accelerator Physics Branch, a copy of the code has been acquired and familiarity with its operation is being obtained. Following a magnet-design course (offered by the U.S. Particle Accelerator School) in 1995 January, these newly-acquired skills will be applied to the design of beam routing requirements of AECL Accelerators, and to an energy-defining spectrometer for use on the PHELA accelerator.

1.3.3 Laser Acceleration of Particles

N.A. Ebrahim

The high-power CO_2 laser laboratory is operated by the branch to study advanced acceleration concepts, laser chemistry and laser surface treatment of pressure tube materials for CANDU© reactors.

1.3.3.1 High-Power CO_2 Laser System

N.A. Ebrahim, J.F. Mouris and R.W. Davis

The high-power CO_2 laser system continues to perform satisfactorily, with several significant system upgrades during the past year (Report AECL-11240, 1994).

1.3.3.1.1 Laser-Triggered Spark-Gap

J.F. Mouris and N.A. Ebrahim

We have designed and constructed a new high-voltage (46 kV) laser-triggered spark-gap to replace the existing, aging model that has been used in the switching system for many years. The input and output high-voltage terminals have been significantly re-designed to obtain a 50-Ω impedance match with the RG8 transmission line cable. We have also re-designed the gap-adjustment mechanism so that the gap can be adjusted in more controlled fashion. These modifications are designed to obtain a faster rise-time pulse from the laser-triggered spark-gap and hence a fast-rising, short pulse from the switch-out system.

1.3.3.1.2 Low-Pressure Smoothing Laser Sections

J.F. Mouris and N.A. Ebrahim

We have designed and constructed two low-pressure discharge tubes to replace the existing discharge tubes, which have deteriorated over the years and are showing poor reliability. The new low-pressure tubes are made of thick-walled quartz tubing, 60 cm long, with a bore diameter of 20 mm (compared to 15 mm for the earlier tube). This increased diameter alleviates the difficulties we have encountered previously in maintaining the necessary alignment of the tubes within the 3-metre optical cavity of the hybrid-oscillator driver system. The plasma tubes are operated with a trigger-transformer-delay (TTD) unit in conjunction with an auto-ignition coil, high-voltage pulse transformer.

1.3.3.1.3 High-Voltage Impedance-Matching Transmission Line Terminator

J.F. Mouris, R.W. Davis and N.A. Ebrahim

The laser-triggered spark-gap in the ultrafast electro-optic switching system generates a 23 kV, fast-risetime pulse, which propagates along a 50-Ω transmission line and through the transmission line Pockels Cell holders. The high-voltage pulse must be terminated in a 50-Ω, high-voltage terminator, to minimize reflections in the transmission line. This terminator has been prone to damage, as a result of high-voltage arcs which occur from time to time. We have recently made significant design changes to the terminator assembly to make it less susceptible to damage as a result of arcs. The new assembly uses a number of 500-Ω, 12.5 watt, film resistors in a high-voltage configuration with suitable adapter flanges for the RG8 transmission line cable. A combination 50-Ω and 50 kΩ, 8 watt film resistors have been used to build a voltage-divider network for a number of low-voltage (10-15 volt) trigger pulses, which are synchronized to the short laser pulse to better than 200 ps.

1.3.3.1.4 Lumonics 820 Oscillator Discharge Assembly

J.F. Mouris, R.W. Davis and N.A. Ebrahim

The main high-voltage discharge tubes containing the discharge electrodes, the pre-ionizer capacitors, the pre-ionizer electrodes and the gas circulation system, were dismantled and replaced with an identical 820 Laser system. This was necessary because the oscillator has been operating for a number of years with only minor servicing. Significant refurbishing was therefore necessary at this time, to avoid frequent arcing in the main discharge and the component damage that generally results from frequent arcs.

1.3.3.1.5 Off-Axis Parabolic Mirror CO_2 Laser Focussing Mirror

J.F. Mouris and N.A. Ebrahim

A new, off-axis, parabolic-focussing mirror was designed at Chalk River, and fabricated by Inter-Optics, a division of Lumonics. The mirror has a diameter of 15 cm, effective focal length of 125 cm, off-axis distance of 22.23 cm and off-axis angle of 10.15 degrees. The mirror was fabricated from solid aluminium (Aluminium 6061 T6), turned on a diamond lathe and coated with chromium and gold to a surface finish better than $\lambda/20$ at 10.6 μm. During the machining process, a 12.7 mm flat reference face was machined normal to the optical axis, so that the optical axis could be located precisely using an auto-collimator. The best focal position was then located by shifting the auto-collimator beam to the centre of the mirror, locating a pinhole in the centre of the target chamber and determining the best focus for the pinhole. With an f-number of 12.5, the focussing mirror was designed to produce a focal spot of diameter approximately 250 μm and a focal depth of approximately 15 mm. The focal-power density of the beam was expected to approach 2×10^{14} W/cm^2. This has been confirmed in experiments, where plasmas have been produced by tunnelling ionization of hydrogen gas, which has a tunnelling-ionization threshold of 2×10^{14} W/cm^2.

1.3.3.2 Laser Plasma Beatwave Acceleration Experiments

N.A. Ebrahim

Detailed discussions of the experiments and the main results have been published elsewhere (Research Trends in Physics, Ed. A.M. Prokhorov, AIP, 1992, pp 310-351; Proc. Linac 92 Conf. 1992; J. Appl. Phys. 76, 11, 1994 and Proc. Linac 94 Conf. 1995, in Press). The experimental energy spectrum of the accelerated beam in an argon plasma for Ar-gas pressure of 280 mtorr (full dots in Figure 1) show clear evidence of acceleration out to approximately 29 MeV. The accelerating field gradients of 1.7 GeV/m (and hence, density fluctuation $\varepsilon=\delta n_e/n_e$ of 0.17) deduced from these measurements are consistent with a model of laser-driven plasma waves in which the density fluctuation grows linearly with time, initially, and then saturates as a result of the relativistic detuning of the resonance. Simple estimates of wave amplitudes for our experimental conditions rule out the possibility of amplitude saturation by either mode-coupling or collisional damping.

We have carried out extensive analytical and numerical studies of relativistic wave particle dynamics with a model of the plasma wave, which includes longitudinal and radial fields, linear amplitude growth rates and, in the three-dimensional case, finite beam emittance *(Laser and Particle Beams, 13, 1, (1995), in Press).* For comparisons of the accelerated energy spectrum with experimental results, we show a three-dimensional case where 500 000 electrons distributed over a phase-ellipse with an emittance of 6.2×10^{-7} m.rad were accelerated in a plasma wave with longitudinal and radial fields (Figure 1.3.3.1). It was assumed that the plasma wave is linear and that beam loading is negligible. For the case of dc beam injection, electrons were externally injected into the plasma wave with a uniform phase, with distribution between 0 and

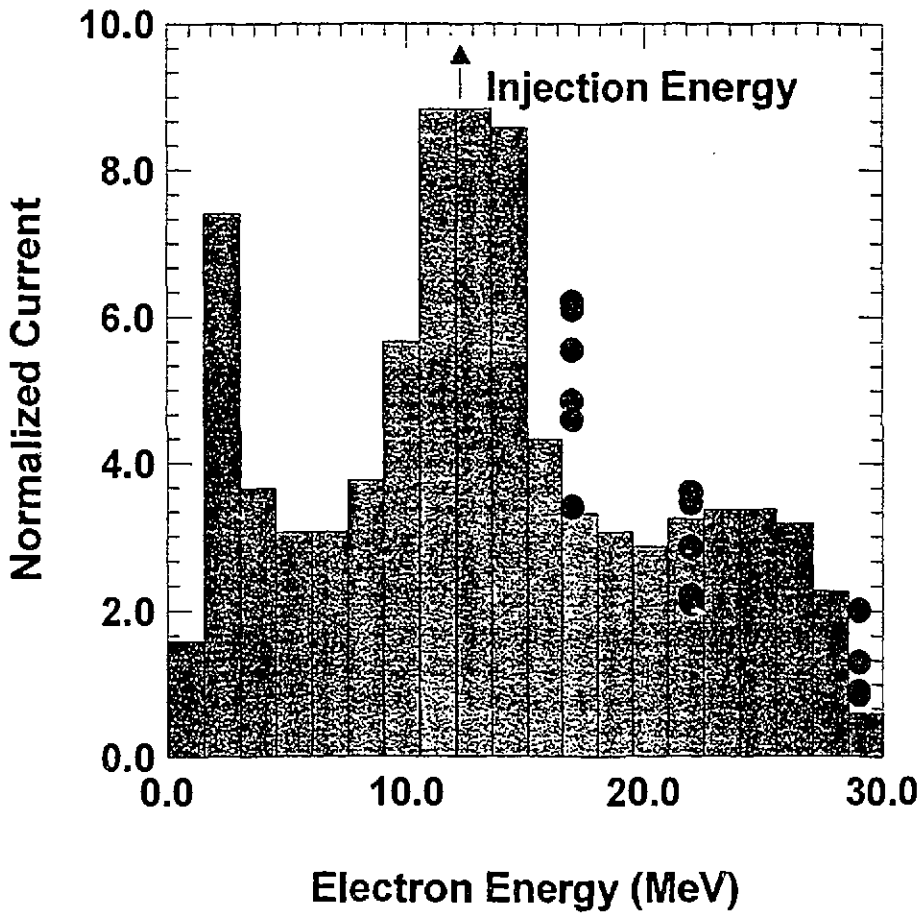

Fig. 1.3.3.1

2π radians (phase interval of $\pi/180$ per particle), and accelerated over a distance of 1 cm. The calculated output-energy spectrum shows electrons accelerated out to approximately 30 MeV, which is in excellent agreement with experimental observations. The calculated, detailed, energy spectrum also shows excellent agreement with experimental observations. Our model calculations also predict a component of the beam which is decelerated, although we do not as yet have experimental evidence for this.

Figure 13.3.2 shows the input emittance for 500 000 electrons randomly distributed over the phase-space ellipse with an emittance of 6.2×10^{-7} m.rad. The calculated output-beam emittance (Fig. 1.3.3.3) shows two distinct components which correspond to a tightly-focussed beam and a defocussed output beam. The tightly-focussed beam results from particles which are injected into the plasma wave in a phase where the radial forces are focussing, whereas the radially-

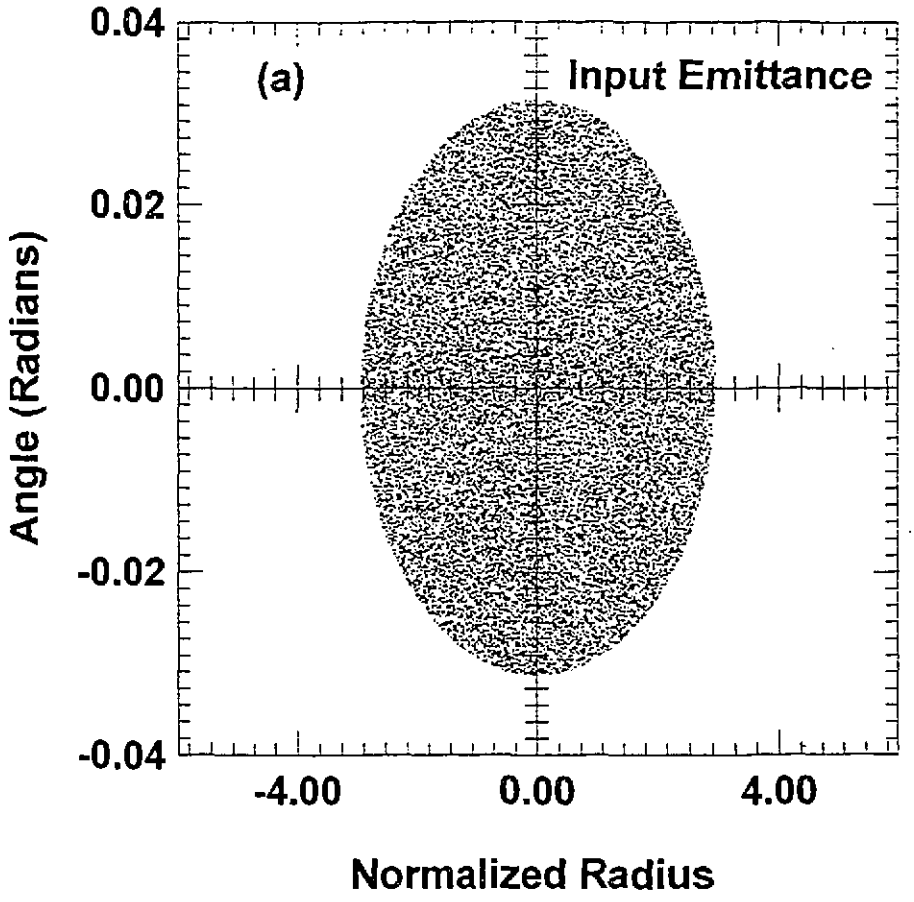

Fig. 1.3.3.2

defocussing forces result in a highly-defocussed output beam. This is readily demonstrated in a series of model calculations, where the particle bunches were injected in phases, where the radial fields were either focussing or defocussing, and the longitudinal fields of the plasma waves were either accelerating or decelerating.

Experimentally, we have established the resonant nature of the beatwave excitation of electron plasma waves by measuring the accelerated current in a given energy beam as a function of the gas-filling pressure (and hence the plasma electron density). To compare the experimental results (Figure 1.3.3.4) with theory, we have used a non-linear, fully-relativistic treatment of the plasma waves that includes a mismatch between the laser beat frequency and the plasma frequency. The governing equations describe the growth of the plasma waves up to saturation. Analytical expression for the maximum wave amplitude E_{max} is given by

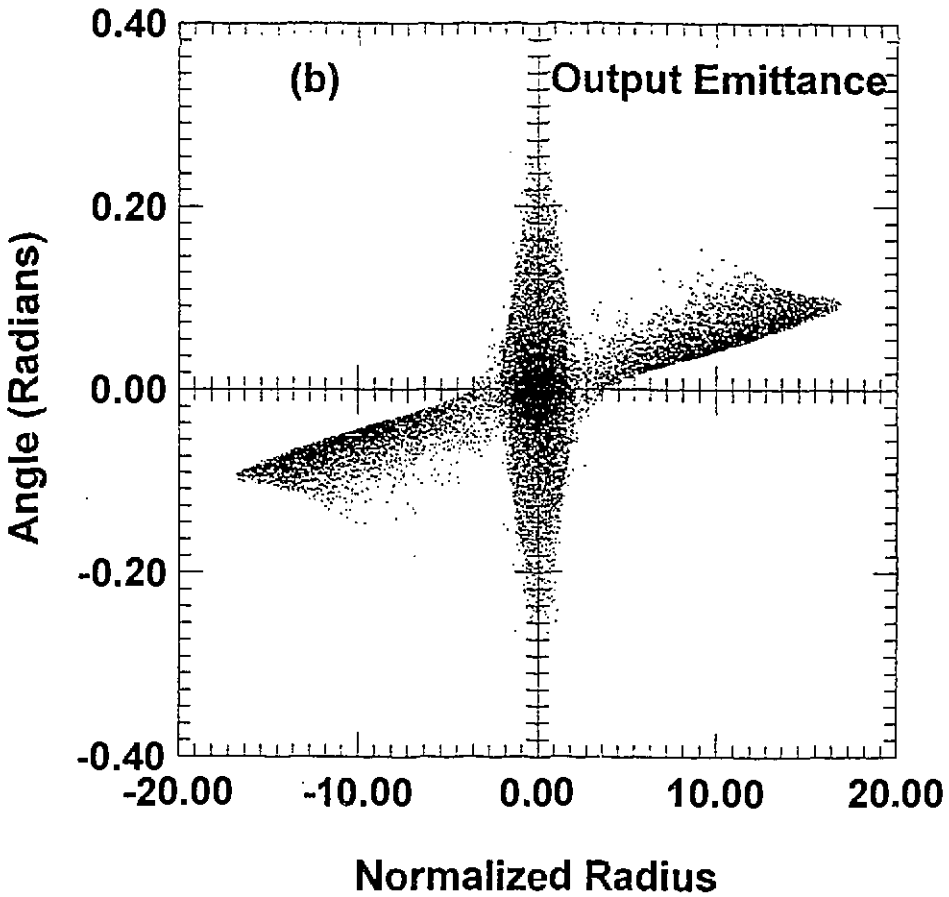

Fig. 1.3.3.3

$$E_{max}^3 + (\frac{16}{3})(f^2-1)E_{max} - (\frac{16}{3}) f^3 a = 0,$$

where $f = \Delta\omega/\omega_s = (\omega_1 - \omega_2)/\omega_s$, gives the mismatch between the laser beat frequency and the plasma frequency; $\omega_s = \omega_p/\gamma_{\perp 0}$ is the effective plasma frequency and $\gamma_{\perp 0}$ is a measure of the magnitude of the transverse oscillations induced by the laser beams. At exact resonance, f=1. For nonrelativistic motion in the transverse direction, $\gamma^2_{\perp 0} \approx 1$ and $a \approx \alpha_1\alpha_2$, where α_1 and α_2 are the maximum intensities of the two laser beams. The solid curve in Fig. 1.3.3.4 was obtained by solving the cubic polynomial in E_{max}, assuming a resonant density which corresponds to $\omega_1 - \omega_2$. For comparison with experiments, the analytical curve was normalized to the peak of the experimental measurements. Comparison between the analytical and experimental results shows excellent agreement between theory and experiments over most of the density range.

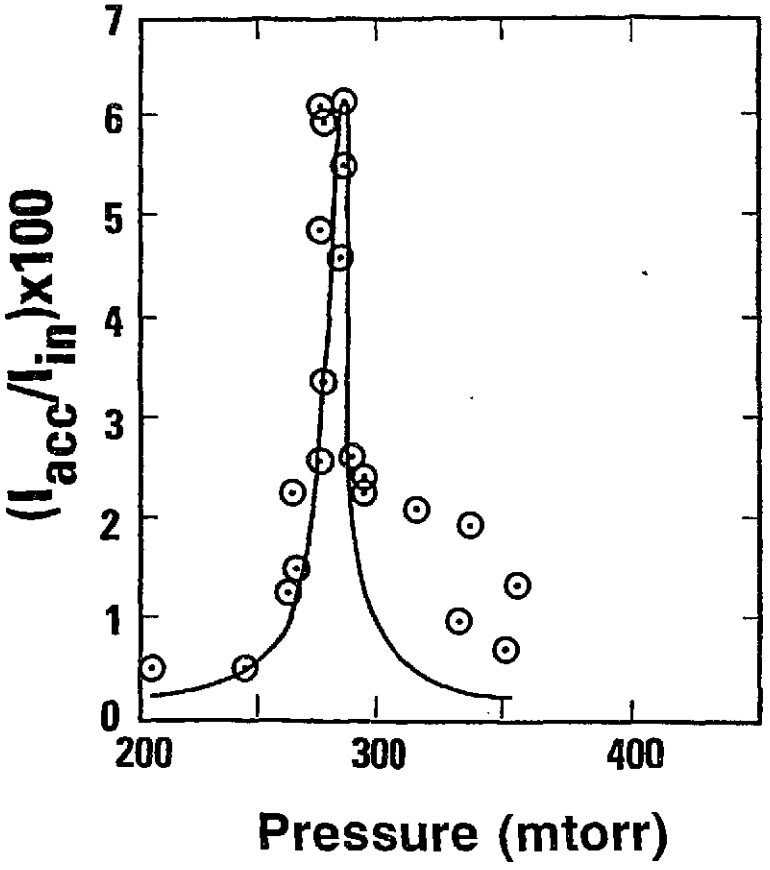

Fig. 1.3.3.4

1.3.3.3 Electron Injection System, Beamline and Spectrometer

N.A. Ebrahim

The electron accelerator system, the injection beamline and the spectrometer continue to perform satisfactorily, with some system upgrades during this past year.

1.3.3.3.1 Linear Electron Accelerator System

R.W. Davis, N.A. Ebrahim and J.F. Mouris

The accelerator system has continued to perform reliably, with some modifications in the beam-alignment procedure and technique. Faraday cups have been installed at each of the bends and the signal from these collectors is used to centre the beam in the vacuum beamline. A quadrupole doublet has replaced the quadrupole singlet as the final focussing element into the main interaction chamber. Typically, 80 -100 mA of beam current are now measured at the exit of the electron spectrometer, with a reasonable beam size at the centre of the main interaction chamber. The upgrades to the control and wiring systems have now been completed.

1.3.3.3.2 Beamline Steering Magnets

- C.R. Hoffmann, R.W. Davis and N.J. Diserens

Small picture-frame magnets, with solenoidal windings on each of four iron legs, are used at several locations along the beamline to generate coupled x- and y-direction transverse steering fields. In this application the steerer windings ran uncomfortably hot. Some features of these steerers were explored with TOSCA, which showed that operation was relatively insensitive to details of the winding geometry. The steerers were redesigned, to have a clear bore that better fit the beamline, and to have the windings wound from larger cross-section conductor. Fabrication and testing of two steerers demonstrated satisfactory performance with acceptable winding temperatures. More replacement steerers will be fabricated.

1.3.4 Intense Photon Sources

1.3.4.1 Synchrotron Radiation Source for Canada

N.A. Ebrahim and M.S. de Jong

The Committee on Materials Research Facilities (CMRF) has now issued its final report on major materials research facilities in Canada's future. On October 17-18, 1994, NSERC Council held a lengthy discussion of the final CMRF report. At the conclusion of its meeting, the Council accepted the recommendations of the report in facilitating and accelerating initiatives to coordinate the resources to establish regional "clusters" of facilities for materials research; to provide the necessary infrastructure to operate each cluster; and to initiate cooperative efforts among the parties from Industry Canada, Canadian universities, AECL, CINS, CISR, NRC, MRC and other interested parties. In view of the uncertainties surrounding the outcome of the Federal Program Review, and the Science and Technology Review, the Council did not think that the time was opportune to act on recommendations for Canada to make an immediate commitment to develop a fully-dedicated national source for Synchrotron Research.

A Synchrotron Radiation Workshop was held at the Saskatchewan Accelerator Laboratory on November 7-11, 1994. The purpose of the Workshop was to review a design for a Canadian synchrotron radiation laboratory for the Canadian Institute for Synchrotron Radiation (CISR). The specifications by CISR in 1992 called for "a world-class national synchrotron radiation facility" of 1.5-2.5 GeV, providing high brightness beams with low emittance (~10 nm-rad), and with some provision for hard x-rays. The final report of this Workshop has now been issued.

1.3.4.2 Infrared Free-Electron Laser (FEL) Study

M.S. de Jong, N.A. Ebrahim and C.R.J. Hoffmann

A recent review in the USA (Committee on Free Electron Lasers and Other Advanced Coherent Light Sources), commissioned by the US-DOE and the National Academy of Sciences, identified the far-infrared portion of the spectrum as the area most in need of further development. The relatively modest electron beam energies (10-20 MeV) needed to service such an FEL-based source matches very well the needs of accelerators under development by AECL for industrial irradiators.

A team has been assembled to study the possibility of developing a far-infrared (wavelengths greater than 10 microns) free-electron laser based on IMPELA technology. The study has two main goals: to review the possible applications of far-infrared FEL, especially those areas with relevance to nuclear reactor technology, and to assess the additional development required to build an FEL using an IMPELA-type accelerator.

1.3.5 Heavy Ion Superconducting Cyclotron

C.R. Hoffmann

TASCC Accelerators and Development Branch operate the Chalk River superconducting cyclotron. Accelerator Physics Branch provides assistance in commissioning, maintenance and operation, and in the design of improved components to enhance performance and reliability.

1.3.5.1 Foil Changer

C.R. Hoffmann

To successfully inject ions lighter than ^{6}Li into the cyclotron, the foils must be able to travel to radial positions beyond 265 mm. Modifications to components mounted in the dee interior have been identified which extend the range outwards by 17 mm. Detailed design is completed and fabrication will begin early in 1995.

1.3.5.2 Computing

1.3.5.2.1 Code Conversion

C.R. Hoffmann

The major programs used to calculate cyclotron setup parameters (TRIUMF2, TRIUMF3 and SUPERGOBLIN) have been successfully modified to compile on the WATCOM 77/386 Fortran compiler. SUPERGOBLIN had to be changed to double precision because single precision (roughly 1 in 10^7) was not able to acceptably reproduce test-case results, but double precision was acceptable. TRIUMF3 was revised to write output field maps with double precision data. As well, several smaller auxiliary codes have been converted for operation on personal computers that run the WATCOM compiler.

The PC versions of these codes have been used to calculate parameters of beams that were subsequently developed and successfully run in the cyclotron.

1.3.5.2.2 File Transfer

C.R. Hoffmann, E.H. Lindqvist and W. Michel

Transfer of code and data files from the CYBER 990 computer to fast personal computers was completed. This activity was in response to the announcement that the CYBER 990 mainframe computer would be shut down on 1994 May 31. The personal computers operate under DOS and use the WATCOM77/386 Fortran compiler. About 2500 files were transferred. All of the data files that the program SUPERGOBLIN reads were rewritten as double precision binary files using auxiliary codes compiled with the WATCOM compiler.

All of the cyclotron data files, as well as various others, were made available from a shared area set up on the VAX system that is accessible to the personal computers over the network via PATHWORKS. This arrangement provides security and daily backup.

1.3.5.2.3 Beam Capture by Mass Change

C.R. Hoffmann and E.H. Lindqvist

The cyclotron is designed to capture injected ion beams by passing them through a thin carbon foil to change the charge state of the ions, and consequently their charge to mass ratio, by a factor of two or three. The lightest ion that the design treated was ^6Li. Calculations with IONSCAN and SUPERGOBLIN show that ions lighter than Li may be captured and accelerated. Such beams generally require that the foil be positioned beyond the range limit of 265 mm. ^3He, charge state +1, was injected, fully stripped to +2 by a foil placed at 270 mm and accelerated to 50 MeV/u. However, the lightest ions H^+ and D^+ are fully stripped before encountering the foil, and consequently cannot be captured by charge stripping. An alternative method is being

explored for them of injecting singly charged, molecular beams that would result in singly charged atomic beams after passing through the foil. The effect would be to have the mass of the injected particle change by a factor of two or more. A study was started that will explore the feasibility and requirements of this mass change scheme. Initial results indicate that deuterium beams with specific energies up to 40 MeV/u might be produced using an injected beam of singly charged triatomic molecules of energy 14.6 MeV. Implementation would require development of an appropriate ion source that would be located in the terminal of the Tandem.

SUPERGOBLIN was modified to model mass change at the stripper foil as follows. Upon encountering the foil, an injected molecular ion breaks up into N atomic ions of equal mass and charge. Each atomic ion has kinetic energy E/N and momentum P/N, where E and P are the kinetic energy and total linear momentum of the injected particles. However, in SUPERGOBLIN momentum is embedded in the code in units of m_0c (product of rest mass and speed of light). Consequently, this stripping process caused a change in the units of momentum, but not the numerical magnitude. Revisions were made to use only the momentum units associated with the particle mass after stripping.

1.3.5.2.4 Code Development

C.R. Hoffmann

For some combinations of inner and outer coil currents, the code TRIUMF2 failed to calculate correct values of lattice parameters that logically represent the operating area of the cyclotron magnet. This situation arose because of the loss of precision when the code was transferred from a system that used 64-bit words, to the PC, which uses 32-bit words. Satisfactory results were restored when the appropriate variables were incremented in step-sizes that were sufficiently larger than the intrinsic precision limits.

Code that allowed magnetic fields to be calculated for coil currents outside the mapped region was inadvertently omitted from the version of TRIUMF2 that was transferred from the CYBER 990 to the PC. This code was installed in the PC version and was debugged and commissioned.

The code EXMAP, which is used to calculate extraction channel magnetic field maps, was successfully set up on the PC to operate under the WATCOM77/386 compiler.

1.3.6 Applications of Radiofrequency Waves to Materials

R.M. Hutcheon, G.F. Morin and B.H. Smith

Accelerator Physics Branch has developed experience in the application of rf technology to the study of materials properties and to the processing of materials. The branch has developed two key tools for this work - SEAFISH, the complex 2-D code that calculates the detailed distribution of rf fields in materials in an "applicator", and the high-temperature, complex dielectric constant measurement apparatus, that has recently been fully automated. Both these tools continue to

attract commercial contracts and justify continued underlying development work.

Over the past few years several carefully-documented cases of enhanced organic synthesis reaction rates have been reported using microwave heating. Recently, a small experiment was initiated with Prof. R. Gedye of the Dept. of Chemistry & Biochemistry, Laurentian University, to study the possible source of this enhancement - specifically to measure the effect of strong electric field gradients in a microwave digestion "bomb". Various gradient-enhancing inserts were made and shipped to the university for testing on an organic synthesis reaction.

The possible advantages of microwave-driven, advanced-ceramic synthesis are of interest to the materials community. A collaboration was initiated with M. Mathis at the Materials Research Lab. at Penn. State University, on leave from the 3M Ceramic Technology Centre in St. Paul. He is studying the high-temperature microwave-driven synthesis of aluminum titanate (Al_2TiO_5) and of Sialons and, in particular, is trying to understand the enhanced reaction rates noted when different flowing gas atmospheres are used. We have done complex dielectric constant measurements on these materials using conventional heating, but otherwise following their processing rates and conditions. The results of the collaboration are expected to be reported in two papers at the 1995 Spring MRS meeting.

The collaboration with Prof. D. Clarke's group at the University of Florida, Materials Science & Engineering Dept., continued this year, and included a very interesting set of measurements up to 1400°C of the dielectric properties of aluminas generated by the sol-gel process and loaded with various known microwave-absorbing materials, including chromia, silicon carbide, nickel and iron oxides.

A new multimode cavity for measuring permeability as a function of frequency and static magnetic bias field was designed, constructed and tested. Calibration of the unit is not complete and modifications to increase mode separation may be necessary.

The multimode (400 MHz-3000 MHz), dielectric properties measurement system was fully automated using in-house software developed for "Labview for Windows" and National Instruments data acquisition hardware. The system steps the temperatures, waits for settling times, moves the samples between the furnace and the cavity, and drives the Hewlett-Packard network analyzer system.

The high-temperature dielectric properties of a sheet of aluminum nitride were measured for the AECL TASCC group, to assist them in the design and selection of a new rf window material for an ECR ion source.

1.3.7 Ion Linear Accelerator Technologies

T. Taylor and J.Y. Sheikh

The ion linear accelerator development programme was discontinued in the spring of 1993, after almost thirty years at the forefront of research into high-current, cw, ion beams. Nonetheless, researchers at CRL and elsewhere continue to call on the expertise of the Accelerator Physics Branch for hardware and consultations both on a commercial and on a collaborative basis.

1.3.7.1 Chalk River Injector Test Stand (CRITS)

T. Taylor and J.Y. Sheikh

The entire RFQ1 system, including a 50 keV, microwave, proton source, a low-energy beam transport (LEBT) system, two 250 kW, cw, klystrode-based, rf power supplies and a 1.25 MeV radiofrequency quadrupole (RFQ) accelerator, was transferred to Los Alamos National Laboratory (LANL) when the ion accelerator development program at CRL was terminated. The Accelerator Operations and Technology (AOT) Division at LANL has since been exploiting the hardware, which has been renamed the Chalk River Injector Test Stand (CRITS), to gain experience in the crucial low-energy portion of a high-current, cw, linear accelerator.

1.3.7.1.1 Microwave Proton Source and LEBT System

T. Taylor

The 2.45 GHz microwave proton source has been extensively characterized at LANL. The high discharge efficiency and the high proton fraction measured at CRL have been confirmed. The system was operated continuously for one week (170 h) at a beam current of 60-65 mA dc, with an extraction voltage of 47 kV. Availability was 96%. All of the downtime was attributed to periodic high-voltage sparkdowns in the extraction system. The plasma generator performed flawlessly.

The injector has been installed in an off-line configuration, with the emittance measurement unit (EMU) replacing the RFQ, so that the LEBT system, which consists of nothing more than a drift followed by a solenoid followed by a drift, could be evaluated. The measurements suggest an emittance growth of approximately 70% and a steering error of 0.5 to 3.2 mm. The steering error is consistent with the observed dipole component in the solenoid field. (A misalignment of 1.0 mm will give rise to a 10% reduction in the transmission of the RFQ.) Calculations with the macroparticle code, SCHAR, using the measured solenoid fields and an effective ion beam current of 1.0 mA, predict a total emittance growth of 38%, of which 32% is attributable to solenoid aberrations and 6% is related to residual space-charge. (The residual space-charge, according to beam-plasma simulations, corresponds to an effective ion beam current of 1.4 mA. Fits to the experimental data with the beam-envelope code, TRACE, suggest an effective beam current of 1.0 mA.) Further studies are needed to address the problems of solenoid steering and

LEBT emittance growth.

1.3.7.1.2 RF Power Supplies and RFQ Accelerator

J.Y. Sheikh

Both of the 267 MHz, klystrode-based, rf systems have been installed at LANL. These amplifiers have the very desirable attributes of high efficiency and good output control at high output power levels. One of the amplifiers has been used for preliminary trials and to condition the RFQ structure.

Initial testing of the rf system into a resistive load confirmed the klystrode operating characteristics previously measured at CRL. The final power amplifier (FPA) had a gain of >20 dB as it increased the 1 kW driver-klystrode input power to >250 kW of output power. LANL staff also observed the klystrode efficiency (dc to rf conversion) to be above 70% at 250 kW. The 1 dB bandwidth of the FPA output amplitude was 1.4 MHz.

Preliminary tuning of the RFQ at 160 kW with a 5% duty factor led to a frequency shift of -10 kHz, well within the tuning range of the klystrode. The RFQ has recently been conditioned to 160 kW cw. Further conditioning is planned before operation with beam into the accelerator is attempted.

1.3.7.2 Microwave Ion Sources for TASCC

T. Taylor, J.S.C. Wills and N.J. Diserens

The permanent magnet microwave ion source was equipped with a hot-finger to supply bismuth vapour and a heated, boron nitride liner to suppress condensation. An ion beam, comprised 45% of bismuth and 55% of xenon, was extracted at 19 kV with a high-voltage power supply drain of 3.0 mA. About 0.5 mA was transported through a dormant charge-exchange canal. Spectral analysis showed that, with a cesium charge-exchange medium, as much as 25 μA of Bi^- could be generated. The ion source and the charge-exchange canal were subsequently installed on a TASCC high-voltage deck, and a Bi^- beam was successfully injected into the tandem accelerator and through the superconducting cyclotron.

The magnetic field configuration of the present, permanent magnet, microwave ion source is only a crude approximation of the optimum. The entire ion source, including the extraction system, has been redesigned for increased efficiency, improved reliability and simplified servicing. The preparation of engineering drawings is nearing completion.

In principle, the negative ion beam system could be simplified immensely by eliminating the charge-exchange canal and extracting negative ions directly from the plasma. Initial attempts at direct extraction were hampered by the presence of a solenoidal field at the plasma electrode. A version of the microwave ion source with an electromagnetic solenoid at the microwave

window and a permanent magnet multipolar cusp at the plasma electrode has been developed using the TOSCA three-dimensional magnetostatics code. The design has yet to be verified.

For details of microwave ion source development activities, refer to PR-TASCC-9, AECL-11239.

1.4 PUBLICATIONS AND LECTURES

Publications

OPTICAL MIXING OF LASER LIGHT IN A PLASMA AND ELECTRON ACCELERATION BY RELATIVISTIC ELECTRON PLASMA WAVES
N.A. Ebrahim
J. Appl. Phys. 76 (11), 7645 (1994).

A UV PRE-IONIZED DUAL-WAVELENGTH SHORT-PULSE HIGH-POWER CO_2 LASER FACILITY FOR LASER PARTICLE ACCELERATION RESEARCH
N.A. Ebrahim, J.F. Mouris and R.W. Davis
AECL Report, AECL-11240 (1994).

ELECTRON ACCELERATION BY RELATIVISTIC ELECTRON PLASMA WAVES IN THE LASER PLASMA BEATWAVE ACCELERATOR CONCEPT
N.A. Ebrahim
Proc. Linac 94 Conference, 1995 (in Press).

DC PROTON BEAM MEASUREMENTS IN A SINGLE-SOLENOID LOW-ENERGY BEAM TRANSPORT SYSTEM
R.R. Stevens, Jr., P. Schafstall, J.D. Schneider, J. Sherman, T. Zaugg and T. Taylor
ibid.

INSTALLATION OF CW RADIOFREQUENCY QUADRUPOLE ACCELERATOR AT LOS ALAMOS NATIONAL LABORATORY
J.D. Schneider, J. Bolme, V. Brown, M. Milder, G. Neuschaefer, D. Rees, P. Schafstall, J. Sherman, R.R. Stevens, Jr., T. Zaugg, G.E. McMichael, J. Sheikh and T. Taylor
ibid.

INSTALLATION AND TEST RESULTS OF A HIGH-POWER, CW KLYSTRODE AMPLIFIER AT LOS ALAMOS NATIONAL LABORATORY
M. Lynch, D. Keffeler, D. Rees, W. Roybal and J. Sheikh
ibid.

INDUSTRIAL APPLICATIONS OF LOW-ENERGY LINACS
J. Ungrin
ibid.

THE ACCELERATION OF PARTICLES BY RELATIVISTIC ELECTRON PLASMA WAVES DRIVEN BY THE OPTICAL MIXING OF LASER LIGHT IN A PLASMA
N.A. Ebrahim and S.R. Douglas
Laser and Particle Beams 13 (1), 1995 (in Press).

BATES SOUTH HALL RING RF CONTROL SYSTEM
S.T. Craig, M.S. de Jong, G. Frketich, G.F. Morin, A. Zolfaghari and P.T. Demos
Proc. of 1994 European Particle Accelerator Conference, eds. V. Suller and Ch. Petit-Jean-Genaz, p. 1839 (1994).

PERFORMANCE OF THE MIT-BATES SOUTH HALL RING 2856 MHZ CW RF CAVITY SYSTEM
M.S. de Jong, S.T. Craig, A. Zolfaghari, B. Binns, P.T. Demos and D. Wang
ibid., p. 1888.

FERRITE-LOADED HIGHER-ORDER-MODE ABSORBERS FOR THE MIT-BATES SOUTH HALL RING
M.S. de Jong, F.P. Adams, R.M. Hutcheon, G.F. Morin, R.J. Bakewell, A. Zolfaghari and P.T. Demos
ibid., p. 2016.

HIGH-POWER RF CAVITY R&D FOR THE PEP-II B FACTORY
R. Rimmer, G. Lambertson, J. Hodgson, K. Ko, C. Ng, R. Pendleton, E. Reuter, H. Schwarz, K. Skarpaas, F. Adams, R. Burton, M. de Jong, M. Lipsett, C. Belser, M. Franks and T. McCarville
ibid., p. 2101.

HIGH-VOLTAGE SAFETY CODE
C.R. Hoffmann, R.J. Burton and J.Y. Sheikh
CRNL-200(Rev.3), 1994

RELATIVE EFFICACY OF HIGH-ENERGY ELECTRONS AND GAMMA RAYS IN THE ACTIVATION OF SEVERAL SPECIES OF MICROORGANISMS
L.M. Lucht, C.B. Saunders, J.W. Barnard, J. Borsa and D.L. Smyth
Submitted to J. Radiation & Sterilization, 1994 September

BEAM SCANNING FOR DOSE UNIFORMITY
J. McKeown, S.T. Craig, N.H. Drewell, G. Frketich and D.L. Smyth
Presented at 9th Int. Meeting on Radiation Processing (IMPR-9), Instanbul, Turkey, 1994 Sept. 11-16

Patents

ELECTRON RADIATION DOSE TAILORING BY VARIABLE BEAM PULSE GENERATION
D.L. Smyth and G. Frketich
1994 Sept. 9, U.S. Patent Application 08/302/036

Conference Presentation

ELECTRON ACCELERATION BY RELATIVISTIC ELECTRON PLASMA WAVES IN THE LASER PLASMA BEATWAVE ACCELERATOR CONCEPT
N.A. Ebrahim
Paper presented at Linac 94 Conference, Tsukuba, Japan, 1994 August 21-26.

MICROWAVE DRIVEN NEGATIVE ION SOURCES
J.S.C. Wills, T. Taylor, N.J. Diserens and P.A. Dube
Presented at 17th International Linac Conference, Tsukuba, Japan, 1994 August 21-26.

DC PROTON BEAM MEASUREMENTS IN A SINGLE-SOLENOID LOW-ENERGY BEAM TRANSPORT SYSTEM, R.R. Stevens, Jr., P. Schafstall, J.D. Schneider, J. Sherman, T. Zaugg and T. Taylor, *ibid.*

INSTALLATION OF CW RADIOFREQUENCY QUADRUPOLE ACCELERATOR AT LOS ALAMOS NATIONAL LABORATORY
J.D. Schneider, J. Bolme, V. Brown, M. Milder, G. Neuschaefer, D. Rees, P. Schafstall, J. Sherman, R.R. Stevens, Jr., T. Zaugg, G.E. McMichael, J. Sheikh and T. Taylor, *ibid.*

INSTALLATION AND TEST RESULTS OF A HIGH-POWER, CW KLYSTRODE AMPLIFIER AT LOS ALAMOS NATIONAL LABORATORY
M. Lynch, D. Keffeler, D. Rees, W. Roybal and J. Sheikh, *ibid.*

INDUSTRIAL APPLICATIONS OF LOW-ENERGY LINACS
J. Ungrin, *ibid.*

INDUSTRIAL APPLICATIONS OF COMPACT ACCELERATORS
J. Ungrin
Paper presented at U.S. Advanced Technology Program Workshop on Beams, Plasmas, Lasers and Microwaves, Albuquerque, New Mexico, 1994 September 27-28

SECTION 2

NEUTRON AND CONDENSED MATTER SCIENCE BRANCH

Edited by S.M. Kim

CONTENTS

2.1 NEUTRON AND CONDENSED MATTER SCIENCE BRANCH STAFF LIST

BRANCH MANAGER: B.M. Powell

Professional Staff

W.J.L. Buyers (1)
A.P. Clarke (2)
M. Couture
E.D. Earle
J.D. Hepburn (3)
T.M. Holden
T.C. Hsu (4)
J. Katsaras (5)
S.M. Kim
M.A. Lone
F.J. Marsiglio
R.B. Rogge (6)
J.H. Root
V.F. Sears
B. Sur (7)
E.C. Svensson
I.P. Swainson (8)
D. R. Taylor (9)
Z. Tun

Technical Staff

J.J.P. Bolduc
R.J.E. Deal
D.A. Doering
R.L. Donaberger (10)
J.H. Fox
E.R Gaudette
M.D. Gauthier
L.E. McEwan
M.W. Montaigne
P.A. Moss (11)
H.F. Nieman (12)
M.M. Potter
G.A. Sims
H.C. Spenceley
D.C. Tennant

Secretarial Staff

J.S. Hill

(1) Returned to NCMS from sabbatical, 1994 August 04.
(2) Research Associate, jointly with Reactor Materials Research Branch, joined 1994 April 04.
(3) On attachment to SNO Project at Laurentian University, Sudbury.
(4) Research Associate terminated 1994 September 08.
(5) Research Associate joined NCMS 1994 September 19.
(6) Research Associate.
(7) Term Appointment.
(8) Research Associate, jointly with University of Guelph.
(9) Visiting Scientist, returned to Queen's University 1994 August 04.
(10) NSERC Technician with McMaster University attached to NCMS Branch.
(11) Glassblowing Apprentice.
(12) Retired, 1994 January 18.

Visiting Scientists

M. Birsan	McGill University
E. Bonvin	Queen's University
M. Brauss	Proto Engineering, Windsor
S. Brock	University of California, San Diego
G. Byczyski	University of Windsor
L. Clapham	Queen's University
S. Clarke	University of Oxford
M. Collins	McMaster University
J. Dahn	Simon Fraser University
W. Dimaline	University of Waterloo
R. Drew	McGill University
E. Fawcett	University of Toronto
E. Fuller	Simon Fraser University
Z. Gamba	CNEA, Buenos Aires
B. Gaulin	McMaster University
P. Gerard	Queen's University
J. Greedan	McMaster University
T. Hayakama	McGill University
J.G. Hykawy	Laurentian University
T. Krause	Queen's University
A. Lamarche	Université d'Ottawa
G. Lamarche	Université d'Ottawa
S. MacEwen	Alcan International
M. Mao	McMaster University
T. Mason	University of Toronto
A.Z. Menshikov	University of Toronto
S. Mentink	University of Toronto
G. Mills	University of Salford
H. Nakotte	Los Alamos National Laboratory
E.B. Norman	Lawrence Berkeley Laboratory
O. Petrenko	McMaster University
J. Porter	Defence Research Establishment Atlantic, Halifax
A. Purwanto	Los Alamos National Laboratory
D. Rancourt	Université d'Ottawa
R. Robinson	Los Alamos National Laboratory
A. Roordea	University of Waterloo
J. Savoie	McGill University
S. Spooner	Oak Ridge National Laboratory
M. Steinitz	St. Francis Xavier University
E. Sternlieb	Brookhaven National Laboratory
J.A. Szpunar	McGill University
L. Taillefer	McGill University
D. Tindall	Dalhousie University
P. Webster	University of Salford

S. Westcott	Queen's University
P. Withers	University of Cambridge
J. Woolley	Université d'Ottawa
S. Yue	McGill University
V. Zacek	Université de Montréal

Graduate Students

H. Abuluwefa	McGill University
C. Adams	Dalhousie University
D.F. Agtenberg	University of Toronto
A. Di Chiro	McGill University
M-Z. Dhang	Université d'Ottawa
B. Ellman	McGill University
M. Gharghouri	McMaster University
R. Ham-su	McMaster University
J. Junginger	University of Waterloo
E. Kartini	McMaster University/Hahn Meitner Institute, Berlin
T. Kerr	University of Waterloo
J-J. Liang	University of Manitoba
G. Liu	McMaster University
M. Lumsden	McMaster University
B. Lussier	McGill University
E. Martinelli	McGill University
W. Minor	McMaster University
K. Murnaghan	Queen's University
T. Peterson	University of Toronto
R. Pridmore	University of Waterloo
M. Sandlin	Purdue University
M. Small	Dalhousie University
N. Towneley	Queen's University
M. Wells	University of British Columbia

Visiting Apprentice (Glassblowing)

L. Cafferty	AECL, Whiteshell Laboratory

2nd WORKSHOP ON NEUTRON POWDER DIFFRACTION
1994 May 26-27

J. Bareman	Xerox Research Centre of Canada
E. Brouwer	National Research Council
M. Drouin	Université de Sherbrooke
B. Finch	University of Manitoba
I. Garneau	Université de Montréal
A. Héroux	Université de Montréal

T. Jiang	University of Toronto
N. Jourdan	Université de Montréal
J. Junginger	University of Waterloo
T. Kullberg	FMC - Lithium Division
J. Liang	University of Manitoba
C. McCague	National Research Council
R. McEachern	AECL
M. Mao	McMaster University
J. Nicholls	University of Calgary
P. Prado	University of New Brunswick
R. Pridmore	University of Waterloo
S. Petrov	University of Toronto
C. Winters	Merck Frosst Canada Inc.

NEUTRON APPLICATIONS IN MATERIALS SCIENCE AND ENGINEERING
1994 August 15-19

M. Budhu	University of Arizona
A. Chatt	Dalhousie University
L. Clapham	Queen's University
B. Clausen	Risø National Laboratory
A. Colotto	McMaster University
G. Downing	National Institute of Standards and Technology
R. Epand	McMaster University
J. Garrett	McMaster University
M. Gharghouri	McMaster University
F. Haeussler	Fraunhöfer Institute, Saarbrücken, Germany
E. Kartini	McMaster University
T. Kerr	University of Waterloo
A. Krawitz	University of Missouri
G. Langelaan	Queen's University
A. Lodini	University of Rheims, France
G. Long	National Institute of Standards and Technology
C. Majkrzak	National Institute of Standards and Technology
J. Mashek	Northwestern University
I. Pho	University of Western Ontario
D. Price	Argonne National Laboratory
R. Pynn	Los Alamos National Laboratory
P. Rangaswamy	Los Alamos National Laboratory
J. Richardson	Argonne National Laboratory
T. Russell	IBM, Almaden
J. Ryskamp	Idaho National Engineering Laboratory

D. Schaefer	Office of American Competitiveness, Washington
S. Shapiro	Brookhaven National Laboratory
D. Shaw	McMaster University
S. Spooner	Oak Ridge National Laboratory
S. Torbaty	Université de Toulon et du Var, France
N. Towneley	Queen's University
P. Walker	University of Western Ontario
J. Wallace	University of Western Ontario
D. Wang	The Open University, England

TOPICAL REVIEW

Phonon Density of States from Incoherent Inelastic Neutron Scattering

V.F. Sears *(AECL)*

The scattering length that characterizes the interaction of a thermal neutron with a nucleus depends on both the nuclear spin and the isotopic species. In condensed matter the spins are randomly oriented and the various isotopes are randomly distributed throughout the system. As a result, the scattering cross section is the sum of two terms: a 'coherent' cross section, which is characteristic of the collective motion of the atoms, and an 'incoherent' cross section, which is characteristic of the single-particle motion.

The scattering cross section is usually expressed in terms of the Van Hove scattering function $S(\mathbf{Q}, \nu)$, in which $\mathbf{Q}$ and ν are the momentum and energy transfers in the collision (expressed in units of Planck's constant). For a harmonic crystal the coherent scattering function at small $\mathbf{Q}$ is of the form

$$S_{coh}(\mathbf{Q}, \nu) \propto \delta(\nu - \nu_{kj}), \tag{1}$$

where ν_{kj} is the frequency of the phonon that is created in the collision, $\mathbf{k} = \mathbf{Q} - \mathbf{K}$ is its wave vector, and j the polarization index. By convention, $\mathbf{K}$ is the reciprocal lattice vector that puts $\mathbf{k}$ in the first Brillouin zone.

The corresponding incoherent scattering function is of the form

$$S_{inc}(\mathbf{Q}, \nu) \propto f(\nu), \tag{2}$$

in which $f(\nu)$ is the velocity spectrum, i.e. the Fourier transform of the velocity autocorrelation function of an atom in the system. For a harmonic crystal,

$$f(\nu) = \frac{1}{N_0} \sum_{kj} | \hat{\mathbf{Q}} \cdot \hat{\mathbf{e}}_{kj} |^2 [\delta(\nu - \nu_{kj}) + \delta(\nu + \nu_{kj})], \tag{3}$$

where $\hat{\mathbf{Q}}$ is a unit vector in the direction of $\mathbf{Q}$, $\hat{\mathbf{e}}_{kj}$ is the phonon polarization vector, and N_0 the number of unit cells. The velocity spectrum $f(\nu)$ is closely related to the phonon density of states $g(\nu)$, which determines the thermodynamic properties of the system (e.g., the internal energy, entropy, specific heat, etc.). In particular,

$$g(\nu) = \frac{1}{3sN_0} \sum_{kj} \delta(\nu - \nu_{kj}) \tag{4}$$

where s is the number of atoms per unit cell. Note that, although Eqs. (1), (3), and (4) are only valid for harmonic crystals, the relation (2) is completely general, and also applies to gases, liquids, and anharmonic or amorphous solids.

In most materials, the incoherent scattering is very much weaker than the coherent scattering, and inelastic neutron scattering measurements then provide direct information on the collective motion of the atoms. Thus, for example, in a crystal, the observed positions of the sharp coherent one-phonon peaks (1) provide a direct measurement of the frequencies of the normal modes of vibration of the crystal ν_{kj}. These can then be fitted to theoretical models to determine the interatomic forces in the crystal.

Two important exceptions are hydrogen and vanadium, for which the incoherent scattering is two orders of magnitude larger than the coherent scattering. For these elements, inelastic neutron scattering provides a direct measurement of the velocity spectrum $f(\nu)$. Since vanadium has the body-centered cubic structure, the dependence of $f(\nu)$ on the phonon polarization vectors vanishes and one finds that

$$f(\nu) = g(\nu), \qquad \nu \geq 0. \tag{5}$$

In the past six years, numerous inelastic neutron scattering experiments have been performed at NRU to determine the velocity spectrum $f(\nu)$ and, in some cases, the phonon density of states $g(\nu)$ for various kinds of materials. This work has been done in collaboration with a number of people at AECL (E.C. Svensson, B.M. Powell, W. Montfrooij, J.H. Root, I.P. Swainson, and C. Szomel), at NRC (E. Whalley, D.D. Klug, J.S. Tse, C.I. Ratcliffe, and Y.P. Handa), at Laurentian University (E.D. Hallman), and at Dalhousie University (M.A. White).

Fig. 1 shows the phonon density of states $g(\nu)$ obtained for four phases of ice: the cubic crystalline (Ic) phase, the hexagonal crystalline (Ih) phase, the low-density amorphous (lda) phase, and the high-density amorphous (hda) phase. A theoretical relation was used to convert the experimental $f(\nu)$ distributions to $g(\nu)$, and the specific heat curves calculated from these results are in excellent agreement with available directly-measured values. The experiments covered both the phonon band (which characterizes the center-of-mass motion of the H_2O molecules) and the libron band (which characterizes the librational motion of the H_2O molecules about their centers of mass). The peaks in the phonon spectrum correspond to the transverse acoustic (TA) modes, the longitudinal acoustic (LA) modes, the transverse optic (TO) modes, and the longitudinal optic (LO) modes.

Experiments have also been performed to determine the motion of CH_4 molecules in D_2O clathrate at six temperatures between 5 and 77 K. This is a form of ice that is characterized by an open lattice of water molecules containing large cages that are stabilized by the inclusion of guest molecules (in this case CH_4), which can move more or less freely within the cages. The neutron scattering by this system is due almost entirely to incoherent scattering by the H atoms in the methane molecules, so that neutron inelastic scattering measurements allow one to study both the translational and rotational motion of the trapped methane molecules. The experimental $f(\nu)$ distribution at 5 K shows a sharp peak at 0.26 THz, which is due to the $J = 0 \rightarrow 1$ rotational transition of the CH_4 molecules. This result demonstrated for the first time the free quantum-mechanical rotation of trapped molecules in clathrate structures. The $f(\nu)$ results also show an irregular distribution of intensity from 0.5 to 4.0 THz, which broadens with increasing temperature. This is attributed to the translational motion of the CH_4 molecules and is in qualitative agreement with molecular dynamics calculations.

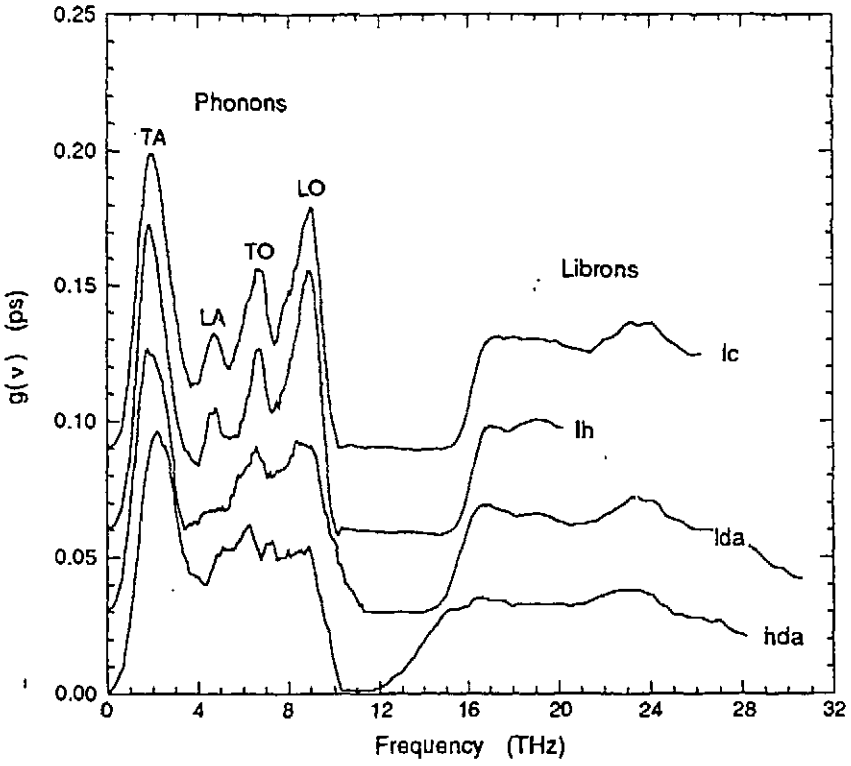

Fig. 1 The phonon density of states $g(\nu)$ for four phases of ice determined from incoherent inelastic neutron scattering experiments at NRU. Results are shown for the cubic crystalline (Ic) phase, the hexagonal crystalline (Ih) phase, the low-density amorphous (lda) phase, and the high-density amorphous (hda) phase. The Ic, Ih, and lda curves have been shifted upward for clarity.

We have also done experiments on H_2O clathrate that is stabilized by the inclusion of Xe and Kr atoms. Here, the observed scattering is due almost entirely to incoherent scattering by the H atoms in the host lattice. These experiments provide information on the vibration of the clathrate lattice and are again in good agreement with molecular dynamics calculations. Similar experiments have also been performed on clathrates of Dianin's compound.

Useful information on lattice vibrations can also be obtained from inelastic neutron scattering experiments on polycrystalline or powder samples of coherent-scattering materials, where the presence of a large number of randomly-oriented grains tends to average-out interatomic interference effects, with the result that the scattering is approximately the same as for true incoherent scattering. We have analyzed available data for cristobalite, a form of silica (SiO_2), in order to study the changes in the lattice vibrations at low frequencies that occur when the crystal undergoes an order-disorder phase transition at 270°C. This work is described in more detail in Sec. 2.3.1.31 of the present report.

To obtain a benchmark for the work described above, and to test the method used for making multiphonon corrections, we have recently carried out similar experiments on vanadium. As

noted earlier, vanadium is the prototype material for these kinds of studies because (1) it is an almost totally incoherent scatterer and (2) the atoms occupy the sites of a cubic Bravais lattice (the bcc structure) so that, to the extent that multiphonon scattering is negligible, the observed inelastic scattering is directly proportional to the phonon density of states $g(\nu)$. In all other real materials, the effective density of states obtained from such experiments is weighted by the phonon polarization vectors. This work is described later in Sec. 2.3.1.21. Our results are compared with the first experimental paper on this subject by A.T. Stewart and B.N. Brockhouse (Rev. Mod. Phys. **30** (1958), 250). The comparison with this paper is especially relevant at the present time, because it is part of the pioneering work for which Brockhouse was recently awarded the Nobel prize in physics.

2.2 SUMMARIES

Condensed Matter Science

Measurements of the magnetic phase diagrams in rare earth metals continued with the investigation of "lock-in" phases in Ho (2.3.1.1) and Er (2.3.1.2) in magnetic fields. A more detailed examination of the 54 K transition in Er was made, while the effects of magnetic fields on the magnetic structure of two Ho/Lu superlattices were explored (2.3.1.3).

Investigation of heavy-fermion systems involved measurements of the structure of UNi_2Al_3 at high field (8T) (2.3.1.4) and a search for the existence of magnetic domains in UPt_3 (2.3.1.5).

Powder diffraction measurements on annite mica (2.3.1.6) found the highest magnetic ordering temperature reported for any layer silicate structure. Similar measurements on $InMnO_3$ showed that long-range interplanar order is not achieved in this material (2.3.1.7). Two possible magnetic structures were identified for the trirutile system $CuSb_2O_6$ (2.3.1.8).

The magnetic structure of the frustrated antiferromagnet UNi_4B was investigated as a function of magnetic field (2.3.1.9), while its low energy excitations were measured for zero field.

The $DyVO_4$ system, with substitution of As in large concentrations, was investigated. The magnetic ordering was explored for 35% As concentration (2.3.1.10), while for 15% As concentration the roughening of domain walls by the random static fields was measured (2.3.1.11).

The nature of the magnetic transition in the layered rock salt structure of $NaTiO_2$ was investigated with powder diffraction measurements (2.3.1.12). The data suggests the transition is analogous to the metal-insulator transitions.

Critical fluctuations near the magnetic phase transition were measured in the Ising-like antiferromagnet, $CsCoBr_3$ (2.3.1.13). A new theory of the excitation spectrum of the quasi-one-dimensional material $CsNiCl_3$ was tested (2.3.1.14).

Inelastic measurements were made to measure spin waves in $FeGe_2$ (2.3.1.15). The results suggest strong ferromagnetic coupling within the spin chains and weaker antiferromagnetic coupling between chains.

The compositional dependence of the partial structure factors in NiZr metallic glasses was probed by measurements on $Ni_{0.5}Zr_{0.5}$ (2.3.1.16). The low angle, three-body correlation peak was confirmed. The temperature dependence of the static structure factor of $Ca_{0.4}K_{0.6}(NO_3)_{1.4}$ in its liquid and glassy states was explored (2.3.1.17), together with the time dependence of the transformation to a crystalline phase. Inelastic measurements were also made (2.3.1.18), to seek signatures of the liquid-glass transition and to test the predictions of mode coupling theories.

Spin-Peierls transitions were investigated in $CuGeO_3$ (2.3.1.19) and $Pr(OD)_3$ (2.3.1.20). Powder diffraction data from both systems suggested the presence of an SP transition, although one was not observed directly in either.

The phonon density of states was measured in vanadium (2.3.1.21). It is a benchmark test of a new method of correcting for multiphonon effects for comparison with similar work on hydrogenous materials.

A computer program has been developed to calculate the reflectivity of a model layer profile (2.3.1.22). It will be used in the analysis of neutron reflectivity measurements.

Molecular Science

Powder diffraction data from ice grown in an electric field were analyzed (2.3.1.23). The field was found to change the lattice parameter, but to have little effect on the atomic positions of oxygen and deuterium. However, it has a marked effect on thermal parameters of the deuterium atoms.

Investigations were made, by powder diffraction methods, of three ferroelastic systems. For K_2CO_3, a lattice melting, m=2, transition was observed (2.3.1.24). This is due to the total loss of long-range order along the c-axis. In $K_3Na(SeO_4)_2$, a transition from a trigonal to a monoclinic structure was observed at 334 K (2.3.1.25). In $(ND_4)_4\ LiH_3\ (SO_4)_4$, a tetragonal to monoclinic transition was observed at 236 K (2.3.1.26). Efforts are in progress to understand the temperature dependence of the monoclinic angles in terms of Landau theory.

Measurements were continued on the isomorphic systems, $NaNO_3$ and $CaCO_3$. In $NaNO_3$, the tricitical, order-disorder transition at 553 K was found not to be Ising-like (2.3.1.27). Instead, it appears to be the result of continuous librational melting. For $CaCO_3$ (2.3.1.28), it was found that the symmetry of the TA mode at the F-point would lead, on condensation, to a high-pressure form of calcite. It appears that this competing structure may be the cause of the inelastic diffuse scattering observed at F.

Powder diffraction measurements on the zeolite H-SAPO-37 containing perdeuterated benzene (2.3.1.29) found the benzene to locate above the 6-ring window and in the plane of the 12-ring window. But protons could be located only at the O(2) site.

Neutron powder-diffraction measurements from $CHCl_2F$ (2.3.1.30) showed that the high-temperature phase has space group Pbca. At low temperatures (55 K, 30 K, 5 K) additional peaks are observed, but their origin is not yet understood.

Neutron time-of-flight measurements for the α- and β-phases of cristobalite were analyzed, to derive the phonon density of states, $g(\nu)$ (2.3.1.31). The results are in qualitative agreement with molecular dynamics calculations, except at low frequencies.

Powder diffraction from lithium manganese oxide (2.3.1.32) found the point at which an electrolytic reaction must be terminated to prevent formation of the undesirable product $Mn(OH)_2$.

Materials Science

Residual stresses were measured for several engineered components. Very large compressive hoop stresses were found close to the edge of the hole in a cold-worked and fatigued lug specimen (2.3.1.33). Excessive grain size prevented meaningful analysis of strain measurements in the bulk-head of an engine block (2.3.1.34). Measurements of strain near holes in thin, hot-rolled steel plates, designed to simulate defects in line-pipe, disagreed completely with the predictions (2.3.1.35). The stress pattern measured in welded rails (2.3.1.36) was found to inhibit transverse cracks starting at the surface of the rail, a very beneficial configuration. Extrusion of rods of the metal-matrix composite Al:SiC was found not to generate a macroscopic residual stress field (2.3.1.37). The observed stresses are due only to interphase constraints. Residual stresses were measured near the interface of a SiC/Mo ceramic-metal joint (2.3.1.38). The results show that the stresses increase with the bonding temperature. The residual axial strains in an extruded aluminum bar were found to exhibit a pattern typical of a quench (2.3.1.39). The pattern of texture is linked to the streamlines of the metal flowing through the extrusion die. The three principal strains were measured in the Al matrix of a mullite-reinforced piston head (2.3.1.40). Stresses in the reinforced region were found to be tensile, decreasing to zero in the pure Al region of the casting. Details of the load transfer were made on Ti tensile samples reinforced with SiC fibres (2.3.1.41). At zero load in the Ti matrix large compressive strains are found due to the transfer of stress to the SiC phase. The strain distribution was measured along the fatigue crack axis in particulate reinforced Al (2.3.1.42). In the fully closed condition, the observed tensile stress explains the reduction in fatigue crack growth in metal-matrix composites. Lattice parameters were measured in the extrusion and transverse directions in both the Al(Cu) and the SiC phases in extruded SiC particulate reinforced Al(Cu) (2.3.1.43). Significant asymmetry was found in the residual strains and this is thought to be due to alignment of the particles. A neutron diffraction technique has been developed to probe continuously from the surface into the bulk (2.3.1.44). The method was tested on samples of shot-peened WASPALOY.

Linewidths were measured for plastically deformed HY-80 steels (2.3.1.45). The variation of linewidth with plastic strain was described by an exponential function. No change in linewidth was found for fatigued samples.

Two studies were made of textural characteristics. The evolution of recrystallization texture of an Al alloy was studied as a function of hot deformation parameters (2.3.1.46). Deformation temperature and total strain were found to affect the texture, whereas the strain rate did not. The texture of the α- and β-phases of CANDU pressure tube material were measured simultaneously. The texture of the δ (hydride) phase was also measured (2.3.1.47). The texture of the metal phases was typical of extruded or drawn materials. That of the hydrides was typical of drawn fcc metals.

The time dependence of the oxidation of iron at 1200°C was investigated by powder diffraction (2.3.1.48). The variation of the intensities of the diffraction peaks measures the growth rate of the many iron oxides.

The lattice parameter in a stainless steel weldment was measured as a function of position in the fusion zone (2.3.1.49). The diffraction pattern was also analyzed to determine the volume fraction of ferrite as a function of position.

Multiple scattering was found not to be a cause of aberrations in strain measurements in thick plates (2.3.1.50), but wavelength-dependent effects are important.

Powder diffraction measurements provided the first direct evidence that the metastable anstenitic phase disappears in TRIP steels under large compressive strain (2.3.1.51).

The properties of a two-phase magnesium alloy subjected to applied loads were investigated by neutron diffraction (2.3.1.52). The data suggests that the deformation mechanism involves twinning of the magnesium matrix.

The feasibility of measuring the statistical distribution of magnetic domain orientations in motor core steel was investigated by polarized neutron experiments (2.3.1.53). The magnetic scattering dominates the difference in the intensities of the pole figures measured for two different polarization configurations.

The temperature dependence of the detailed structures of B2-type NiAl alloys was measured by powder diffraction (2.3.1.54). The data for the stoichiometric alloy shows no vacancies or antisite defects are present at temperatures below 1000°C.

A theory to predict the sublattice on which a third component of a binary alloy will locate was tested by application to the binary $L1_2$ ordered alloys Al_3TiX (X = transition metal) (2.3.1.55). After corrections, the theory correctly predicts that, for the five alloying elements studied, all should locate on the Al sublattice.

The temperature dependence of the lattice parameters of α-Zr up to 850 K were measured for use in modelling the residual stresses in extruded and annealed pressure tubes (2.3.1.56). Both lattice parameters were found to vary linearly with temperature.

Theory

A model Hamiltonian was proposed for the heavy-fermion compound URu_2Si_2 (2.3.1.57). It gives a qualitative explanation for the temperature dependence of the specific heat jump at the Néel temperature.

Neutron scattering lengths are discussed in two reports. The experimentally determined values for the bound coherent and incoherent scattering lengths have been updated (2.3.1.58), and two simple methods were developed to correct the scattering lengths for electromagnetic interactions (2.3.1.60). This interaction depends on the atomic form factor. A new method of calculating the form factor from the Thomas-Fermi equation was obtained (2.3.1.60).

Work on the polaron properties of the Holstein model of electron-ion interactions was continued (2.3.1.61). Calculations were carried out utilizing weak coupling and strong coupling expansions

and also the adiabatic approximation. A very different model for electron-ion interactions is also being investigated (2.3.1.62).

Calculations of the upper critical field have been made for high T_c superconductors, in an attempt to explain the positive curvature as a function of temperature (2.3.1.63).

Calculations were also made to explain recent high-precision microwave measurements on superconducting Nb. The BCS-like coherence peak below T_c remains anomalous (2.3.1.64).

A new theory has been developed to solve the Heisenberg quantum spin chain (2.3.1.65). Work is in progress to propose an experimental verification of the theory. A braided version of this Hamiltonian has been developed (2.3.1.66) and diagonalized. The solution of the resulting Bethe equations is being sought. New examples of braided Hopt algebras have been found (2.3.1.67) and an example discussed in the context of the recently formulated general theory.

Neutrino Physics

The levels of ^{232}Th in materials for the SNO detector continue to be monitored (2.3.2.1). Some Th is observed to be introduced during the thermoforming of the acrylic, but the level remains below specifications. A test facility has also been constructed and installed to check for contamination of the D_2O to be used in the detector (2.3.2.2).

A prototype plant has been built to test the procedures for coating acrylic beads with MnO_2 (2.3.2.3). A prototype system has been assembled to turn the recently developed radon cryodetectors from experimental devices into semi-automated instruments (2.3.2.4).

A system to deliver short-lived radioactivities, by gas transport, to calibrate the SNO detector has been developed (2.3.2.5). The calibration schemes have been successfully tested and the design and operating parameters optimized.

The Chalk River SNO group has joined the data simulation and analysis software team (2.3.2.6).

Nuclear Data and Modelling

One advanced fuel concept under investigation uses a high-temperature coefficient absorber in slightly enriched uranium fuel. The temperature coefficients were calculated for eleven possible absorbers as a function of neutron energy (2.3.3.1).

Calculations were made to evaluate the optimum configurations of a high-power bremsstrahlung converter for radiation processing, using IMRELA. The angular and spectral distributions of bremsstrahlung and electrons from medium Z and high Z materials were computed (2.3.3.2).

The dynamics of several concepts for the production of fission ^{99}Mo were investigated (2.3.3.3).

Instrumentation

The single excitation scattering by superfluid ^{4}He has been used to determine accurately both the angular resolution and the time resolution of the IRIS time-of-flight (TOF) spectrometer (2.3.4.1). Previously, there has been no standard procedure for determining the wave-vector resolution for TOF spectrometers.

Significant upgrades are being carried out on the T3 small-angle scattering spectrometer (2.3.4.2). These include replacement of air by helium for all neutron beam paths, and a rebuilt specimen environment and positioning system.

The specifications for a jib crane were completed, with particular application for ANDI measurements (2.3.4.3). A suite of set-up utilities was fabricated to aid in alignment of the sample (2.3.4.4). An XYZ translation system was assembled for the stress rig (2.3.4.5).

Software was installed that enables remote monitoring of a neutron experiment (2.3.4.7), and an additional mode was added to the DUALSPEC control program. The switches controlling the DUALSPEC beam gate were successfully replaced (2.3.4.8).

Support Services

A 32-wire, grounded anode detector with 2 mm wire spacing, was completed and put into service with the ANDI group (2.3.5.1). Its performance has exceeded all expectations and two further models are under construction.

Two electronic communication services were established (2.3.5.4), ANDInet and CINSnet. Each provides a single electronic mail address that is used to direct e-mail to all net members. ANDInet is for the ANDI group, while CINSnet is for all members of the Canadian neutron scattering community.

Work in the Mechanical Laboratories (2.3.5.5) included components to complete the stiff link for the C2 spectrometer, components for the upgrades to the T3 spectrometer, components for ANDI experiments and both multiwire and fast-neutron spherical detectors.

Alumina columns and recovery headers were produced by the Glassblowing Laboratory for the ^{99}Mo program (2.3.5.6). Two closed circulating systems with a glass impeller were fabricated, and small holes (0.004" and 0.007") were drilled in the glass wall of pyrex cells. Glass hooks were fabricated for burst tests on calandria tubes, and two electrolysis cells were constructed for an IAEA contract.

2.3 INDIVIDUAL REPORTS

2.3.1 Condensed Matter Science

Physics

2.3.1.1 Lock-In Phenomena in Holmium

Z. Tun and T.M. Holden *(AECL)*, D.A. Tindall, C.P. Adams and M.J. Small *(Dalhousie University)* and M.O. Steinitz *(St. Francis Xavier University)*

The M2 magnet mounted on the N5 spectrometer has been used to investigate the magnetic phase diagram of holmium in its spiral antiferromagnetic state between 30 K and 132 K, in magnetic fields up to 3 T applied along the b- and c-axes. At a number of commensurate values the wave-vector of the spiral, τ, as a function of temperature, "locks-in", rather than smoothly increasing as it does in zero field. Some of these commensurate values are simple rational fractions, others not so "simple"; for example, in a b-axis field just below T_N(132 K) the τ reported in 1979 by J.A. Tarvin and J. Eckhert (Solid State Comm. **30**, 375) was 8/29 (0.2759), whereas we obtained 0.2773, which we suspected was closer to 5/18 (0.2778). This raised a challenging task: could we distinguish 0.2759 from 0.2778? There are two major problems to be overcome to achieve this: a) by careful design of the experiment we had been able to reduce the width (FWHM) of our neutron peaks to about 0.007 rlu (reciprocal lattice units, along the c* direction); b) the thermal expansion of holmium is very large so, with a spectrometer control program that accepts only constant values for the lattice parameters, it is very difficult to obtain *absolute* values of the peak positions to better than 0.005 rlu -- clearly insufficient for the present purpose. In fact, even though the peak widths were 0.007 rlu, the scans over the peaks, coupled with the fitting technique that has been developed, gave values for *changes* in the peak positions that were accurate to 0.0001 rlu.

We believe the results shown in Fig. 2.3.1.1 are the most precise determinations of the helimagnetic spiral wave vector ever made. What is the significance of knowing whether the observed value of τ, 0.28, is really 5/18 or 8/29, or some other rational fraction with an even bigger denominator? There is a fundamental difference between these values in the theoretical models that we are now developing to account for the lock-ins. Our hope is that a careful study of the commensurate values that are observed, and at which field orientations they occur, will give us a deeper understanding of the underlying interactions that cause the complicated phase diagram. Fig. 2.3.1.2 shows a lock-in value of 2/9, which we observed at 75 K in a b-axis field of 1.4 T. This is interesting because it is far away from any line on the known phase diagram.

As noted above, the magnetostriction and thermal expansion of holmium are very large, which makes accurate measurements of τ a time-consuming *tour-de-force* with the standard spectrometer control program, based on fixed lattice parameters. Therefore, an alternative, peak-finding program is being developed. Preliminary results, in which we measured the lattice parameter of holmium as a function of temperature in b- and c-axis magnetic fields, are encouraging.

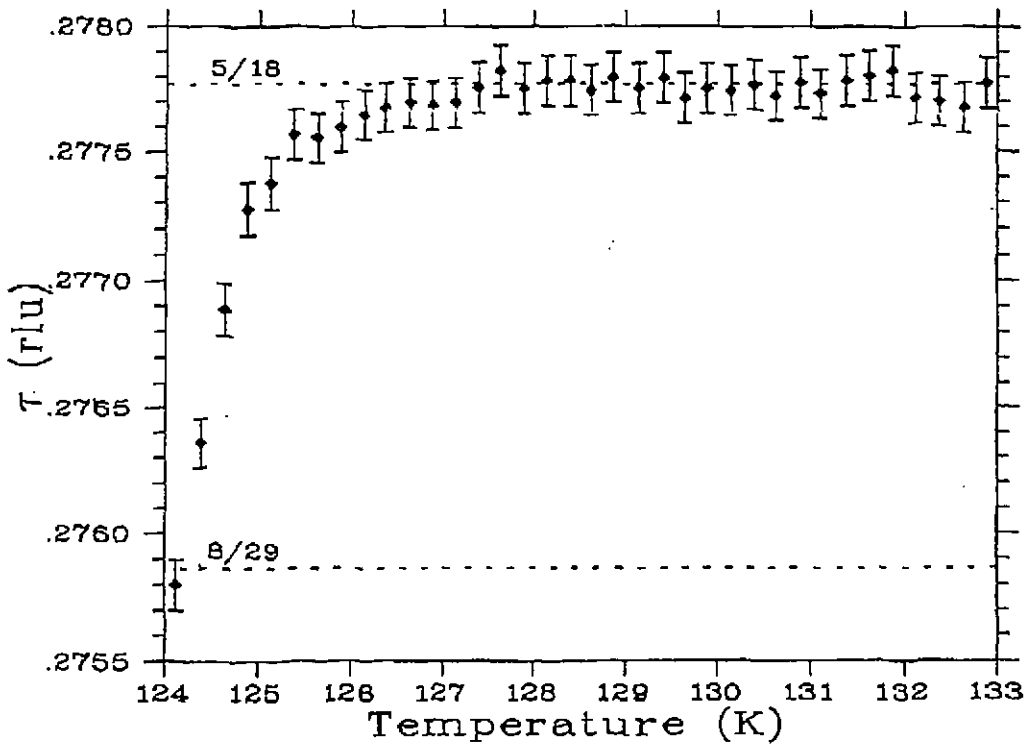

Fig. 2.3.1.1 The 5/18 lock-in of the helimagnetic spiral wave vector τ.

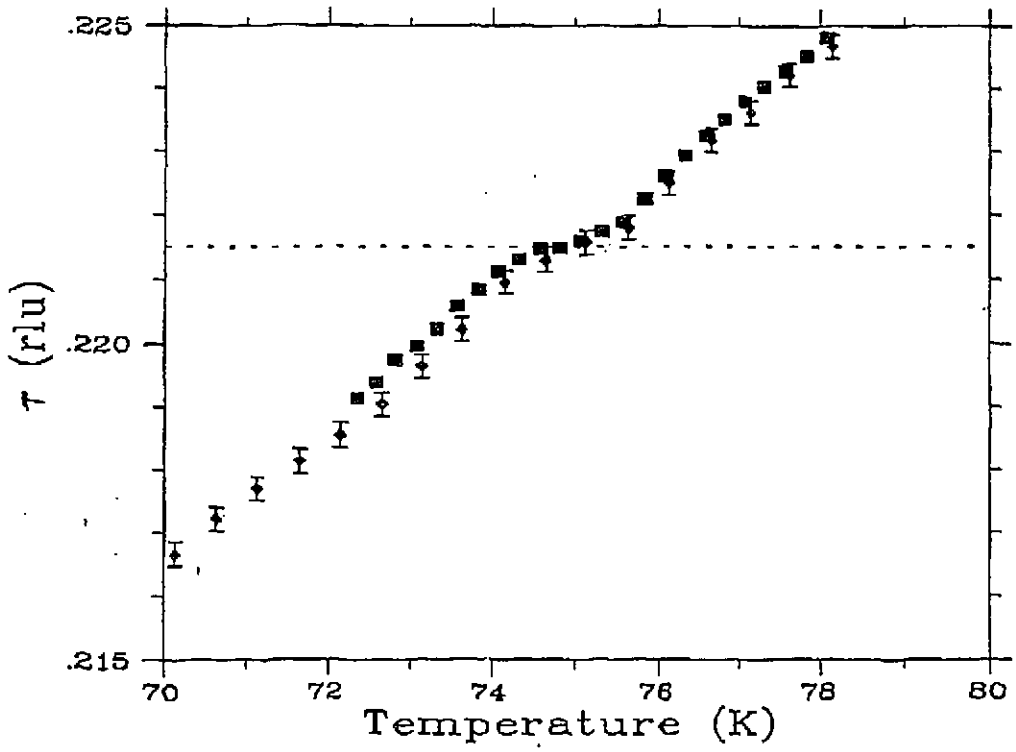

Fig. 2.3.1.2 The variation of τ with temperature around the 2/9 lock-in.

2.3.1.2 An Investigation into the 54 K Phase Transition and the 2/7th Lock-In in Er

P.P. Swaddling and R.A. Cowley *(University of Oxford)*, D.F. McMorrow *(Risø National Laboratory)*, M.F. Collins *(McMaster University)* and W.J.L. Buyers *(AECL)*

The examination of the 54 K phase transition in Er comprised measurements of the (00q), (10q), (002-q) magnetic peaks and the associated higher harmonics over a temperature range 53 -63 K. In Fig. 2.3.1.3, the intensity of the first-order magnetic peaks is plotted as a function of temperature. A significant amount of scattering was observed at (00q) above the transition temperature, while the scattering around (002-q) was relatively large, but only slowly varying. (It is thought that the scattering around (002-q) is mainly multiple.) Based on the scattering around (00q), we believe that there is a small ordered magnetic component in the a-b plane above 54 K. The increase in intensity is similar to that observed in a previous experiment, although observed at a slightly lower temperature. However, the transition to the low-temperature phase is also observed at a slightly lower temperature, and so we attribute this difference to a difference in temperature calibration between the two experiments.

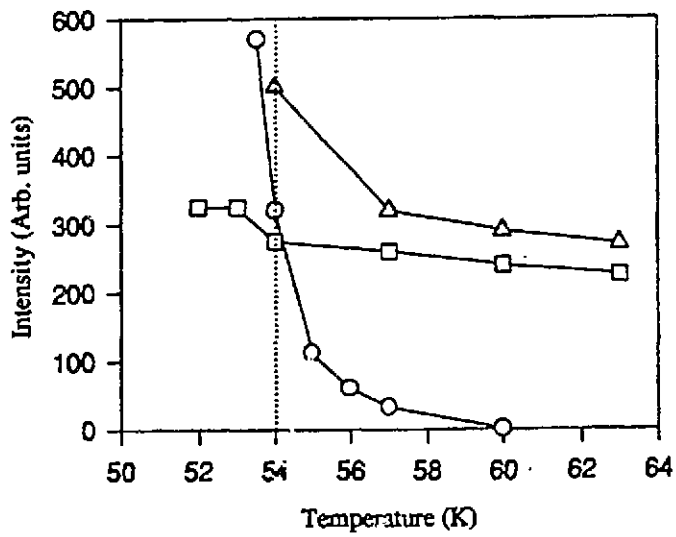

Fig. 2.3.1.3 The intensity of the (00q) - circles, (10q) - squares and (002-q) - triangles vs the temperature.

As a continuation of a previously unfinished experiment to map out the higher temperature region of the phase diagram in Er, we used the horizontal field magnet M2 to map out the extent of the 2/7ths phase in Er in a c-axis field. The measurements concentrated on scans around the (10q) magnetic Bragg peak, which were used to produce the completed diagram shown in Fig. 2.3.1.4. As can be seen, the 2/7ths lock-in phase is substantially stabilised by the presence of the magnetic field. This is believed to arise from the fact that this phase, with four moments pointing along c and three moments in the opposite direction, has a net ferromagnetic moment

along c leading to a relative reduction of energy in the field compared to the neighbouring phases. The result is that a lock-in that is 1 K wide in zero field is stabilised to having a width of 35 K in a field of 2 T.

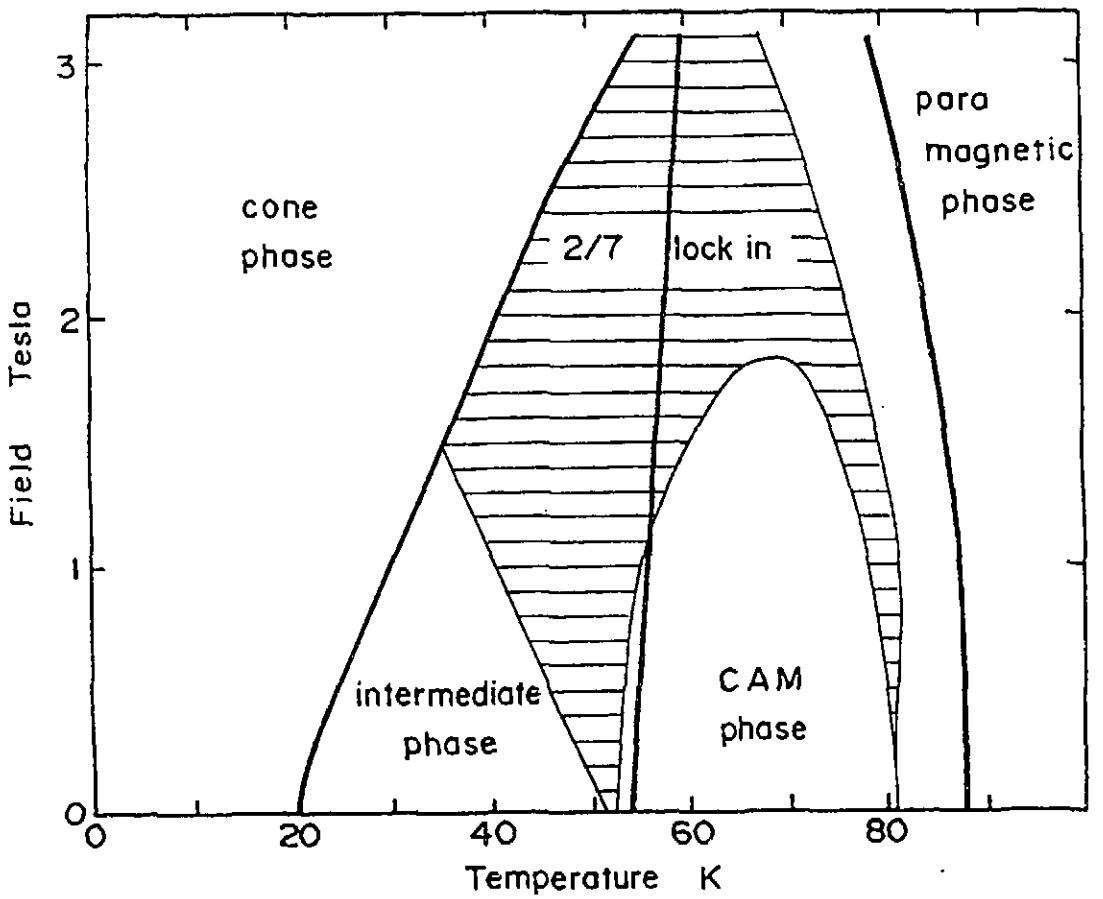

Fig. 2.3.1.4

2.3.1.3 **The Phase Diagram of Ho/Lu Superlattices**

P.P. Swaddling and R.A. Cowley *(University of Oxford)*, D.F. McMorrow *(Risø National Laboratory)*, M.F. Collins *(McMaster University)* and W.J.L. Buyers *(AECL)*

We have measured the effects of both basal plane and c-axis magnetic fields on the magnetic structure of two Ho/Lu superlattices. The samples $Ho_{40}Lu_{15}$ and $Ho_{20}Lu_{10}$ were chosen for the study. The investigation into the latter was motivated by the discovery of a ferromagnetic phase at low temperatures. In this phase the adjacent Ho blocks are antiferromagnetically coupled and we wished to examine the strength of the coupling between adjacent layers. The $Ho_{40}Lu_{15}$ remains in a helical phase down to low temperatures. We were particularly interested in determining the relative stability of this phase and the ferromagnetic phase, which would presumably be observed for sufficiently high fields. To determine the structures present we

performed scans around (002) and (100), along the [001] direction, and over the temperature range 4-140 K. The resulting phase diagrams measured at constant field and for increasing temperature are shown in Figs. 2.3.1.5(a) and 2.3.1.5(b) for the samples in a basal plane field. For sufficiently high fields, both samples are, as expected, ferromagnetically aligned. As the temperature is raised, both samples undergo a transition to a helically ordered phase, with $Ho_{40}Lu_{15}$ passing through an intermediate fan phase (this phase is not observed on cooling). Scans were then made at constant temperature, stepping up in field, to determine the low-temperature transition to a ferromagnet. $Ho_{40}Lu_{15}$ passed directly into a ferromagnetic phase at 0.25 T, but on reducing the field to zero the helical phase was not recovered until the sample was taken to higher temperatures. For $Ho_{20}Lu_{10}$, the zero-field low-temperature phase was driven ferromagnetic at 0.3 T but, in contrast to the previous case, was regained on returning the field to zero. $Ho_{20}Lu_{10}$ was also examined for a c-axis field. Here it was established that as the field increased above 1 T, the stability of the ferromagnetic phase was lost, and the helical phase became more favourable.

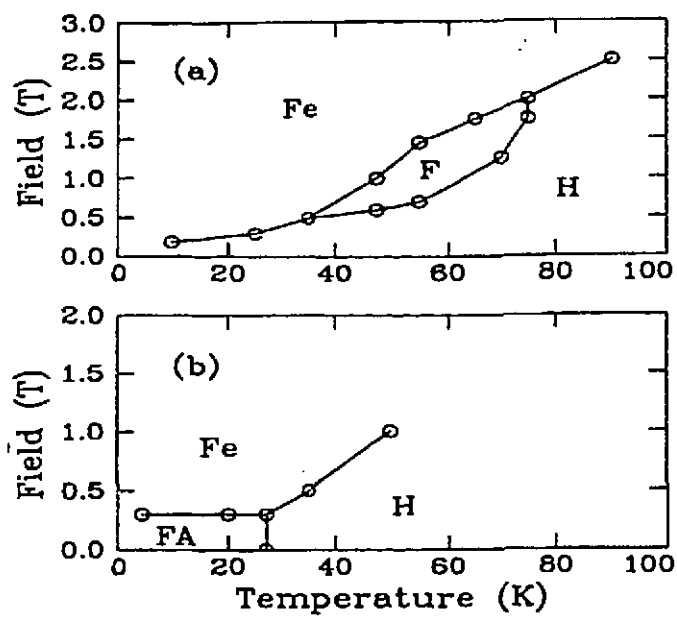

Fig. 2.3.1.5 The magnetic phases of (a) $Ho_{40}Lu_{15}$ and (b) $Ho_{20}Lu_{10}$ in a basal plane magnetic field. Fe - ferromagnetic coupling, H -basal plane helix, FA - ferromagnetic ordering with antiferromagnetic coupling between blocks and F- fan phase.

We also attempted to measure the coherence length of the helically ordered phase of $Ho_{40}Lu_{15}$ close to T_N. It was found that, to within the sensitivity of the experiment, the coherence length remained constant as a function of temperature up to 1 K below the Néel point. This is a surprising result, in view of the coupling mechanism, which is thought to occur across the Lu blocks. It would be expected that the individual Ho layers would order separately, and then at the point where the developing moment is sufficiently large the separate blocks would co-operatively order.

2.3.1.4 Magnetic Structure of UNi_2Al_3 in High Magnetic Fields

J.G. Lussier, A. Schröder and B.D. Gaulin *(McMaster University)*, W.J.L. Buyers and Z. Tun *(AECL)*

We have extended our earlier elastic neutron scattering measurements of the heavy fermion superconductor UNi_2Al_3 to include measurements in applied magnetic fields up to 8 T. These measurements made use of M3, the high vertical field magnet cryostat.

Our earlier zero-field measurements showed that this material underwent a phase transition at a Néel temperature of 4.6 K to an incommensurate magnetic structure. Our new measurements show that while both the intensity of the magnetic Bragg peaks and their positions (hence the incommensurate wavevector) change appreciably on application of the magnetic field, the Néel temperature does not. In addition, the temperature dependence of the ordering wavevector is strongly field dependent. It seems that qualitatively different behaviour is seen for fields above and below $H_c \sim 4$ T. Finally, as expected, additional magnetic scattering is observed at the nuclear Bragg positions in the presence of high magnetic fields. However, this excess scattering has a very interesting **Q**-dependence, which is not consistent with the expectation of a simple ferromagnetic canting of the moment along the field direction.

2.3.1.5 Test for Existence of Magnetic Domains in the Heavy Fermion Superconductor UPt_3

B. Lussier and L. Taillefer *(McGill University)*, T. Petersen *(Risø National Laboratory)*, T. Mason *(University of Toronto)* and W.J.L. Buyers *(AECL)*

Theories of the field dependence of the anisotropic superconductivity in UPt_3 assume that there are three independent domains of antiferromagnetic order below the 6 K Néel temperature. Similar assumptions have been used to account for the angular anisotropy of the resistivity near the upper critical field. We searched for evidence that the transition was to a single-**q** structure. There should then be three independent magnetic satellites with wave vectors related by the 120 degree rotation symmetry of the hexagonal structure; moreover, one of these domains could be selected by applying a horizontal field from the M2 cryostat along a <110> direction perpendicular to $\mathbf{q} = (\frac{1}{2}00)$. An experiment was carried out at DUALSPEC on a very small but high-quality single crystal at 1.8 K and 10 K. The satellites caused by the weak magnetic order were examined with a highly filtered neutron beam of energy 3.52 THz. Notwithstanding the difficulty of the experiment, it was seen that no change occurred at any of the equivalent satellite positions in fields up to 3 Tesla, much larger than the field required for spin flop, according to prior theory. We conclude that theories of the superconductivity based on independent magnetic domains are not in accord with experiment. It is possible that UPt_3 undergoes a transition to a triple-**q** state instead of the single-**q** state assumed to date, or that the crystalline anisotropy is much larger than had been expected.

2.3.1.6 The Magnetic Structure in Annite Mica $K_2Fe_6Al_2Si_6O_{20}(OH)_4$

I.P. Swainson *(AECL)* and D.G. Rancourt *(Université d'Ottawa)*

Annite, $K_2Fe_6Al_2Si_6O_{20}(OH)_4$, is the Fe-endmember of the biotite--phlogopite solid solution micas, $K_2(MgFe^{2+})_{6-4}(Fe^{3+},Al,Ti)_{0-2}(Si_{6-5}Al_{2-3}O_{20})(OH,F)_4$. The unit cell is a pseudo-hexagonal C2/m monoclinic cell of dimensions a = 5.3 Å, b = 9.2 Å, c = 10.3 Å and β = 100°. The structure of these micas consists of an Fe--O octahedral layer, sandwiched between two $(Si,Al)O_4$ tetrahedral layers, and this composite sandwich is then weakly bonded by K atoms to form a layer compound with a repeat of ca. 10 Å. No direct magnetic exchange mechanism is possible over such a large distance. This strong anisotropy between relatively strong in-plane exchange and relatively weak out-of-plane interactions (10 to 50 times weaker) makes the magnetic order in the micas a good candidate for natural 2D magnetism.

Recently, powder experiments were performed on synthetic pure end member composition annite using the C2 DUALSPEC powder diffractometer. Very strong (0, 0, 1/2) and (0, 0, 3/2) peaks have been observed at 5 K (D.G. Rancourt, I.A.D. Christie, G. Lamarche, I. Swainson and S. Flandrois, J. Magn. Magn. Mater. **138** (1994), 31). This demonstrates that the magnetic spins in annite lie in the (001) planes and are antiferromagnetically ordered up the c* layer axis. Mossbauer and SQUID measurements have suggested that this order is metamagnetic-like, and that T_c = 58 K (D.G. Rancourt et al., *loc. cit.*). This is the highest T_c reported for any layer silicate structure.

The extent of cation disorder in most natural micas prevents magnetic ordering from occurring in these natural 2D magnets. This rules out the use of most natural single crystals in order to determine the orientation of the magnetic moment in the layer, or to examine the dynamics of the magnetic order. However, we possess a natural single crystal from St. Hilaire, Quebec (Sample M42126, Royal Ontario Museum), which is the largest, most Fe-rich biotite sample known, and which has been shown to order magnetically (D.G. Rancourt et al., *loc. cit.*). Polarised triple-axis measurements of this sample are in progress on C5 to determine the orientation of the moment in the (001) plane.

2.3.1.7 Magnetic Structure of $InMnO_3$

J.E. Greedan and R.L. Donaberger *(McMaster University)*, H.C. Zur Loye and D. Gia Quinta *(Massachusetts Institute of Technology)*

Powder diffraction data were collected on the DUALSPEC powder diffractometer with λ = 2.5 Å at one detector setting, and at several temperatures between 5 K and 130 K. Preliminary results from McMaster University had indicated a possible magnetic phase transition near 120 K. The crystal structure was believed to be isostructural with $YALO_3$ ($P6_3/mmc$) on the basis of single crystal X-ray results. The single crystals and polycrystals had been prepared by different methods.

The first observation was that for high temperatures, T = 130 K, it was necessary to choose a larger unit cell of symmetry $P6_3cm$ and cell constants á = ¦3a, ć = c relative to the $P6_3/mmc$ cell.

This cell was then confirmed by careful analysis of the X-ray powder diffraction pattern. The structure is shown in Fig. 2.3.1.6.

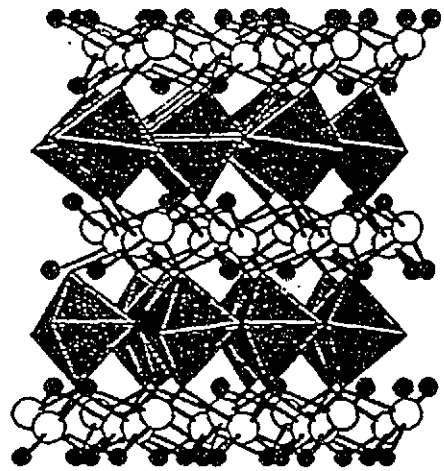

Fig. 2.3.1.6 The layered structure of $InMnO_3$. The MnO_5 trigonal pyramids are shown in polyhedral form, the large open circles are In and the small filled circles are O.

The low-temperature patterns showed super cell reflections with indices (h0ℓ/2), h=1,2 and (h1½), h=1,2 which displayed rather unusual temperature dependencies, Fig. 2.3.1.7. Closer inspection of the (h0ℓ/2) reflections indicated line widths which were always greater than the resolution-limited widths. This indicates that true long-range interplanar order is not achieved in this material.

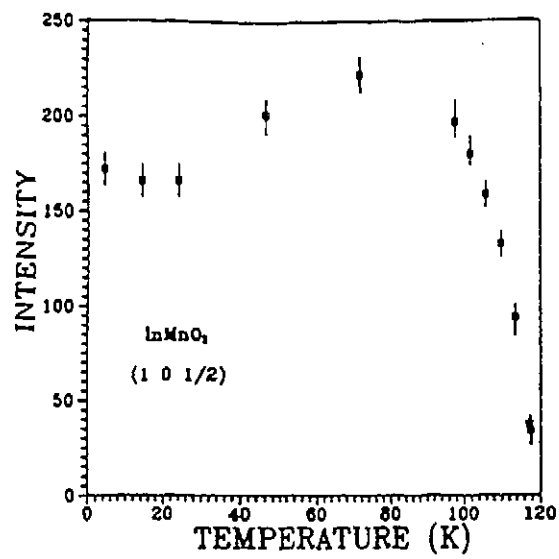

Fig. 2.3.1.7 The unusual temperature dependence of the (10½) reflection and an apparent $T_c \approx 118$ K.

For temperatures T > 120 K the ½ super cell lines vanished, but a prominent broad feature remained, which could be described in terms of a Warren-type line shape, indicating two-dimensional correlations. This peak could be indexed as a (100) reflection and thus it describes intraplanar magnetic correlations. For T< 120 K the overlapping (100) and (10½) reflections were deconvoluted using Warren and Gaussian line shapes, respectively. A key parameter to be extracted from the Warren analysis is the two-dimensional correlation length. The temperature dependence of this length is shown in Fig. 2.3.1.8, where it increases from ~ 4 Å at room temperature (complementary data from the McMaster experiments were used to construct this curve) to about 50 Å at 5 K. Thus, there is no long-range intraplanar order, either, in $InMnO_3$.

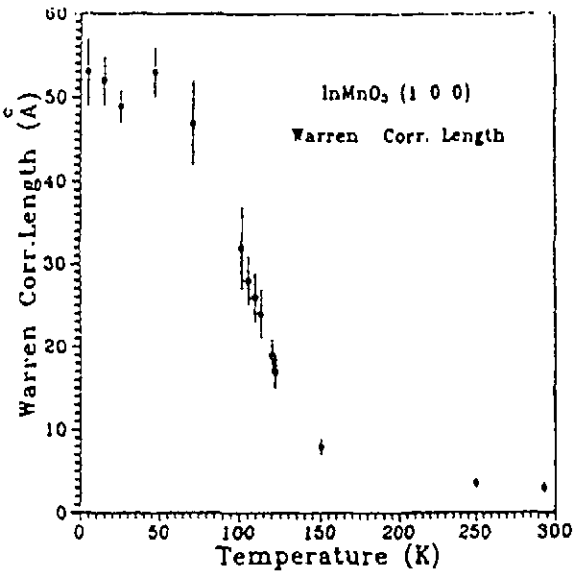

Fig. 2.3.1.8 Temperature dependence of the Warren correlation length.

This situation is in sharp contrast to that for isostructural $LuMnO_3$ and $ScMnO_3$, which show a magnetic long-range order below 90 K and 127 K, respectively, of the 120° or triangular type. The difference between $InMnO_3$, on the one hand, and $LuMnO_3$, on the other, is traceable to the nature of the bonding about the diamagnetic ion. In both cases, the coordination is 8-fold, but for In there are six shorter In-O bonds and two longer ones, whereas for Sc and Lu the eight bonds are similar in length. The main interplanar superexchange pathway involves one of these long bonds, Mn-O-In-O-Mn, so this pathway is much weaker in $InMnO_3$ than the other two materials. Since LRO is not possible in two dimensions for Heisenberg ions (Mn^{3+},S=2), interplanar coupling of some minimum strength is necessary for LRO. These results have been compared to recent mean field theory for stacked, hexagonal antiferromagnets (J.N. Reimers and J.R. Dahn, J. Phys. Condens. Matter 4 (1992), 8105).

2.3.1.8 Low-Temperature Crystal and Magnetic Structure of $CuSb_2O_6$ - a Linear Chain Antiferromagnet

J.E. Greedan, R.L. Donaberger and A. Nakua *(McMaster University)*

At room temperature, $CuSb_2O_6$ crystallizes in a slightly distorted form of the trirutile structure, space group $P2_1/n$. In spite of the fact that the magnetic Cu^{2+} ions are arranged in layers, this compound shows significant short-range magnetic order, which is clearly one-dimensional in form. Also, there is a sharp decrease in the magnetic susceptibility at about 9 K, which could be due either to the onset of long-range AF order or even to a spin-Peirels transition, which is not impossible in a linear chain antiferromagnet.

To investigate the low-temperature properties of $CuSb_2O_6$, neutron powder diffraction data were collected on the DUALSPEC powder diffractometer at 5 K and 12 K. One superlattice reflection is observed in the low-temperature data which can be indexed as (½ 0 ½) on the chemical cell, Fig. 2.3.1.9. This is consistent with a magnetic propagation vector of $\vec{q}$ = (½ 0 ½). Magnetic structures with such propagation vectors have been found for the trirutile oxides $CuSb_2O_6$ and $FeTa_2O_6$ (J.N. Reimers, J.E. Greedan, C.V. Stager and R.K. Kremer J. Solid State Chem. **83** (1989), 20). The temperature dependence of this reflection is also consistent with a T_N = 9 K.

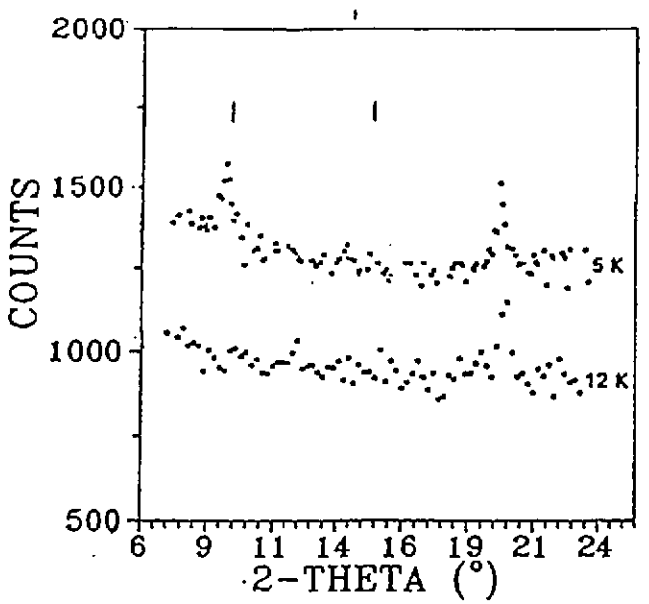

Fig. 2.3.1.9 Neutron diffraction data at 5 K and 12 K for $CuSb_2O_6$. The low angle reflection can be indexed as (½ 0 ½) on the chemical cell.

Although, with only one magnetic reflection, there exists a certain level of uncertainty, we can assign tentatively a magnetic structure, which is one of the two illustrated in Fig. 2.3.1.10 (the two are indistinguishable from powder data alone).

There is no evidence of a structural distortion below T_N to within the resolution of the experiment. The magnetic moment on Cu^{+2} at 4.5 K is estimated to be 0.5 μB.

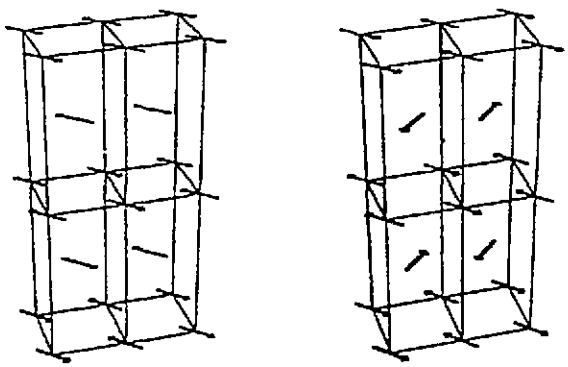

Fig. 2.3.1.10 Possible magnetic structures consistent with a propagation vector of (½ 0 ½).

2.3.1.9 **Magnetic Structure and Low-Energy Excitations in the Frustrated Antiferromagnet UNi_4B**

S.A.M. Mentink and T.E. Mason *(University of Toronto)*, B.A. Mydosh *(Leiden University)* and W.J.L. Buyers *(AECL)*

The hexagonal compound UNi_4B orders antiferromagnetically below 20 K with ordering wave vector $Q = (\frac{1}{3}\ 0\ 0)$ in terms of the basic hexagonal unit cell. A complicating factor is the occurrence of a crystallographic superstructure, enlarging the real unit cell by a factor of 9. We performed elastic and inelastic neutron scattering on a large single crystal with scattering vector in the (h k 0) plane using the horizontal field magnet M2 and, in zero field, in the (h 0 *l*) plane. The incident energy used was mainly E_i = 3.52 THz. A few runs were also taken with E_i = 2.3 THz. Further data were taken, without analyzer, with E_i = 4.36 THz.

Elastic Scattering

In the (h k 0) plane we have confirmed the presence of various $(\frac{h-k}{3}, \frac{h+k}{3}, 0)$ reflections, which led to the determination of the magnetic structure in experiments at Petten on a different, smaller crystal. After subtraction of a flat background, the derived critical exponent for the magnetic ordering at T_N = 20.6(1) K is β = 0.32(1), as expected for a 3D-XY type of ordering. This critical behaviour did not change in fields up to 2.5 T, still well below the first spin-reorientation transition at 7 T.

The peak intensities of five magnetic and two superstructural reflections were examined in horizontal fields up to 2.5 T parallel to the (100) and (110) axes. Due to the occurrence of non-ordering, or induced-moment, magnetic sites in the lattice, extra intensity is expected to develop with field at the superstructural reflections. Significant intensity changes with applied field were found for the ($\frac{2}{3}$ 0 0) and ($\frac{4}{3}$ 0 0) reflections. While their intensities both decrease by about 7% at 2.5 T for $B \parallel (100)$, they behave differently for $B \parallel (110)$. There, a 10% decrease for ($\frac{2}{3}$ 0 0) is accompanied by a 15% *increase* of ($\frac{4}{3}$ 0 0), see Fig. 2.3.1.11. An explanation may have to be found in the formation of a rather complicated magnetic structure in these fields, for which a more elaborate study is needed.

In the (h 0 *l*) zone at zero field, the correct magnetic Bragg peaks were found, but the earlier observation of small superstructural reflections of the type ($\frac{n}{3}$ 0 1), n = 1 and 2 could not be confirmed.

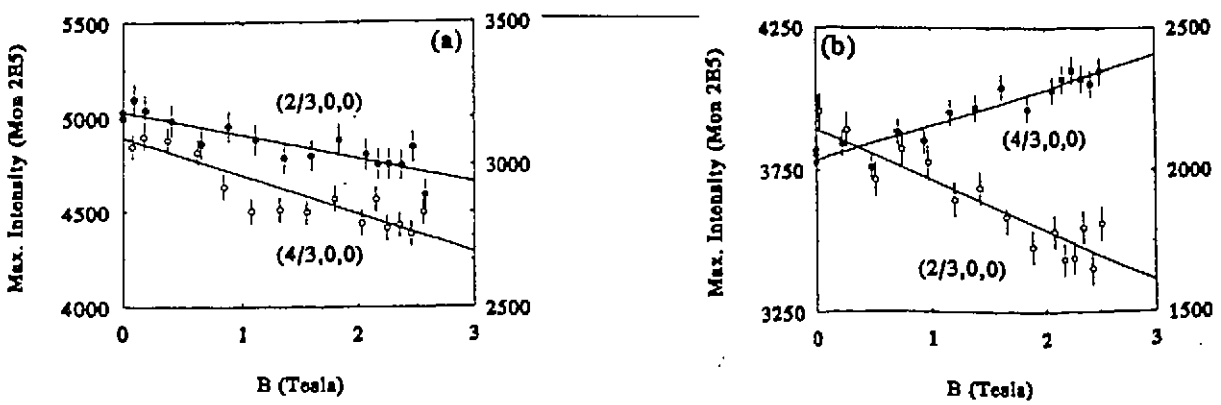

Fig. 2.3.1.11 Field dependence of the maximum intensities of the magnetic ($\frac{2}{3}$ 0 0) and ($\frac{4}{3}$ 0 0) reflections at 4.2 K for (a) field $B \parallel (100)$ and (b) $B \parallel (110)$.

Inelastic Scattering

The inelastic scattering was investigated in zero field in both zones. Scans with either constant energy or constant momentum transfer were performed along various high-symmetry trajectories. A broad inelastic signal was observed as is typical for uranium intermetallic compounds due to hybridization effects. Superimposed on this background, real excitations are inferred from weak extra intensity at 4.2 K at rather high energies, 3.4 THz at $Q = (\frac{4}{3}, 0.2, 0)$ and 4.5 THz at $Q = (\frac{5}{3}, 0, l)$, for l in the range 0.8 to 1.0. An important conclusion we can draw from the inelastic experiments in the (h 0 *l*) zone is the absence of strong one-dimensional fluctuations, as was proposed on the basis of bulk magnetic and transport measurements. Such fluctuations would have led to a large inelastic response, modulated along the l direction. This was not observed.

To obtain a broad overview of the inelastic response, the (h 0 *l*) zone was also investigated without an analyzer, thus measuring excitations integrated over a range of energies. Bragg scattering was reduced by a factor 34, by using a pyrolytic graphite filter in the scattered beam, and an incident energy of 4.36 THz, so that it is strongly attenuated by the graphite (see Fig. 2.3.1.12). An anomalous response is observed, asymmetric with respect to the zero-field magnetic structure, which is different for $l = 0$ and $l = 2$, although it is expected to be the same for antiferromagnetic ordering. The Bragg-like peaks found on the $(\frac{n}{4}\ 0\ l)$ sites with integer n and $l = 1$ or 3 are likely due to higher order neutrons, that were not filtered in this configuration.

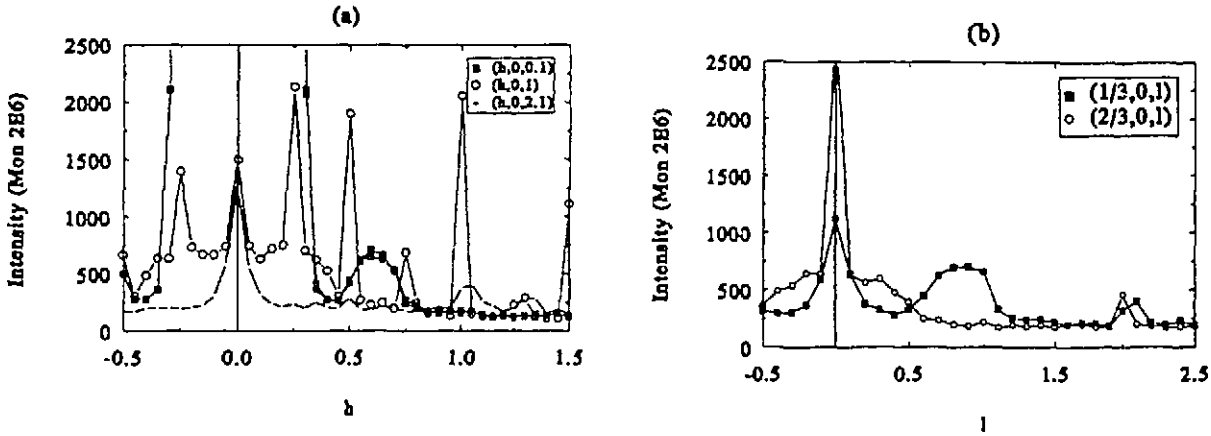

Fig. 2.3.1.12 Constant energy scans in the (h 0 *l*) zone at 15 K, performed without analyzer, (a) along the *h* direction, (b) along the *l* direction.

We have confirmed the basic magnetic structure of UNi_4B and measured its field dependence up to 2.5 T. We showed that the earlier proposed strong one-dimensional excitations do not exist, and found several excitations in both zones studied. The nature and Q-dependence of these excitations is presently unclear. The data obtained without analyzer are a starting point for a systematic search for possible low-energy excitations, not clearly established in the runs with analyzer. Evidence has been found for a superstructure somewhat different from that observed in a different crystal. Its implications are not yet known. In order to understand this and the field dependence of the various Bragg reflections, a continuation of these studies in zero field and high fields up to 9 T is needed.

2.3.1.10 Magnetic Ordering in the Random-Anisotropy System $Dy(As_{0.35}V_{0.65})O_4$

D.R. Taylor *(Queen's University)*

Large concentrations (As/V >0.2) of As added to $DyVO_4$ suppress the tetragonal to orthorhombic transition that normally occurs near 14 K. The random substitutions, however, break the local tetragonal symmetry at the Dy sites and induce a uniaxial moment parallel to one or the other

basal plane axes. The system thus provides an ideal random-axis antiferromagnet with two identical competing anisotropy axes, but with no mixing of the magnetic species. A neutron scattering experiment was carried out on the E3 spectrometer at the NRU reactor using the H8 cryostat on a crystal with 35% arsenic concentration. The objective was to examine the (100) reciprocal lattice point for evidence of antiferromagnetic ordering. The monochromator was Ge (113), giving an incident neutron wavelength of 1.188 Å. Graphite filters in both the incident and scattered beams reduced higher-order scattering at (100) to unobservable levels. A peak was found to appear at approximately 1.9 K, consistent with antiferromagnetic ordering, well below the temperature (3.0 K) expected for ordering. Both a broad peak and a narrow, resolution-limited peak appear at this temperature, indicating that regions with both short- and long-range order were simultaneously present. Just below this temperature the broad peak (width 0.1 rlu) dominates the scattering intensity, but the narrow peak grows rapidly at lower temperatures while the broad peak changes rather little. Data taken at the (010) and (300) positions confirmed the general results. There was some indication of hysteresis in the magnetic ordering, but better thermometry is required to confirm this and to obtain results for critical exponents.

2.3.1.11 Random-Field Broadening of Diffraction Peaks in Orthorhombic $Dy(As_{0.15}V_{0.85})O_4$

D.R. Taylor, K.A. Reza and J.T. Graham *(Queen's University)* and W.J.L. Buyers *(AECL)*

High-resolution measurements of neutron diffraction peaks were carried out in $Dy(As_{0.15}V_{0.85})O_4$ to determine the changes in width and structure associated with the transition from a tetragonal to a twinned orthorhombic lattice. Previous experiments (J.T. Graham, D.R. Taylor, D.R. Noakes and W.J.L. Buyers, Phys. Rev. **B43** (1991), 3778) had found a significant increase in the transverse width for larger arsenic concentrations, which was associated with roughening of the {110} domain walls by the random strains due to the As/V size mismatch. The degree of roughness and its dependence on temperature, composition, and ordering field would allow basic models of random field phase transitions to be tested.

The spectrometer configuration chosen to provide high resolution with a small sample was a focussed "W" triple-axis configuration with monochromator and analyzer plane spacings matched to the (660) spacing of the sample. The rocking curve FWHM peak widths just above the transition temperature T_D=8.4 K were 0.048° (transverse) and 0.060° in transverse and longitudinal directions, respectively. The high resolution was obtained by use of a highly oriented germanium analyzer.

The temperature dependence of the transverse widths is shown in Fig. 2.3.1.13 for the $(\bar{6}60)$ peak at three temperatures.

Just below T_D a broad component develops under the main peak, which itself broadens significantly. At low temperatures, the intensity appears in two main peaks, indicating that the sample twinning is predominantly parallel to the $(\bar{1}10)$ direction. The sharper features that appear at low temperatures are attributed to areas that contain larger single domains. The overall *broadening by a factor of ~ 4 is to be compared with negligible broadening in pure* $DyVO_4$

(unpublished work), and has been analyzed using a random walk model of domain orientations (J.T. Graham et al., *loc. cit.*) to give a roughness parameter of 0.11 μm for a typical interface.

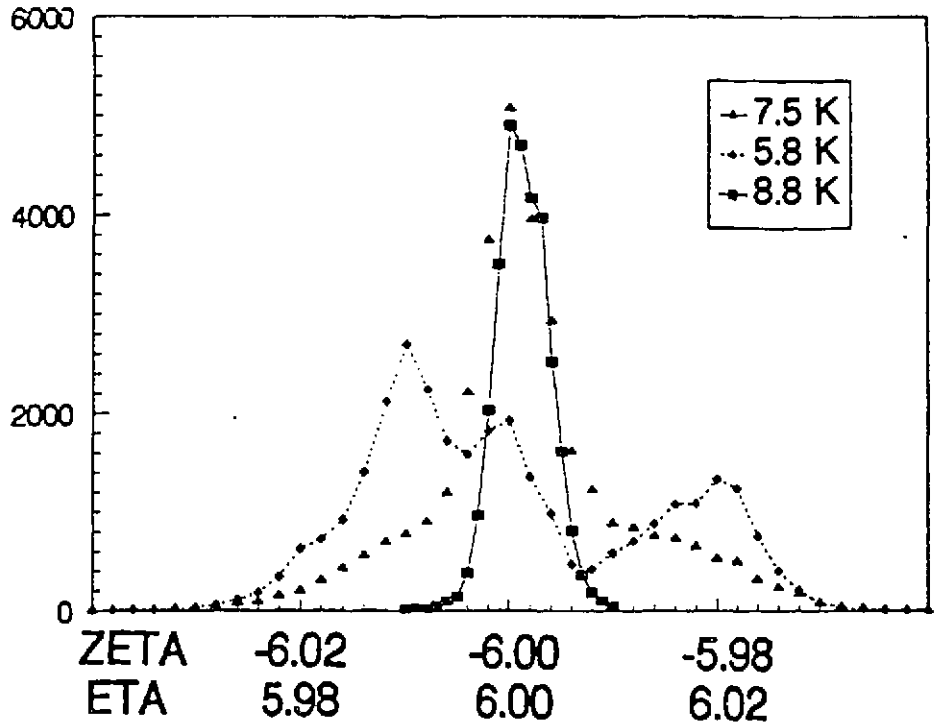

Fig. 2.3.1.13

Another set of experiments was to observe lineshapes such as those in the Fig. 2.3.1.13 while an ordering field forces the sample into a single domain. The observations imply that the interfaces become smoother as the field increases, and when domains re-form after removal of the field they adopt a different configuration with smoother walls.

The radial peak widths were also investigated. They showed a small but unambiguous broadening below T_D, but it is not clear whether this is a finite-size broadening or an indirect consequence of the transverse broadening.

We also examined the (100) magnetic peak that appears in the antiferromagnetic phase at lower temperatures. The objective was to determine whether the residual random strain fields depress the ordering of Dy spins. Our result for the ordering temperature was T_c=2.8 K, only slightly lower than predicted for a linear interpolation between the transition temperatures for pure $DyVO_4$ and $DyAsO_4$. This contrasts strongly with the effect of arsenic substitutions in $DyPO_4$, where magnetic ordering is completely suppressed for a few atomic percent As. The significant difference appears to be that the anisotropy directions in $DyPO_4$ are quite different than in $DyAsO_4$ or $DyVO_4$.

The results demonstrate that this system is an excellent one in which to study domain-wall roughening by random static fields.

2.3.1.12 Nature of Magnetic Transition in $NaTiO_2$

Z. Tun *(AECL)*, S.J. Clarke and M.J. Rosseinsky *(University of Oxford)* and A. Harrison *(University of Edinburgh)*

Due to its layered rock-salt structure with a triangular arrangement of Ti^{3+} ions, $NaTiO_2$ had long been viewed as a suitable candidate for observing a non-classical ground state in the two-dimensional triangular lattice (P.W. Anderson, Mat. Res. Bull. **8** (1973), 153). It has approximate lattice parameters a = 3.0 Å and c = 16.2 Å in the space group R3m, where the lattice parameter a is equal to the separation of Ti^{3+} ions. When the material is prepared with the rigorous exclusion of oxygen and water and under conditions in which the Na/Ti ratio is not allowed to drop below 1.0, the black powder samples have very reproducible lattice parameters. Material which is deficient in Na has a shorter a and a longer c. There is a strong correlation between the composition, the lattice parameters and the behaviour of the magnetic susceptibility. The susceptibility of material which is not Na-deficient shows a large and broad anomaly at 250 K, as shown in Fig. 2.3.1.14. The anomaly has been interpreted as evidence for short-range magnetic order of local moments on the triangular lattice (K. Takeda, K. Miyake, K. Takeda and K. Hirakawa, J. Phys. Soc. Japan **61** (1992), 2156), although the anomaly has an unusual shape and the associated entropy change exceeds that expected for complete ordering of S = 1/2 moments on the triangular lattice. We entertain the possibility that the magnetic transition has some structural origin by analogy with other oxide materials in this region of the periodic table (N.F. Mott, Metal Insulator Transitions (1990), Taylor and Francis, London).

A structural analysis of $NaTiO_2$ was carried out with the C2 DUALSPEC powder diffractometer at eleven temperatures between 100 K and room temperature. The powder sample has been previously characterized and is known to show a large magnetic anomaly. Data were collected in the angular range 14° - 94° with a step size of 0.05° in 2θ. The peaks were resolution limited with a FWHM of about 0.2°. Rietveld refinement of the data was carried out using GSAS assuming that the space group was R3m at all temperatures. The fits (Fig. 2.3.1.15) were of good quality with typical X^2 ~ 2.0. While there was no direct observation of a lowering of the symmetry, refinement using the alternative space group C2/m gave an equally good fit at 100 K, but not at room temperature. We have since confirmed that the material is indeed monoclinic at 100 K from data taken on the HRPD at ISIS, UK. The observed monoclinic distortion is extremely small.

On the basis of our refinements of the C2 data with space group R3m, we established that the compressed trigonal antiprismatic coordination of the Ti ion becomes more compressed on heating through the magnetic transition. Fig. 2.3.1.16 shows that the Ti - Ti separation increases on warming and the interlayer separation decreases to compensate. The unit cell volume follows the Ti - Ti separation, indicating that the change in separation drives the transition. This behaviour suggests that the magnetic transition is of the metal to insulator type.

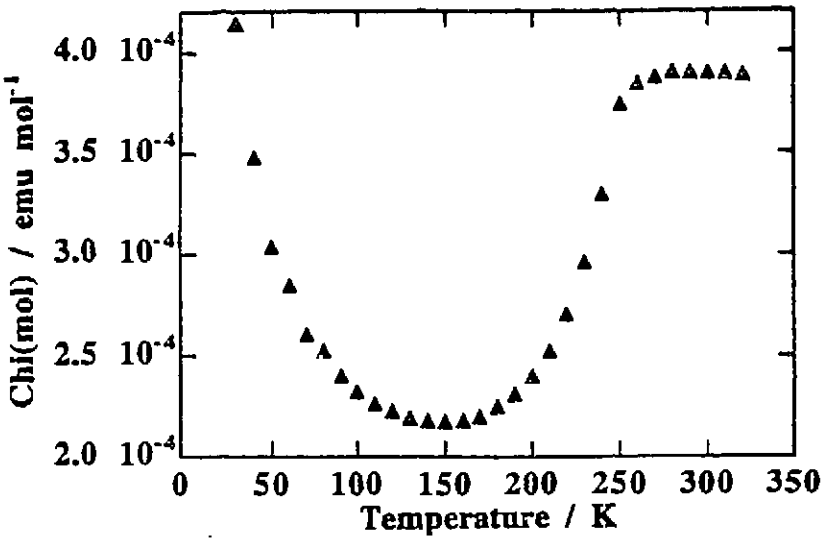

Fig. 2.3.1.14

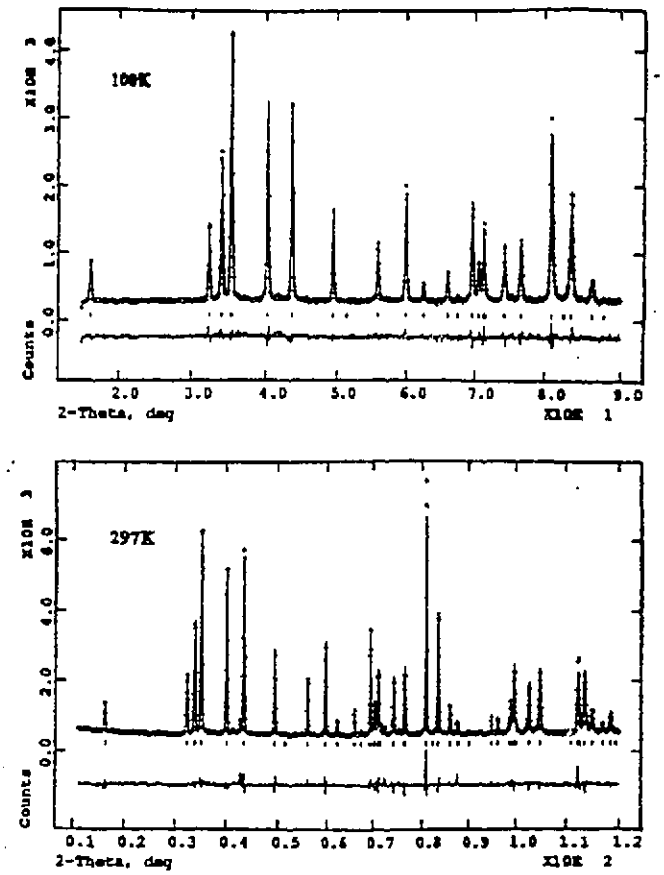

Fig. 2.3.1.15

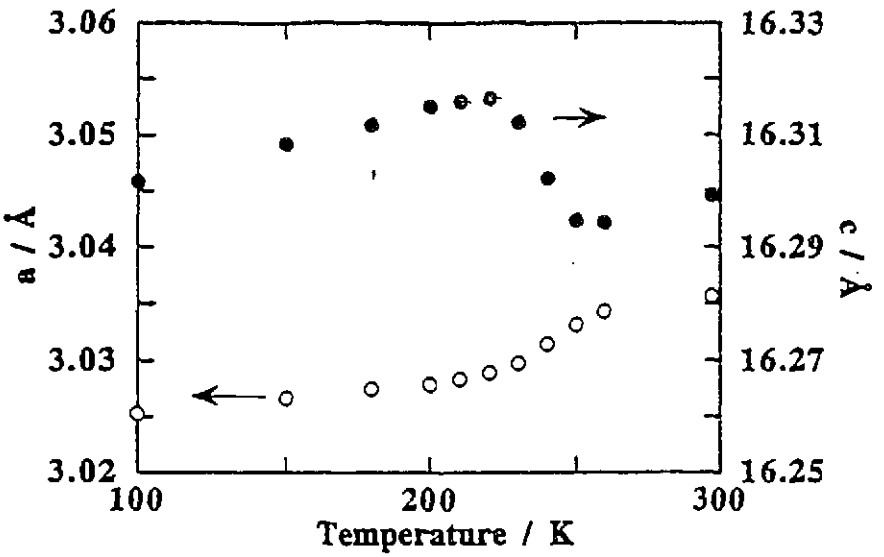

Fig. 2.3.1.16

2.3.1.13 Critical Neutron Scattering Study of $CsCoBr_3$

M. Mao and B.D. Gaulin *(McMaster University)* and R.B. Rogge *(AECL)*

$CsCoBr_3$ is well described as an Ising-like antiferromagnet (AF) on a stacked triangular lattice. The AF interactions within the triangular basal plane are geometrically frustrated; that is, the AF exchange cannot be simultaneously satisfied between the magnetic moments (spins) at the corners of the triangular plaquettes. Critical fluctuations in the vicinity of the magnetic phase transition at $T_N = (28.23 \pm 0.04)$ K have been studied with high-resolution, energy-integrated neutron scattering techniques on a single crystal sample in zero field. The measurements were performed on the C5 spectrometer of DUALSPEC. Temperature stability of ±2 mK was realized over the required 26 to 32 K temperature range.

The build-up of spin-spin correlations upon approaching the phase transition can be seen in the observed scattering intensities at ordering wave vectors (-⅓, -⅓, 1) and (-⅔, -⅔, 1). After resolution convolution, the observed scattering is found to be well described by a single Lorentzian line shape, as shown in Fig. 2.3.1.17. Previous measurements required a second Lorentzian-squared component, and these higher resolution measurements were intended to address this issue.

The assignment of a system to a so-called Universality class is central to the study of continuous phase transitions. Each class can be identified in part by a set of critical exponents. Analysis of this data gives critical exponents, $\nu = (0.54 \pm 0.05)$, $\gamma = (1.05 \pm 0.08)$, and $\beta = (0.28 \pm 0.02)$. While these results are not fully understood, the γ and ν parameters are in good agreement with those obtained from the previous data. The measured exponents are close to the predictions of tricritical mean field theory, but symmetry arguments predict that $CsCoBr_3$ should be a member

of the 3D XY universality class. The question of which universality class $CsCoBr_3$ should belong to remains unanswered.

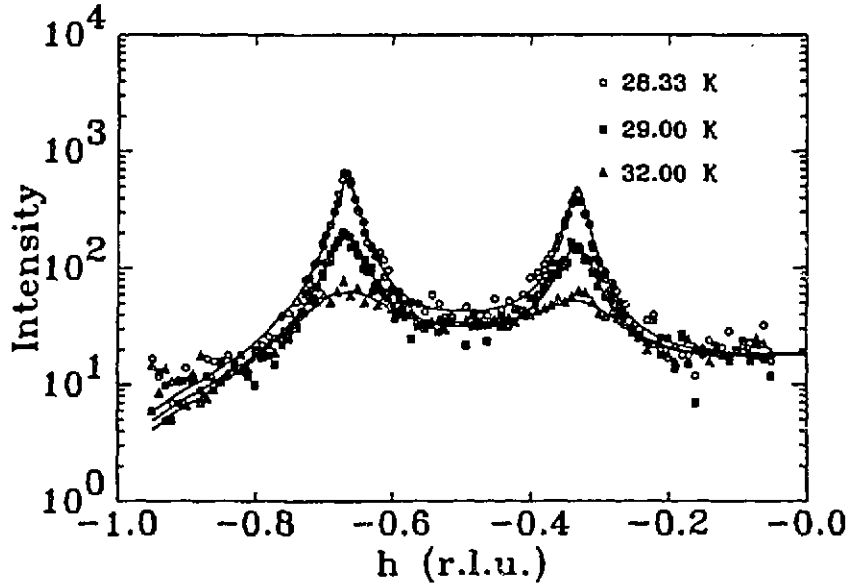

Fig. 2.3.1.17 The observed scattering intensities at (-⅓, -⅓, 1) and (-⅔, -⅔, 1) for different temperatures. The solid lines are the fits.

2.3.1.14 **Searching Evidence for Multi-Magnon Scattering in $CsNiCl_3$**

Z. Tun, T.C. Hsu and W.J.L. Buyers *(AECL)*

Ohyama and Shiba (J. Phys. Soc. Japan **62** (1993), 3277) have proposed that multimagnon processes, which arise from higher-order terms in a 1/S expansion, can lead to peak-like features in the excitation spectrum of quasi-one-dimensional materials. The theory applied to the Haldane gap material $CsNiCl_3$ suggests that some of the peaks that have been identified as single-magnon modes by Z. Tun, W.J.L. Buyers, R.L. Armstrong, K. Hirakawa and B. Briat (Phys. Rev. B **42** (1990), 4677) and K. Kakurai, M. Steiner, R. Pynn and J.K. Kjems (J. Phys. Condens. Matter **3** (1991), 715) are actually due to two-magnon excitations. As for the purely one-magnon modes, the theory predicts them in general to lie at frequencies lower than the peaks due to two-magnon excitations. This experiment was carried out to look for inelastic scattering from these low-frequency modes.

The spectrum calculated from the Ohyama and Shiba theory at **Q** = (0.05, 0.05, 1), one of the wave vectors experimentally investigated, is shown in Fig. 2.3.1.18. The peak labelled "A" is a known excitation, which is now purported to be a result of two-magnon excitations. We particularly searched for the lower-frequency one-magnon mode, labelled "B" in Fig. 2.3.1.18.

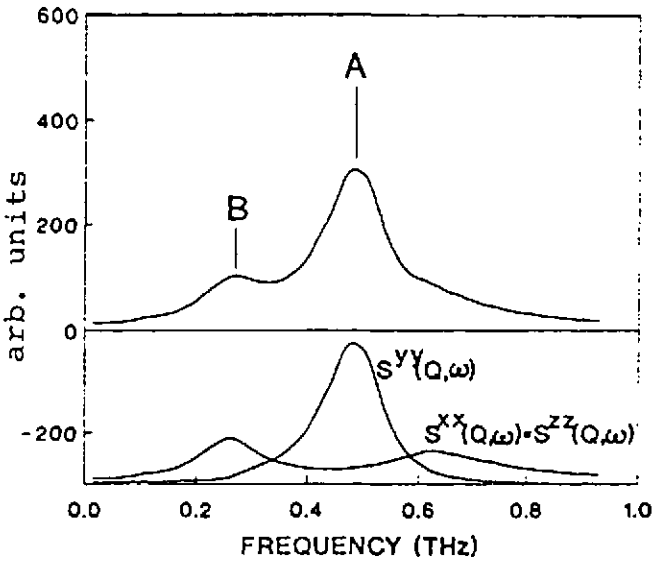

Fig. 2.3.1.18

The experimentally measured $S(\mathbf{Q},\omega)$ is shown in Fig. 2.3.1.19. The predicted low-frequency mode we sought is not observed, at least not with the expected intensity. Constant-**Q** scans were made also at a number of symmetry equivalent wave vectors. The predicted mode was not observed. We therefore conclude that Ohyama and Shiba theory is not applicable to $CsNiCl_3$.

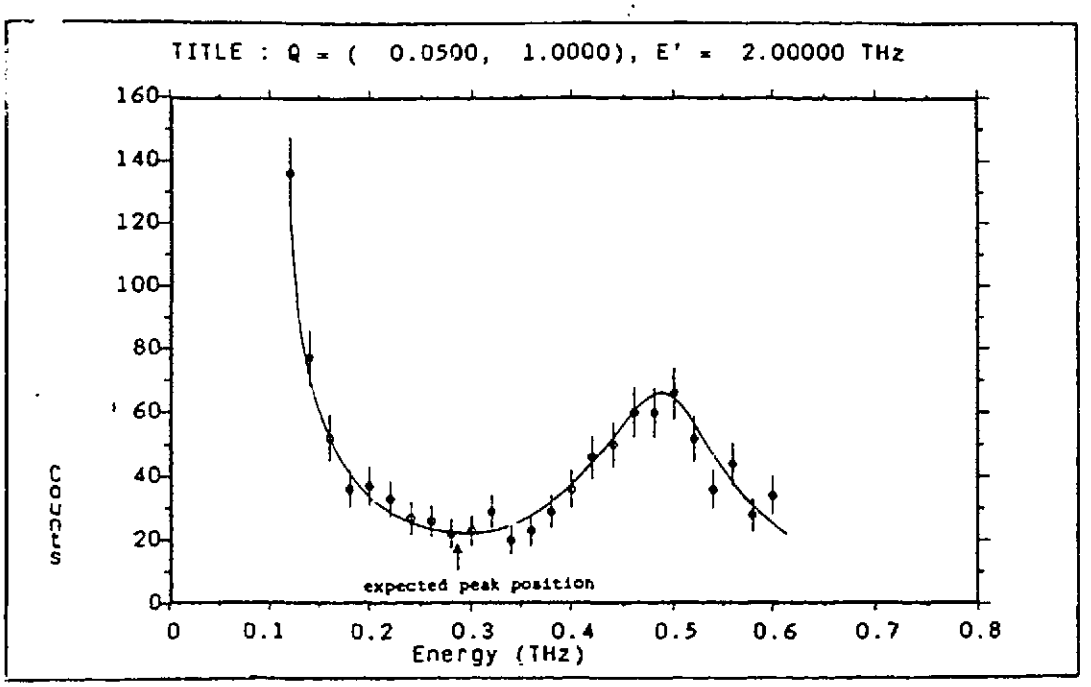

Fig. 2.3.1.19

2.3.1.15 Spin-Waves in $FeGe_2$

T.M. Holden *(AECL)*, A.Z. Menshikov *(Institute for Metal Physics, Ekaterinburg)* and E. Fawcett *(University of Toronto)*

The crystal structure of $FeGe_2$ is tetragonal, with four iron and eight germanium atoms in the unit cell. The magnetic structure below 275 K corresponds to ferromagnetically aligned chains along the c-axis with antiferromagnetic coupling between chains. The separation of the iron atoms in the c-axis chains is 2.5 Å, similar to the interatomic separation in metallic iron, 2.6 Å, and considerably smaller than the distance between adjacent chains, 4.2 Å. The neutron inelastic scattering experiments were carried out with the N5 triple-axis spectrometer, with (113) and (111) planes of Si crystals used as monochromator and analyzer, respectively. The crystal was aligned to measure excitations propagating in the a- and c-directions. The magnon and phonon dispersion curves at low temperatures are shown in Fig. 2.3.1.20. The magnon dispersion relation, indicated by full symbols, is anisotropic: along the c-axis the frequency rises linearly with wavevector, reaching 11 THz by ⅓ of the Brillouin zone boundary, but along the a-axis the frequency rises 30% less rapidly, to a maximum value of 6 THz. There is no evidence for a spin-wave anisotropy gap. The open symbols correspond to zone edge phonons of no direct relevance to the magnetism. There is little change in the magnetic response between 4.2 K and 130 K.

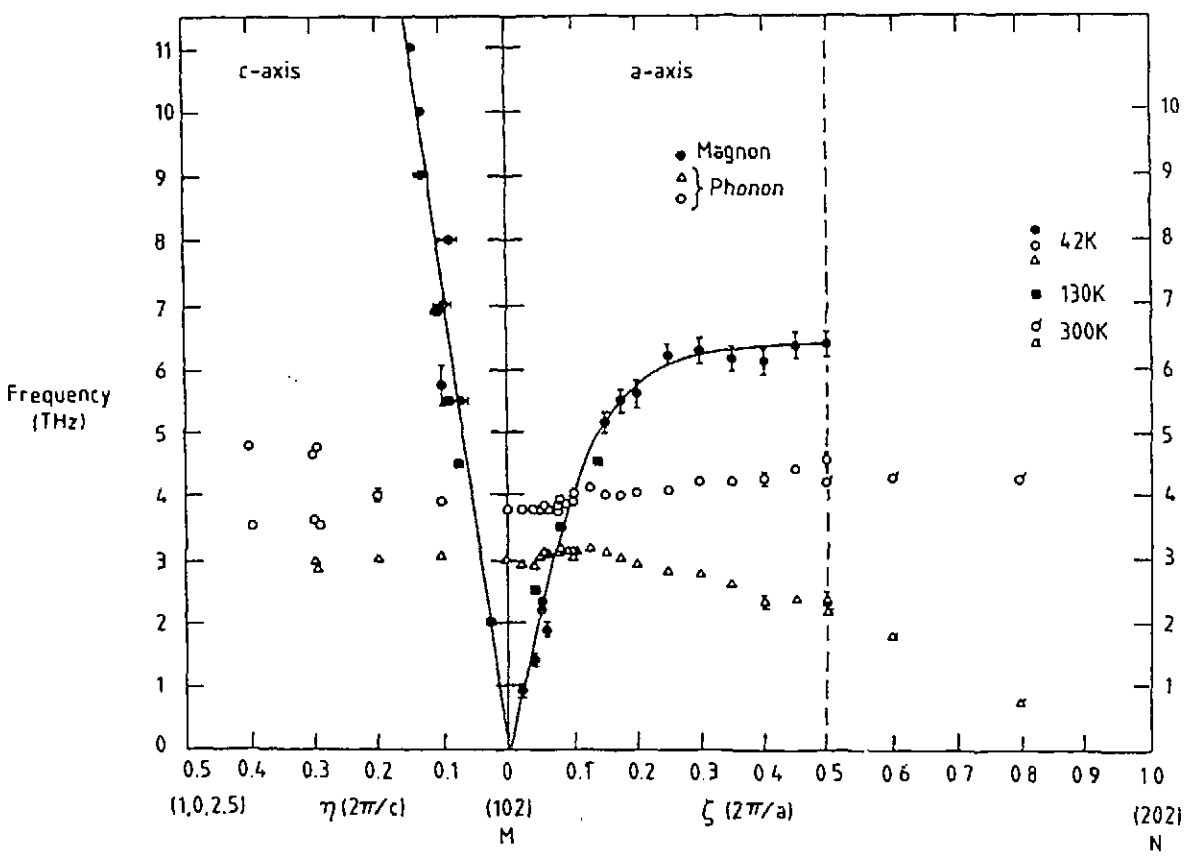

Fig. 2.3.1.20

Above this temperature there are subtle differences between the c- and a-axis behaviour. For example, a constant-ν scan at 3.5 THz through the (102) reciprocal lattice point along the a-axis shows two sharp peaks corresponding to the spin wave excitations at 130 K, but only a single peak at 275 K. A constant-ν scan at 3.5 THz along the c-axis gives two quite well-defined peaks at 275 K. These differences, and the anisotropy of the spin-wave dispersion relation, are consistent with a picture of $FeGe_2$ in which there is a strong ferromagnetic exchange coupling within chains of spins parallel to the c-axis and weaker antiferromagnetic coupling between the chains.

2.3.1.16 Neutron Scattering Study of the Structure of Metallic Glass $Ni_{0.5}Zr_{0.5}$

M. Mao and B.D. Gaulin *(McMaster University)*, W.J.L. Buyers *(AECL)*, Z. Altounian and W.B. Muir *(McGill University)*

The Faber-Ziman partial structure factors of metallic glasses $Ni_{0.33}Zr_{0.67}$ and $Ni_{0.67}Zr_{0.33}$ have been accurately determined recently by X-ray diffraction using the isomorphous substitution technique on the Ni-Zr-Hf glassy system. The partial structure factors generally reproduced the neutron scattering data (Y. Xu, W.B. Muir, Z. Altounian, W.J.L. Buyers and R. Donaberger, Phys. Rev. **B1**, to be published) for these two compositions. The X-ray partial structure factors were, however, found to be strongly composition dependent, in contrast to the model prediction, and failed to give the low-angle precursor peak seen only in the neutron data. To give a definitive answer to whether this composition dependence of the partial structure factor is *linear*, one must perform a detailed structural study of the alloy with composition $Ni_{0.5}Zr_{0.5}$.

A self-supporting ribbon bundle of $Ni_{0.5}Zr_{0.5}$ about 7 mm in diameter and 70 mm in length, weighing about 10 grams, was mounted inside the H8 cryostat, which was continuously evacuated to reduce the background air scattering. The neutron scattering measurement was performed at a wavelength of 1.180 Å on the C2 DUALSPEC powder diffractometer using Si (531) as the monochromator. The entire diffraction pattern from the sample was recorded for 18 hours over an angular range of ϕ=5°-123° using two positions of the detector with a 42° overlap in the two data sets. A background scan over 7 hours was then conducted under the same experimental conditions.

The raw data are presented in Fig. 2.3.1.21, showing very good counting statistics, although there is a slight mismatch between the two data sets collected over the two different detection positions. A great improvement in the data quality has been obtained by performing the measurement in vacuum. The signal to background ratio is ~ 20 at 5° and 120 at the peak position of the scattering curve for the present experiment, as compared to those of the measurements (Yan Xu et al., *loc. cit.*) performed in air on $Ni_{0.3}Zr_{0.7}$ and $Ni_{0.7}Zr_{0.3}$, which are ~ 2 and 9, respectively. This indicates that what has been measured is essentially the total structure factor S(Q). The low angle peak at ~ 19.6°, which is due to the three-body correlation and was poorly resolved in the previous measurements, is now clearly exhibited as a peak. Further data reduction is under way, which will be of great assistance to the determination of the partial structure factors of metallic glass $Ni_{0.5}Zr_{0.5}$ and therefore the amorphous structure of metallic glasses NiZr when combined with the results from X-ray diffraction.

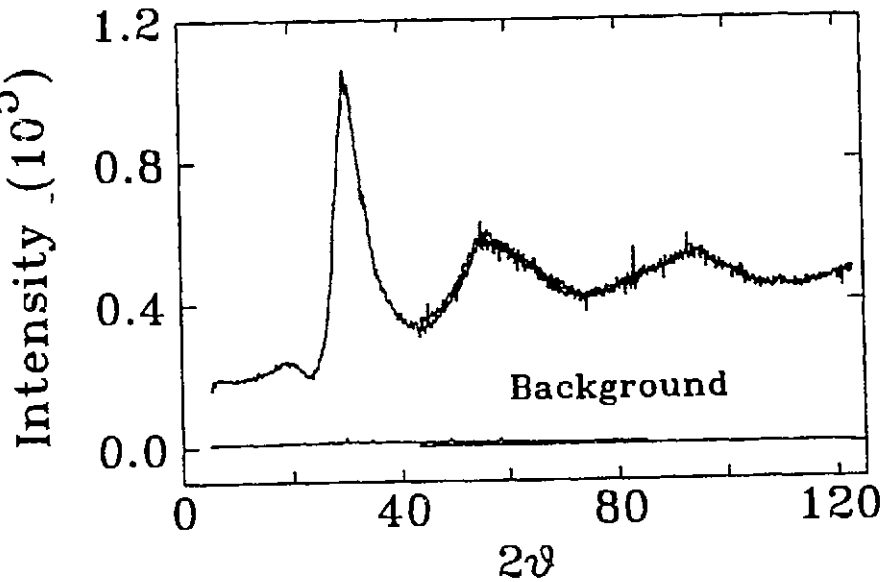

Fig. 2.3.1.21 Neutron diffraction pattern of $Ni_{0.5}Zr_{0.5}$.

2.3.1.17 Neutron Diffraction Studies on Liquid, Glassy and Crystalline $Ca_{0.4}K_{0.6}(NO_3)_{1.4}$

E.C. Svensson *(AECL)*, E. Kartini and M.F. Collins *(McMaster University)* and F. Mezei *(Hahn Meitner Institute)*

The C2 DUALSPEC diffractometer has been used to determine the temperature dependence of the static structure factor S(Q) of $Ca_{0.4}K_{0.6}(NO_3)_{1.4}$ in its liquid and glassy states and the time dependence of the transformation to crystalline states on warming. On cooling $Ca_{0.4}K_{0.6}(NO_3)_{1.4}$ from the liquid state, a glass is formed with a glass transition temperature T_g = 335 K. On heating, crystallization takes place at 370 ± 5 K and, as shown by differential scanning calorimetry (DSC) measurements on samples from the same batch, there are two melting transition temperatures, 425 and 444 K.

The diffraction measurements, carried out using neutrons of 1.507 Å wavelength from a Si(531) monochromator covered a range of wave vectors, Q, from 0.2 to 5.5 $Å^{-1}$. The sample, 0.5 cm in diameter and 5 cm long, was contained in a thin-walled vanadium can. Measurements were carried out over the temperature range 300 to 573 K. Fig. 2.3.1.22 shows our results for the region of the main peak of S(Q) for temperatures of 300, 370, 483 and 573 K, when the sample is a glass, a supercooled liquid, a liquid and a liquid, respectively. The counting time for each spectrum was about 2 hours. The spectra all show the features typical of an amorphous material. There are, however, systematic changes with temperature, which are most marked for the region near the main peak of S(Q), at Q ~ 1.8 $Å^{-1}$. The height of this peak increases, its width decreases, and its mean position moves to larger Q as the sample is cooled from 573 K to room temperature. Our detailed analysis indicates that all three quantities exhibit a linear dependence on temperature. There is no evidence of any anomaly at T_g, or elsewhere.

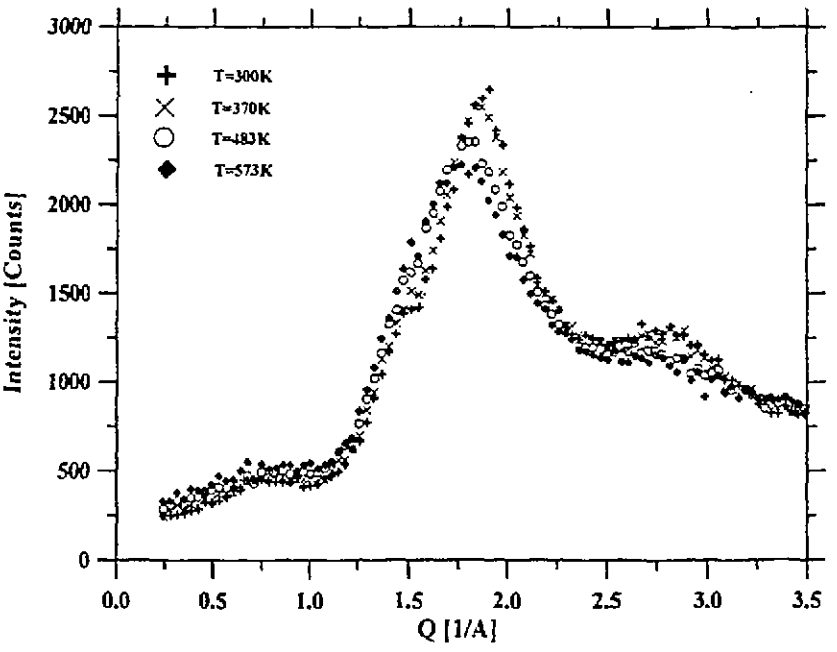

Fig. 2.3.1.22 The static structure factor, S(Q), for $Ca_{0.4}K_{0.6}(NO_3)_{1.4}$ in its liquid (573 and 483 K), supercooled liquid (370 K) and glassy (300 K) states.

Our study of the time dependence of the transformation to crystalline states on warming gives very interesting results. The spectra observed in 0.5 hour runs at 380 K, starting 0.5, 3 and 18 hours after this temperature was first reached (on warming slowly), are shown in Fig. 2.3.1.23. The time dependence of the intensities of the emerging powder lines (Fig. 2.3.1.24) was analyzed in terms of the Johnson-Mehl-Avrami equation (W.A. Johnson and K.F. Mehl, Trans. Am. Inst. Mining Metall. Eng. **135** (1939), 416 and M. Avrami, J. Chem. Phys. 7 (1939), 1103 and **8** (1940), 212),

$$I(t) = 1 - \exp\,[-((t-t_0)/\tau)^n],$$

where τ is the time constant for the process and n is the Avrami exponent which is indicative of the nature of the growth process. It shows that the lines fall into two distinct sets which have markedly different characteristic growth patterns. Set A ($\tau = 5.2 \pm 0.7$ hrs, $n = 0.78 \pm 0.24$), with example lines at scattering angles of 21.10° and 43.01°, grows rapidly for the first 5 hours and then grows slowly. Set B ($\tau = 9.5 \pm 1.0$ hrs, $n = 1.8 \pm 0.4$), with example lines at 14.72° and 29.71°, grows much more slowly at first, but continues to grow approximately linearly for the first 12 hours. These sets correspond to two different crystal structures, neither of which corresponds to the structures of either KNO_3 or $Ca(NO_3)_2$, the parent materials which were used to produce the sample. These results indicate that the crystallization process involves two previously unknown compounds of potassium and calcium nitrate, which undoubtedly explains the two melting points observed in the DSC measurements. The very different Avrami exponents

for sets A and B indicate that the growth process (which is controlled by the nucleation rate, the dimensionality of the crystallites that are formed, and diffusion) is very different for the two structures that are evolving. For diffusion-controlled three-dimensional growth with zero nucleation rate after time zero, the Avrami exponent is predicted to be 1.5. This is consistent with what we observe for set B. Our results (Fig. 2.3.1.23) also show that, after 18 hours at 380 K, about 15% of the sample remains in a non-crystalline form. The decrease of the non-crystalline component with time is reasonably well described by a simple exponential function, $I(t) = \exp(-t/\tau)$, with $\tau = 10.9$ h.

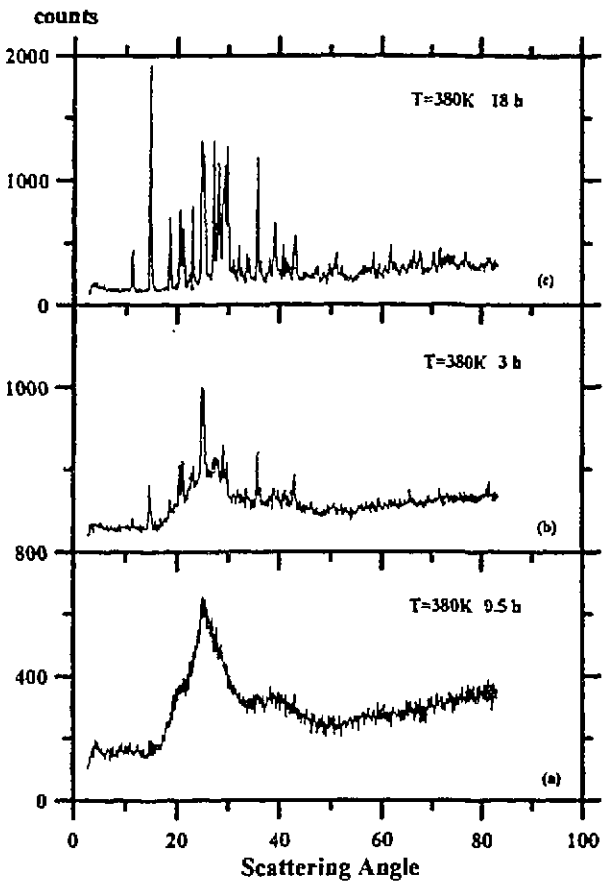

Fig. 2.3.1.23 Diffraction patterns for $Ca_{0.4}K_{0.6}(NO_3)_{1.4}$ obtained in 0.5 hours counting periods beginning 0.5 h (a), 3 h (b) and 18 h (c) after T = 380 K was reached on warming.

2.3.1.18 Inelastic Neutron Scattering by $Ca_{0.4}K_{0.6}(NO_3)_{1.4}$

E.C. Svensson *(AECL)*, E. Kartini and M.F. Collins *(McMaster University)* and F. Mezei *(Hahn Meitner Institute)*

In addition to the neutron diffraction measurements on $Ca_{0.4}K_{0.6}(NO_3)_{1.4}$ discussed in the preceding report (2.3.1.76), we have carried out neutron inelastic scattering measurements using the C5 DUALSPEC triple-axis spectrometer. The primary aims of this work are to discover signatures

of the liquid-glass transition and to obtain results to test critically the predictions of mode-coupling theories.

The sample for the inelastic measurements was a large, rectangular slab of 0.5 cm thickness contained in an aluminum holder with thin (0.5 mm) incident and exit windows. It was masked to an area 5 cm wide by 7 cm high on the incident-beam side, and the measurements were carried out with the sample in symmetric transmission using a Si(113) monochromator and a Ge(113) analyzer. The scattered neutron energy was fixed at 3.52 THz. Sapphire and pyrolytic graphite filters were placed in the incident and scattered beams, respectively, to suppress higher-order neutrons. The resolution at the elastic position was 0.105 THz (FWHM). Measurements were carried out at temperatures between 300 and 573 K, with the sample in either a normal liquid, supercooled liquid, or glassy state. As noted in the preceding report, the glass transition temperature, T_g, is 335 K. Four different types of scans were carried out:

1. Elastic scattering, $S(Q, \omega = 0)$, for wave vectors Q from 0.3 to 4 $Å^{-1}$.

2. Quasielastic scattering (energy range -0.16 to +0.16 THz) for Q values of 0.8, 1.1, 1.5, 1.9 and 2.5 $Å^{-1}$.

3. Inelastic scattering over the energy range 0.1 to 1.8 THz for these same (constant) Q values.

4. Constant-energy scans at energies of 0.4, 0.8 and 1.6 THz over the Q range from 0.6 to 3.0 $Å^{-1}$.

Measurements were also carried out on an identical empty sample holder, and beam profiles were determined (by measuring the scattering from a thin polythene rod as it was translated across the incident beam at the sample position) for six values of the monochromator scattering angle, $2\theta_m$, covering the range employed for the measurements, in order to correct for the effect of rotating the large flat sample in an inhomogeneous flux distribution.

Extensive analysis of all the results is now in progress. We show results for the temperature dependence of $S(Q, \omega = 0)$ in Figs. 2.3.1.24 and 2.3.1.25. Fig. 2.3.1.24 shows the full $S(Q, \omega = 0)$ for five temperatures spanning the complete range of our measurements. Comparison with the results for the static structure factor, S(Q), the integral over all ω of $S(Q, \omega)$, shown in Fig. 2.3.1.22 of the preceding report reveals that $S(Q, \omega = 0)$ exhibits a much greater change with temperature than does S(Q). This is because the total scattering becomes increasingly more inelastic as the temperature is raised. It is also obvious, from this comparison, that the elastic contribution decreases with increasing Q at a given temperature. The temperature dependence of the height and position of the main peak in $S(Q , \omega = 0)$ is shown in Fig. 2.3.1.25. There is clearly a deviation from the linear dependence on temperature observed at high temperature when one goes below T_g = 335 K. Hence, in contrast to the results for S(Q), the results for $S(Q, \omega = 0)$ show a clear signature of the liquid-to-glass transition.

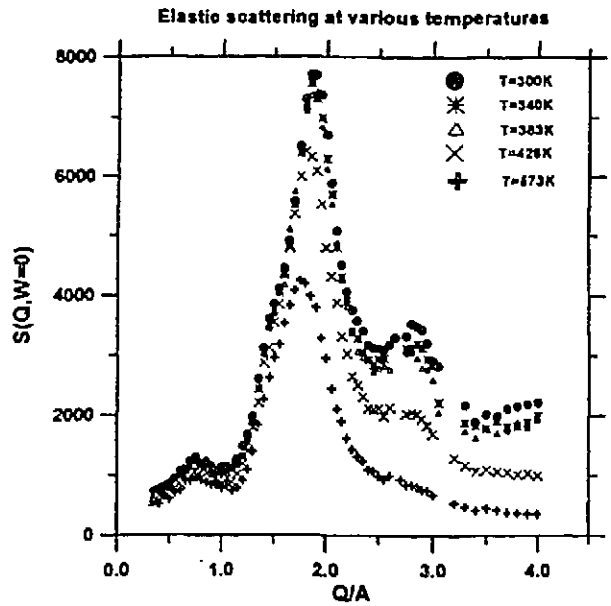

Fig. 2.3.1.24 $S(Q, \omega = 0)$ for $Ca_{0.4}K_{0.6}(NO_3)_{1.4}$ at 5 temperatures. The "gaps" at Q = 2.7 and 3.1 $Å^{-1}$ are a consequence of powder lines from the aluminum sample holder at these Q values.

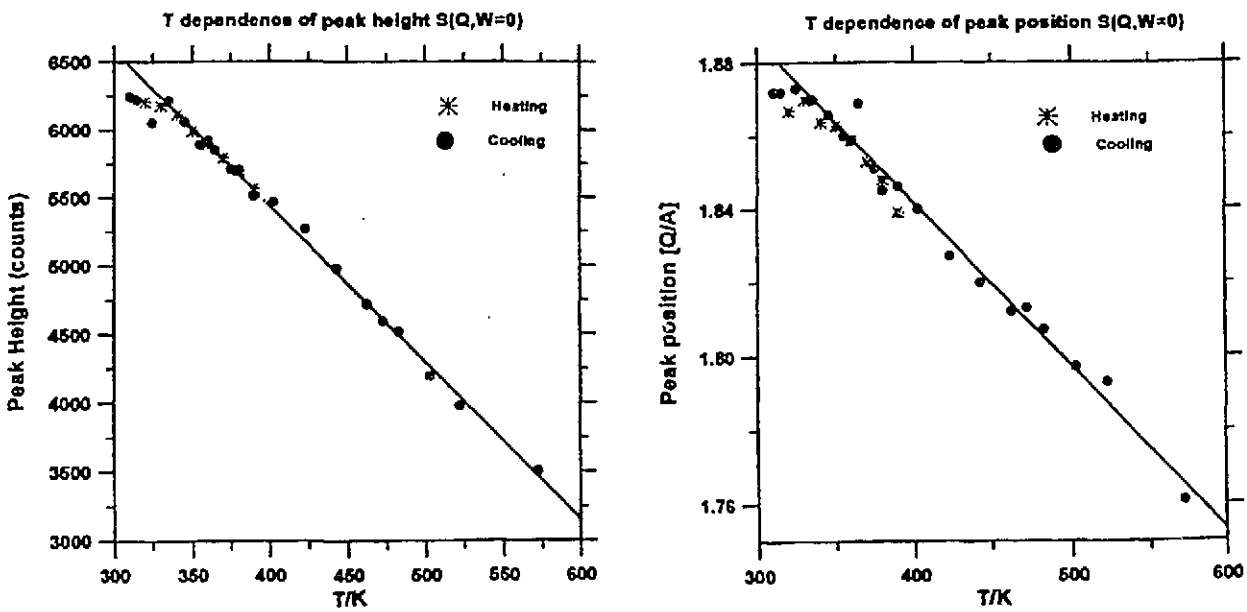

Fig. 2.3.1.25 The temperature dependence of the height (left panel) and the position (right panel) of the main peak in $S(Q, \omega = 0)$ for $Ca_{0.4}K_{0.6}(NO_3)_{1.4}$ (see Fig. 2.3.1.24).

2.3.1.19 Powder Diffraction in $CuGeO_3$

D.R. Taylor and M. Sayer *(Queen's University)* and I.P. Swainson *(AECL)*

Great interest in copper germanate $CuGeO_3$ was stimulated by the work of M. Hase, I. Terasaki and K. Uchinokura (Phys. Rev. Lett. **70** (1993), 3651) that identified a Spin-Peierls (SP) transition at 14 K. The only SP transitions previously identified were in complex organic compounds that were not suitable for detailed investigations of the structure and dynamics. A powder diffraction experiment was carried out at the C2 DUALSPEC powder diffractometer at NRU, to look for diffraction evidence for SP dimerization and to identify the low-temperature structure. The sample was prepared in powder form by M. Sayer at Queen's University. The Si (531) monochromator gave a wavelength of 1.548 Å. Half-wavelength contamination was reduced with a graphite filter in the incident beam. Spectra were recorded for scattering angles between 20 and 120 degrees with steps of 0.025 degrees, at temperatures of 20 K and 3 K. The data for the two temperatures (above and below the expected transition temperature) were separately analyzed by Rietveld refinement, and were subtracted to look for the appearance of new peaks. No detectable change in the structure was found, and no new features were observed at expected scattering angles. On the other hand, no magnetic peaks appeared, consistent with a SP transition. The Rietveld refinement gave satisfactory fits to the orthorhombic Pmma structure. Subsequently, neutron and X-ray data from other groups from single crystals verified the dimerization transition. Neutron powder diffraction performed by other groups also failed to observe this effect.

2.3.1.20 Powder Diffraction of Praseodymium Deuteroxide $Pr(OD)_3$

D.R. Taylor *(Queen's University)* and S. Mroczkowski *(Yale University)*

$Pr(OD)_3$ is a member of an isostructural series that includes some hexagonal rare-earth chlorides, bromides, etc. The praseodymium compounds undergo structural, not magnetic, ordering at low temperatures, and the phase transition has been identified as a Spin-Peierls (SP) transition (Morra, Armstrong, and Taylor, Phys. Rev. Lett. **51** (1983), 809). However, no diffraction evidence has been obtained. The hydroxide members of this series have transition temperatures around 1.2 K, which, although very low, are higher than the halide compounds. An experiment was carried out to look for any change in the diffraction spectrum in this temperature range that might provide definite evidence. The experiment was carried out on the E3 spectrometer with the H5 cryostat and the Edwards 275 pump/Roots booster facility, to reach liquid helium pressures below 1 torr and temperatures below 1 K. The neutron wavelength was 2.376 Å and a graphite filter was inserted in the incident beam. The deuterated powder sample was provided by S. Mroczkowski, of Yale University. An 11-wire multidetector was used to record diffraction spectra at 4.2 K and 1.0 K. No detectable change in the spectrum was observed. This was not surprising, since structural changes occurring at such a low temperature would be very small, and the limited sample size and counting statistics would make detection very difficult. However, magnetic ordering was not observed and this is significant evidence in favour of a SP transition. The observed spectra will be analyzed by Rietveld refinement.

2.3.1.21 Phonon Density of States in Vanadium

V.F. Sears, E.C. Svensson and B.M. Powell *(AECL)*

Over the past five years, a number of neutron inelastic scattering experiments have been performed at NRU to determine the phonon density of states for various hydrogenous materials. To obtain a benchmark for this work, and to further test the method used for making multiphonon corrections, we have recently carried out similar experiments on vanadium. Vanadium is the prototype material for these kinds of measurements because (1) it is an almost totally incoherent scatterer and (2) the atoms occupy the sites of a cubic Bravais lattice (the bcc structure) so that, to the extent that multiphonon scattering is negligible, the observed inelastic scattering is directly proportional to the phonon density of states $g(\nu)$. In all other materials, the effective density of states obtained from such experiments is weighted by the phonon polarization vectors.

The vanadium sample was a slab 4.6 mm thick, masked to a width of 5 cm on the incident-beam side, and the experiments were performed at room temperature (293 K) in symmetric transmission geometry, using the N5 triple-axis spectrometer with a Si (331) monochromator and a Ge (113) analyzer. Scans were taken at a constant wave-vector transfer Q = 6.5 $Å^{-1}$ using a constant scattered-neutron energy of 8.0 THz. The energy transfer ν was varied from −1.9 to 10.0 THz in steps of 0.1 THz, and the energy resolution (FWHM) was 0.3 THz at the elastic position (ν=0). Under these conditions, it was necessary to run for approximately two weeks to obtain reasonable intensity, 300 to 600 counts in the inelastic region. The corresponding background, as determined from measurements with the sample removed, was about 60 counts.

Fig. 2.3.1.27 shows the phonon density of states obtained from a preliminary analysis of the data. The transverse peak at 4.9 THz and the longitudinal peak at 6.8 THz are much more clearly resolved than in any previous measurements of this kind on vanadium. Our results are compared in Fig. 2.3.1.26 with the results from the first experimental paper on this subject by A.T. Stewart and B.N. Brockhouse (Rev. Mod. Phys. **30** (1958), 250). The comparison with these early results is especially relevant at the present time, because this early work was part of the pioneering work for which Professor Brockhouse was recently awarded the Nobel Prize in physics. Both sets of results were obtained using the same neutron source, the NRU reactor. The markedly higher quality of our present results is a reflection of the improvements in neutron spectrometry over the past four decades, especially the development of much better monochromator and analyzer crystals, which have allowed major improvements in resolution while still maintaining reasonable intensity. The monochromator and analyzer crystals used for our measurements were produced at CRL by squeezing slabs of initially perfect (negligibly small mosaic spread) Si and Ge single crystals at high temperature to produce an optimal combination of mosaic spread and reflectivity.

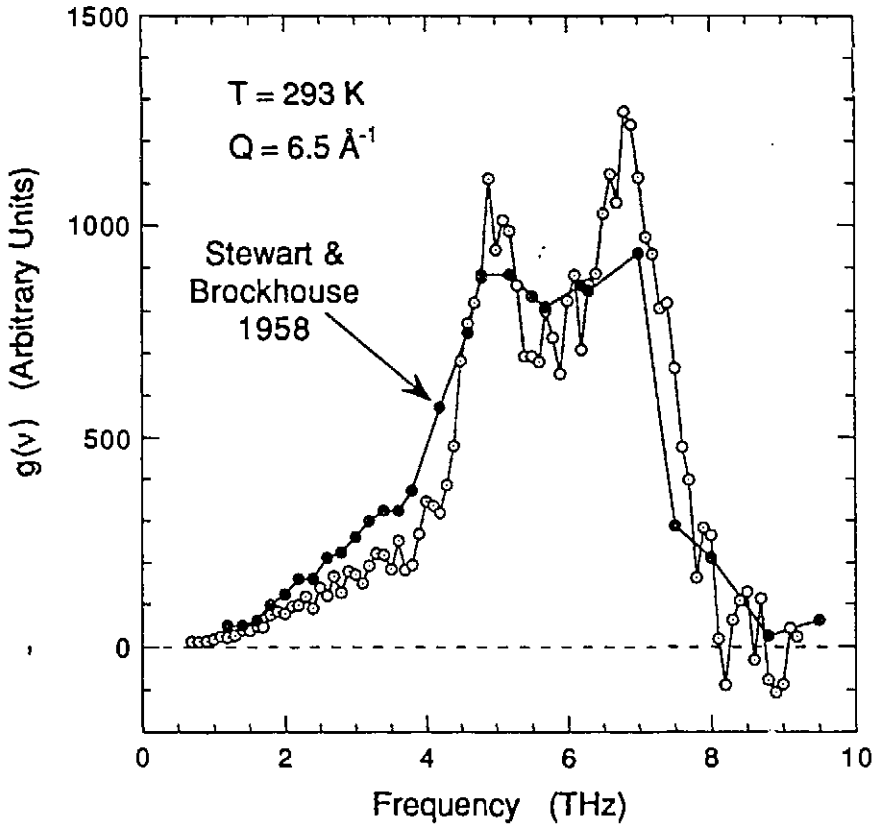

Fig. 2.3.1.26 Comparison of the $g(\nu)$ for vanadium from the present work (open circles) with that obtained in 1958 by Stewart and Brockhouse (solid circles).

2.3.1.22 A Program for Analyzing Neutron Reflectivity Measurements

Z. Tun and M. Vaillancourt *(AECL)*

As a tool for the analysis of neutron reflectivity measurements, a computer program developed at the National Institute for Science and Technology (NIST), by J.F. Ankner, A. Schreyer, Th. Zeidler, C.F. Majkrzak, H. Zabel, J.A. Wolf and P. Grunberg (Neutron Optical Devices and Applications, **1738** (1992), 260), has been implemented at Chalk River. The program, called MLAYER, calculates the neutron reflectivity of a model layer profile in the limit of the plane wave Born approximation. The model profile is input to the program as a series of histograms representing the layers. Each layer is specified by its thickness, scattering power (defined as the square of the critical wave vector for total external reflection) and the linear absorption coefficient. The boundaries between layers could be sharp on the atomic scale, or be smoothed by a hyperbolic tangent or an error function. After achieving sufficiently good agreement between the measured and calculated neutron intensities, the user may choose to least-squares fit the parameters of the model, making the program a very versatile tool.

A local user's guide has been prepared for MLAYER. The guide also describes how the spectrometer data can be directly imported to the program, and how to plot measured and calculated (or least-squares fitted) reflectometry curves using local plotting programs.

Molecular Science

2.3.1.23 **Structure of Ice Grown in an Electric Field**

E.C. Svensson *(AECL)*, M. Farzaneh and M. Hamel *(Université du Québec à Chicoutimi)*, J. Bouillot and Y. Teisseyre *(Université de Savoie)* and R.L. Donaberger *(McMaster University)*

Rietveld refinement of the results from our earlier neutron diffraction measurements (PR-PHY-7:2.3.1.8; AECL-11016) on D_2O ice samples grown in high electric fields has now been completed. In all cases, the Rietveld analysis allows us to describe the observed diffraction profiles very precisely, which is of particular importance when very small changes occur in the structural parameters, as is the case in this study. A comparison of observed and calculated spectra is shown in Fig. 2.3.1.27, and the results from the refinements for all samples studied are listed in Table 2.3.1.1.

All samples have the $P6_3/mmc$ space group of ordinary ice Ih. For an applied electric field of -15 kV/cm, we see that the lattice parameters are larger than for zero field by about 0.08%. For a field of +15 kV/cm, the change is the same magnitude, but of opposite sign. A field of +22 kV/cm gives the same changes as +15 kV/cm. Growth in an electric field has little effect on the positions of the oxygen and deuterium atoms, but it has a marked effect on the thermal parameters (Debye-Waller factors) of the two deuterium atoms in the unit cell. For zero applied field, the mean square displacement of D1 and D2 due to thermal vibrations is well described by an elliptic surface, where one axis is about twice as long as the other two. For high applied fields, the corresponding surface is much closer to spherical, especially for D1.

In this first attempt to determine what happens structurally to ice grown in a relatively high electric field, we have found that ice retains a memory of its growth conditions, as revealed by such structural parameters as the lattice constants and the thermal factors. The effects on a and c are small but significant (20-30 times the estimated uncertainties), of opposite sign for opposite field polarity, and appear to saturate by +15 kV/cm. The effects on the thermal factors of the deuterium atoms are rather large.

In future studies we will investigate samples cooled rapidly to liquid nitrogen temperature (77 K) immediately after formation, to prevent possible relaxation of the structural changes induced by the electric fields, and samples grown over a wider range of fields to establish at which field(s) saturation effects occur. These new studies may also help to reveal why the sign of the change in the unit cell volume depends on the polarity of the field, an effect which is very puzzling at present.

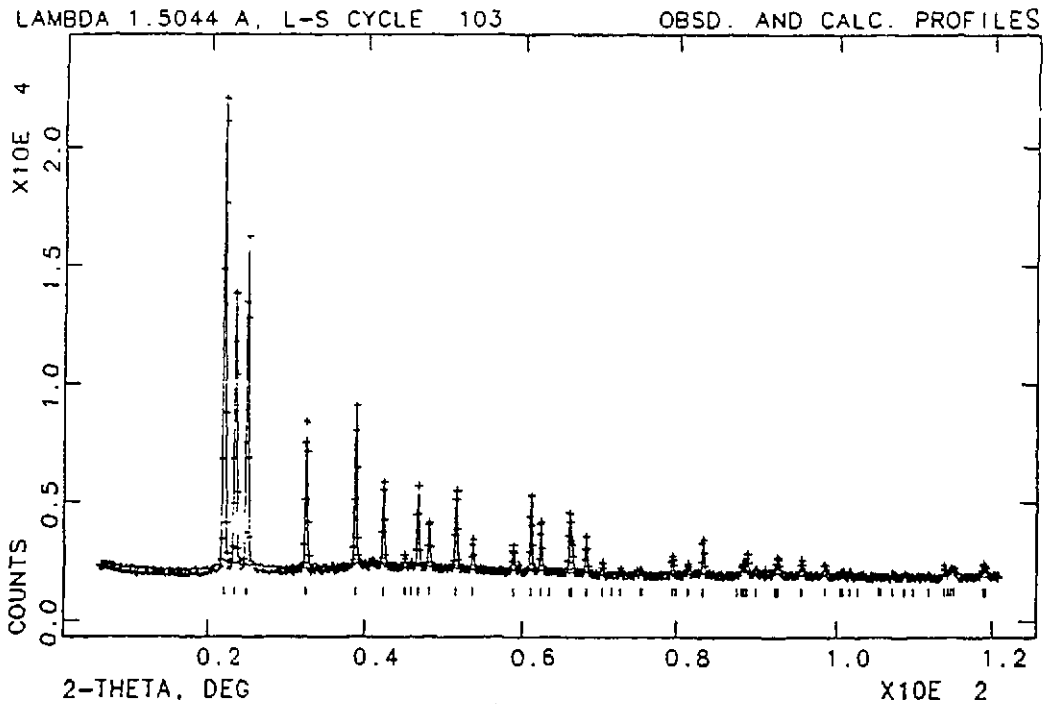

Fig. 2.3.1.27 Comparison of the measured spectrum (crosses) and the calculated spectrum given by the Rietveld analysis program for a fine powder of D_2O ice grown under an electric field of -15 kV/cm. The measurements were performed at 225 K.

Electric Field ($kV.cm^{-1}$)	Lattice Parameters		Z Positions (c unit)		Debye Waller Factors		
						D1	D2
Non Energized	a=b(Å)	4.5130(2)	oxygen O	0.0589(5)	B'_{11}	3.776	2,795
	c=(Å)	7.3486(3)	deuterium D1	0.1935 (5)	B'_{22}	7.619	6.830
	v=(Å^3)	129.618(13)	deuterium D2	0.0167 (6)	B'_{33}	3.777	3.866
+ 15	a	4.5091 (1)	O	0.0621 (6)	B'_{11}	5.201	4.372
	c	7.3426 (2)	D1	0.1977 (5)	B'_{22}	5.712	5.782
	v	129.286 (7)	D2	0.0177 (8)	B'_{33}	5.216	5.202
+ 22	a	4.5097 (1)	O	0.0626 (6)	B'_{11}	5.011	4.343
	c	7.3439 (2)	D1	0.1978 (4)	B'_{22}	5.384	5.529
	v	129.346	D2	0.0188 (8)	B'_{33}	5.013	5.037
-15	a	4.5164 (2)	O	0.0636 (6)	B'_{11}	5.210	3.681
	c	7.3540 (3)	D1	0.1977 (4)	B'_{22}	5.603	5.831
	v	129.909(13)	D2	0.0183 (8)	B'_{33}	5.180	4.615

Table 2.3.1.1 Refinement results for ice samples given by Rietveld analysis. The numbers in brackets are the standard deviations related to the last digits. The B'_{ii} are the Debye-Waller factors calculated in the principal axes of the ellipsoid. Their accuracy is of the order of 10%.

2.3.1.24 m=2 Ferroelastic Phase Transition and Lattice Melting in K_2CO_3

I.P. Swainson *(AECL)*

An experiment was performed, on the C2 DUALSPEC powder diffractometer, to investigate the ferroelastic phase transition in K_2CO_3. The interest in this transition is that K_2CO_3 is isomorphic to Na_2CO_3 above the transition temperature. In the case of Na_2CO_3 it has been shown by previous measurements on C2 and at ISIS (M.J. Harris, R.A. Cowley, I.P. Swainson and M.T. Dove, Phys. Rev. Lett. 71, (1993), 2939; I.P. Swainson, M.T. Dove and M.J. Harris, unpublished) that the crystal undergoes "lattice melting" at T_c followed by complete recrystallisation below T_c. This phenomenon is due to the fact that all the transverse acoustic modes in the a*-b* plane go soft, rather than a single branch of soft acoustic modes (M.J. Harris et al., *loc. cit.*; I.P. Swainson et al., *loc. cit.*). Such a transition is known as an m=2 ferroelastic, and Na_2CO_3 was the only known example of a continuous m=2 ferroelastic transition. The transition in Na_2CO_3 is from $P6_3/mmc$ to C2/m, with a two-dimensional soft mode of symmetry E_{1g}. K_2CO_3 was examined to see if the same effect would be seen in this structure. The low-temperature phase of K_2CO_3 has space group C2/c, not C2/m. However, the active representation in the paraelastic phase is also E_{1g}. The two different low-temperature space groups seen in K_2CO_3 and Na_2CO_3 are two different basis functions of E_{1g}. The "lattice melting" effect was seen very clearly in K_2CO_3, showing that it is the two-dimensional nature of the active representation that is the cause. In both carbonates, the structure can be envisaged as chains of NaO_6 or KO_6 octahedra stacked up the hexagonal c axis, linked together in the a-b plane by rigid planar trigonal CO_3 groups. Below T_c the CO_3 groups act as hinges for the ferroelastic distortion into the monoclinic phases. The "lattice melting" effect can be visualised in both systems as being due to the total loss of long range order along the c* axis (M.J. Harris et al., *loc. cit.*; I.P. Swainson et al., *loc. cit.*). The fluctuations that cause this disorder are fluctuations of this hinge mechanism.

2.3.1.25 Ferroelastic Phase Transitions in $K_3Na(SeO_4)_2$

S.M. Kim and B.M. Powell *(AECL)*, H. Kiefte *(Memorial University of Newfoundland)* and B. Mroz *(A. Mickiewicz University)*

Neutron powder diffraction measurements have been carried out on $K_3Na(SeO_4)_2$ in the temperature range 304 K to 390 K to observe the postulated ferroic phase transition from the space group $P\bar{3}m1$ to $P\bar{3}c1$ near 346 K, and a further discontinuous ferroelastic phase transition from the trigonal space group to the monoclinic structure C2/c at 334 K (PR-PHY-7:2.5.1.15; AECL-11016).

Rietveld analysis of the data shows that there is a discontinuous change in the slope of the temperature dependence of the lattice parameter, c, near 252 K, indicating a possible phase transition. The neutron powder diffraction profile is otherwise insensitive to the change of the space group from $P\bar{3}m1$ to $P\bar{3}c1$.

At 334 K, a first-order ferroelastic phase transition from the trigonal to monoclinic structure (space group C2/c) has been observed. The temperature dependence of the monoclinic distortion

shows that the order parameter, which is proportional to the monoclinic angle β, decreases from ~ 1.0 at 304 K to ~ 0.72 at 334 K. Attempts are being made to understand the observed phase transition in terms of the Landau theory of phase transitions.

2.3.1.26 Neutron Scattering Studies of the Ferroelastic Phase Transition in $(ND_4)_4LiH_3(SO_4)_4$

S.M. Kim and B.M. Powell *(AECL)*, H. Kiefte *(Memorial University of Newfoundland)* and B. Mroz *(A. Mickiewicz University)*

Crystals with the general formula $A_4LiH_3(SO_4)_4$, where A = Rb and NH_4, show tetragonal symmetry $P4_1$ (point group 4) at room temperature, and undergo a structural phase transition to the low-temperature monoclinic phase $P2_1$ (point group 2). From recent studies of Brillouin scattering (B. Mroz, H. Kiefte, M.J. Clouter and J.A. Tuszynski, J. Phys Condens. Matter **3** (1991), 5673) and neutron scattering (PR-PHY-6:2.5.1.7; AECL-10878), it is known that the transition observed in $Rb_4LiH_3(SO_4)_4$ at about 134 K is ferroelastic.

Neutron powder diffraction measurements have been carried out on deuterated $(ND_4)_4LiH_3(SO_4)_4$ compound as a function of temperature from 5 K to 290 K, in order to observe the tetragonal-to-monoclinic phase transition, and to determine the temperature dependence of the lattice parameters and the monoclinic angle. The measurements were made on the C2 DUALSPEC powder diffractometer located at the NRU reactor. Rietveld analysis of the data shows that the ferroelastic phase transition from the high-temperature tetragonal structure to the low-temperature monoclinic structure occurs at about 236 K. The observed temperature dependence of the lattice parameters and the monoclinic angle also shows that this deuterated ammonium compound is more ferroelastic than the rubidium compound: while the monoclinic angle at 5 K was 90.41 ± 0.02 degrees in the Rb compound, it was 90.96 ± 0.02 degrees in the ammonium compound. Attempts are being made to understand the observed temperature dependence of the order parameter, which is proportional to the monoclinic angle, in terms of the Landau theory of phase transitions.

2.3.1.27 Orientational Order-Disorder Phase Transitions in $NaNO_3$

I.P. Swainson and B.M. Powell *(AECL)* and M.T. Dove *(University of Cambridge)*

$NaNO_3$ is a structural analogue of the calcite system. Calcite possesses an orientational order-disorder transition, $R\bar{3}m$ to $R\bar{3}c$, at 1270 K, which is apparently tricritical (M.T. Dove and B.M. Powell, Phys. Chem. Minerals **16** (1989), 790). As most orientational order-disorder transitions are first order, this is a novel characteristic. Unusual diffuse scattering has been seen at points other than the critical zone boundary point (M.J. Harris, M.E. Hagen, M.T. Dove, I.P. Swainson, unpublished). Unfortunately, calcite breaks down below T_c unless a large partial pressure of CO_2 is applied, so a direct measurement of the disordered phase has not yet been made. In $NaNO_3$ the disordered calcite structure is stable (T_c = 553 K) over a narrow temperature range before true melting occurs (T_m = 579 K), and we have been able to directly measure this structure using the C2 DUALSPEC powder diffractometer. The results are in

agreement with previous molecular dynamics simulations of $NaNO_3$ (R.M. Lynden-Bell, M. Ferrario, I.R. McDonald and E. Salje, J. Phys: Condens. Matter **1** (1989), 6523).

In both calcite and $NaNO_3$ the order-disorder transition is tricritical, although there are some deviations away from this behaviour close to T_c for the case of $NaNO_3$. Previous models of these transitions had been Ising-like, in the sense that it is possible to achieve a "disordered" structure in which the trigonal carbonate groups sit in well defined orientations in a plus (0°) or a minus (180 or 60°) orientation. In these models it is expected that a partial occupancy could be refined for each of the orientations, and that close to T_c the partial occupancy for each becomes ~ ½ (J. Lefebvre, R. Fouret and C.M.E. Zeyen, J. Phys. **45** (1984), 1317).

In our previous measurements of calcite at temperatures up to T_c - 100 K, we found that this was a poor description of the structure. This has been borne out in the case of $NaNO_3$, where close to T_c the partial occupancy was impossible to refine. Instead, both studies have shown that the mechanism of disordering in these structures is one of continuous librational "melting", associated with a large growth in the in-plane libration (L_{33}). Once the mean-square libration reaches 30° it is no longer possible to specify which of the "Ising" orientations the NO_3 group occupies and the disordering transition is completed. Fig. 2.3.1.28 shows the Fourier map of a single NO_3 group, close to T_c. There is very little observed nuclear density in the opposite Ising-state. In these systems, therefore, the order parameter for the transition is the value of $\langle L_{33} \rangle$. In $CaCO_3$ the sample broke down when $\langle L_{33} \rangle = 18°$, whereas we were able to measure a continuous change in $\langle L_{33} \rangle$ up to 22° in $NaNO_3$.

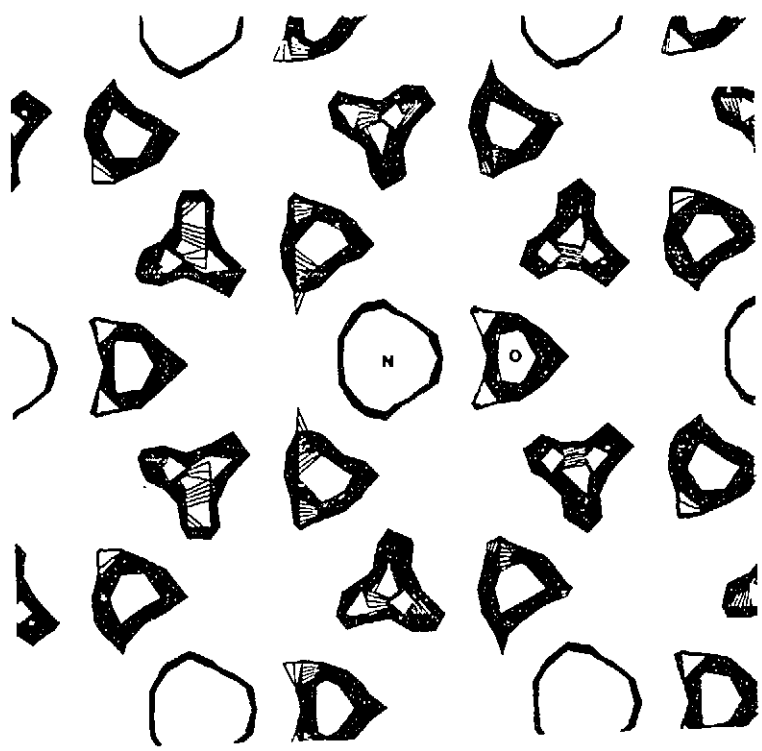

Fig. 2.3.1.28 Fourier section containing a single NO_3 ion close to T_c showing no appreciable nuclear intensity in the "opposite orientation".

Fig. 2.3.1.29 shows the behaviour of L_{33} as a function of temperature. The last two points are in the disordered phase. The apparent decrease in L_{33} at $T>T_c$ is model dependent, as the crystal symmetry $R\bar{3}m$ forces an "Ising-like" half-occupation of sites, and so the thermal factors are effectively reduced. We are currently planning more sophisticated ways of fitting this data. There is still a question as to the nature of the disordered phase. It is possible that the nitrate groups could become free, independent rotors, or else that there exist large domains in which the orientational fluctuations occur "in-phase". We believe that the in-plane interaction between neighbouring nitrates is strong, as the nitrate groups show a "ferro-" type orientational ordering right up to T_c and the refinements revealed effectively no "antiferro-" partial occupation. This may suggest that the "in-phase" model is a better description of the disordered phase.

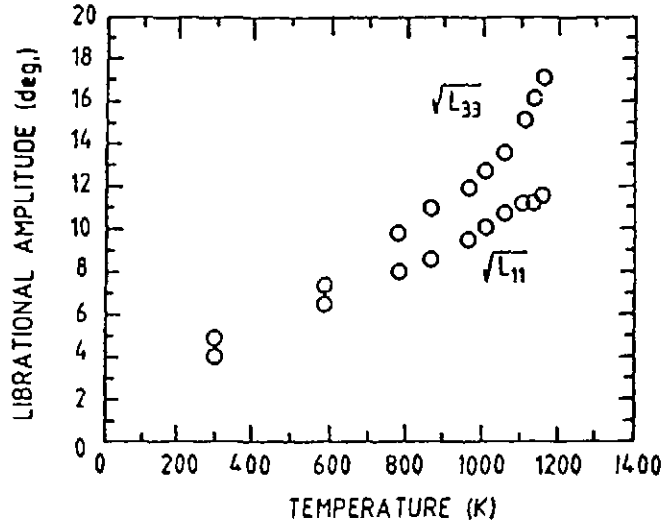

Fig. 2.3.1.29 L_{33} as a function of temperature shows a rapid increase near T_c as the transition is tricritical. The apparent reduction at $T>T_c$ is due to the restrictions imposed by the crystal space group.

2.3.1.28 **The Nature of the F-point Fluctuations in Calcite**

I.P. Swainson *(AECL)*

A transition isomorphic to that seen in $NaNO_3$ also exists in $CaCO_3$. This can be shown to be due to a soft mode instability at the Z-point zone boundary. Neutron powder diffraction data have shown that the chief disordering mechanism is a continuous growth of the in-plane libration, L_{33} (M.T. Dove and B.M. Powell, Phys. Chem. Mineral **16** (1989), 503; M.T. Dove, I.P. Swainson, B.M. Powell and D.C. Tennant, unpublished). This work has also demonstrated that $\beta = 1/4$, and the transition is therefore tricritical. Tricritical indices generally indicate competing interactions; e.g., close to a tricritical point. Other models which predict tricritical indices include the three-dimensional three-state Potts model (W.C-K. Poon and E. Salje, J. Phys. C: Solid State Phys. **21** (1988), 715).

Inelastic neutron scattering experiments performed on N5 and on PRISMA at ISIS have revealed that in addition to the main event at the Z-point, a strong column of inelastic scattering exists at the F-point (2.5, 0, 2) from zero energy transfer up to the energy of the zone boundary transverse acoustic (TA) mode at this point (M.T. Dove, M.E. Hagen, M.J. Harris, B.M. Powell, U. Steigenberger and B. Winkler, J. Phys: Condens. Matter **4** (1992), 2761; M. Hagen, M.T. Dove, M.J. Harris, U. Steigenberger and B.M. Powell, Physica B **180-181** (1992), 276). When the symmetry of the TA mode was examined, it was found that the space group of the phase that would be formed should this TA mode condense would be $P2_1/c$. It therefore seems highly likely that this is the origin of the competing interactions leading to tricritical indices.

Previous experimental work at high pressure has shown that the lowest high-pressure form of calcite, called $CaCO_3$ (II), is the result of a soft, zone-boundary acoustic mode at the F-point and is of symmetry $P2_1/c$ (L. Merill and W.A. Basset, Acta. Cryst. **B31** (1975), 343; D.M. Hatch and L. Merill, J. Chem. Phys. **23** (1981), 368). It would appear, therefore, that the incipient phase seen at ambient pressure as diffuse X-ray scattering and inelastic neutron scattering at the F-point is the high-pressure phase $CaCO_3$ (II).

2.3.1.29 The Influence of Sorbates on Acid Sites in H-SAPO-37

L.M. Bull and A.K. Cheetham *(University of California, Santa Barbara)* and B.M. Powell *(AECL)*

An earlier neutron diffraction study of the zeolite H-SAPO-37 (L.M. Bull, A.K. Cheetham, P.D. Hopkins and B.M. Powell, J. Chem. Soc., Chem. Commun. **1196** (1993), 1196) has shown that acid sites are present at O(1) in the α-cage, at O(2) close to the SII cation site, and at O(3) near the SI' cation site in the β-cage (Fig. 2.3.1.30). This is consistent with infrared studies (S. Dzwigaj, M. Briend, A. Shikholeslami, M.J. Peltre and D. Barthomeuf, Zeolites **10** (1990), 157) and would indicate that the protons at O(1) and O(2), which are accessible to the supercage, are responsible for the observed acidity. However, this deduction is not necessarily correct, because the protons with the highest occupancies, as determined by neutron diffraction, should be the most stable sites and hence the least acidic. To address this paradox we have used neutron diffraction and ^2H NMR to study the behaviour of benzene in H-SAPO-37. This combined approach has enabled us to probe the interaction between adsorbed benzene and acid sites in this prototypic acid catalyst.

Powder diffraction measurements were made on the DUALSPEC powder diffractometer at the NRU reactor, Chalk River Laboratories. The observed and calculated neutron diffraction profiles for perdeuterated benzene adsorbed in H-SAPO-37 (2 mol/s.c) are shown in Fig. 2.3.1.31. Benzene was found to be located both above the 6-ring window in two orientations, and in the plane of the 12-ring window, with occupancies of 6.3%, 7% and 25.1%, respectively, but protons could only be located at O(2) with an occupancy of 10.2% (Fig. 2.3.1.30). The number of protons located falls well short of the expected proton content. However, proton/deuterium exchange between the deuterons on the benzene ring and protons on the framework does not appear to be affecting the results, as no exchange was observed from the ^1H MAS NMR spectrum of perdeuterated benzene adsorbed in H-SAPO-37. The low-temperature ^2H NMR lineshape of

benzene adsorbed in H-SAPO-37 (~ 1 mol/s.c.) is typical of benzene rotating around its 6-fold axis, and is therefore participating in a facial interaction with the proton on O(2).

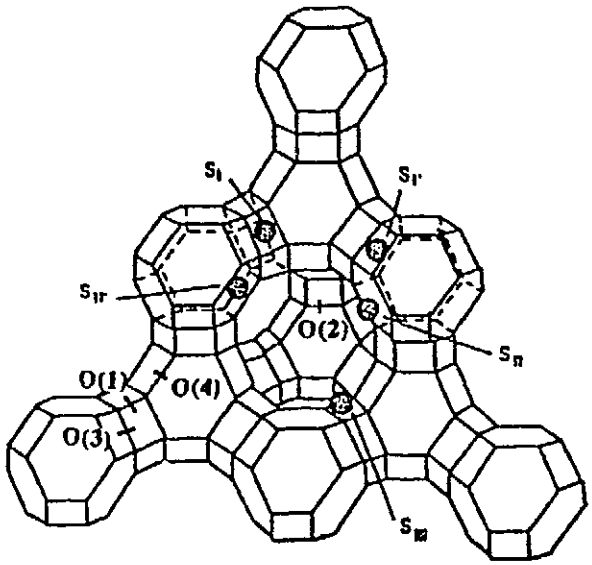

Fig. 2.3.1.30 SAPO-37 structure showing the positions of the four oxygens sites that may be protonated.

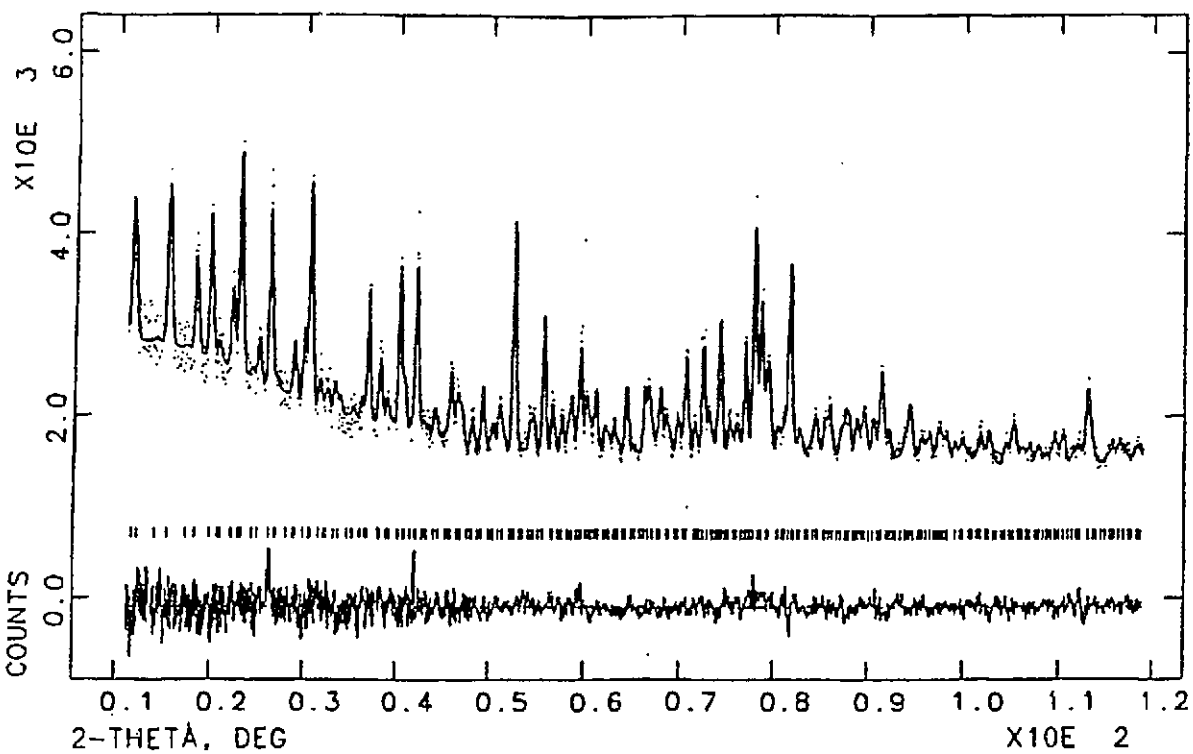

Fig. 2.3.1.31 Experimental, calculated and difference profiles of H-SAPO-37 with adsorbed benzene. The high and low angle data have only been merged for the purpose of the figure.

The earlier diffraction study of the parent H-SAPO-37 material revealed protons at O(1), O(2) and O(3), whereas protons are observed only at O(2) upon adsorption of benzene. This result indicates that the protons are redistributing themselves among the oxygen sites in order to interact more favourably with the sorbate. This conclusion is consistent with I.R. measurements which show that the OH stretching band associated with protons in the α-cage is shifted to lower frequencies on adsorption of benzene (S. Dzwigaj, M. Briend, A. Shikholeslami, M.J. Peltre and D. Barthomeuf, Zeolites **10** (1990), 157). We argue that the OH species associated with O(1) are the ones in the α-cage, and that the OH stretching frequency is lowered when these protons move to O(2) in order to bind to the benzene at the location above the 6-ring; the O-H bonding is presumably slightly weakened by the proton-benzene interaction.

2.3.1.30 Crystal Structure of Freon 21 - $CHCl_2F$

B.H. Torrie, O.S. Binbrek and R. Pridmore *(University of Waterloo)* and B.M. Powell *(AECL)*

As part of a comprehensive study of halogen substituted methanes, the Raman and infrared spectra of solid Freon 21 were recorded. No evidence of phase changes in the temperature range 12-130 K was found (m.p.=138 K). The lattice spectra are consistent, with the unit cell being non-centrosymmetric and containing at least four molecules.

Further interpretation of the spectra requires a precise determination of the crystal structure and, with this in mind, the neutron powder profiles of Freon 21 were recorded for temperatures in the range 5 to 105 K. Measurements on the C2 DUALSPEC powder diffractometer were made at a long wavelength (2.4145 Å) to facilitate the indexing of the peaks, and at a shorter wavelength (1.3536 Å) to give a large number of peaks for a full structural analysis. Contrary to expectations, the structure at the higher temperatures is centrosymmetric, space group Pbca, with eight molecules in a unit cell. The powder patterns remain basically the same at all temperatures, so the same structure can be used to fit all patterns. However, there are a small number of additional intense peaks which appear in the 55 K pattern and another, different, small number which appear in the patterns recorded at 30 and 5 K. These peaks are likely associated with major reorientations of the molecules, but their origins are not understood at the moment.

2.3.1.31 Phonon Density of States in Cristobalite

V.F. Sears and I. Swainson *(AECL)*

Cristobalite is a form of silica (SiO_2) with a cubic structure consisting of SiO_4 tetrahedra in which each oxygen atom is shared by two neighbouring tetrahedra. It undergoes an order-disorder phase transition at 270°C from a low-temperature α phase, in which the SiO_4 framework is distorted and the crystal has correspondingly low symmetry, to a high-temperature β phase in which the framework is undistorted and the crystal has high symmetry. Molecular dynamics calculations predict that the phonon density of states $g(\nu)$ is very similar in both phases. The main difference is at low frequencies ($\nu < 2$ THz) where, in the α phase, $g(\nu)$ increases roughly quadratically with ν to a peak at 1.8 THz that arises from zone-boundary TA modes. In the β phase, on the other

hand, the large degree of dynamic disorder produces additional low-frequency modes so that $g(\nu)$ increases roughly linearly with ν and levels off at about 1.5 THz.

We have analyzed neutron time-of-flight measurements for the α phase at 20°C and the β phase at 320°C that were taken at the ISIS spallation source of the Rutherford-Appleton Laboratory. The $g(\nu)$ curves obtained from this analysis are in rough qualitative agreement with the molecular dynamics results discussed above, but the peak in the α phase and the shoulder in the β phase both occur at a lower frequency of 1.2 THz. Neutron inelastic scattering measurements at constant Q will be made on the N5 triple-axis spectrometer at NRU when a powder sample of cristobalite of suitable quality is obtained.

2.3.1.32 Powder Diffraction Studies of Lithium Manganese Oxides

J.H. Dahn, E. Fuller and W. Li *(Simon Fraser University)* and J.H. Root *(AECL)*

Lithium can be intercalated into a variety of materials through aqueous electrochemical methods, if the materials are stable in concentrated Li+ solutions and if Li+ intercalation takes priority over hydrogen intercalation. Data acquired on the DUALSPEC powder diffractometer has provided evidence that the undesirable product, $Mn(OH)_2$, is formed by continuing an electrolytic reaction beyond 1 electron per mole, when making spinel $Li_2Mn_2O_4$ from spinel $LiMn_2O_4$.

Material Science

2.3.1.33 Investigation of Residual Stresses in a Sleeve Cold-Worked Lug Specimen by Neutron Diffraction

T.M. Holden, R.B. Rogge and J.H. Root *(AECL)*, R. Lin *(Studsvik Neutron Laboratory)* and B. Jaensson *(Saab-Scania AB)*

Sleeve cold-working is a mechanical process used in the aircraft industry to strengthen fastener holes on structural parts. A knowledge of the residual stresses generated by this process is crucial for assessing the fatigue properties of a treated part. The residual stresses were investigated by neutron and X-ray diffraction in a lug specimen that was sleeve cold-worked and fatigued. The measurements were made with neutrons of wavelength 1.55 Å and a radial spatial resolution of 1.5 mm. Very large (-300 MPa) compressive hoop stresses were observed close to the edge of the hole, which were balanced by tensile hoop strains beyond about 7 mm from the edge of the hole. The radial and transverse stresses were much lower, being essentially zero beyond 10 mm from the edge of the hole, and compressive (-100 ± 30) MPa near the hole. The X-ray surface measurements indicated that at the surface the hoop compressive stress (-200 MPa) was less than the stress at depth. The residual stresses were modelled by considering a thick-walled ring subjected to pressure on the inner diameter within a linear elastic-plastic approximation. This model neglects the physical interaction and friction between the mandrel used to sleeve cold work and the sample, and does not include the geometry of the lug sample. The model calculation with no variable parameters is in quite good agreement with the experiments, especially for the hoop component close to the hole, although the balancing tensile stress well away from the hole is over-estimated by 30-50%.

2.3.1.34 Measurements of Residual Strain in an Aluminum Casting Alloy Engine Block

T.M. Holden, R.B. Rogge and J.H. Fox *(AECL)*, G. Sokolowski and G. Byczynski *(University of Windsor)*

Neutron diffraction measurements of residual strain were made in the bulk-head region of an engine block fabricated from an aluminum casting alloy. The component of strain parallel to the crank-shaft direction was initially examined with a gauge volume of approximately 1 cm^3. Very marked variations in peak intensity were noted as the gauge volume was traversed across the bulk-head, indicating very large grain sizes in this region. The fluctuations in peak position accompanying the changes of intensity completely masked any systematic variation in strain in the bulk-head. Metallography later indicated grain dimensions of order several *mm* in the bulk-head.

2.3.1.35 Strain in a Plate with a Through-Hole under Load

T.M. Holden, R.B. Rogge and J, Fox *(AECL)*, L. Clapham, T.W. Krause and D.L. Atherton *(Queen's University)*

Strain measurements have been made by neutron diffraction in thin hot-rolled steel plates (150 x 75 x 3 mm^3) with 12.7 mm diameter holes under an axial stress of 80 MPa in the stress rig. Axial strains were measured on a plate in which a hole had previously been drilled and which was then loaded, and on a plate which was loaded and then drilled out in situ. The motivation for the experiment is that defects form under operating conditions in line-pipe, and it is important to know the stress intensity factor, the magnification of the stress near the defect under load. The applied stress was designed to be such that the yield point (presumed to be greater than 240 MPa) was never exceeded, even near the hole. The solution for the first case may be obtained analytically, and there is good agreement between theory and experiment. It was anticipated that the second case would be identical to the first, since the final states (loaded plate with hole) were the same. The observations disagreed completely with this prediction. The axial strains at the six o'clock position near the hole (see Fig. 2.3.1.32), instead of being large and tensile, were essentially zero. The axial strain increased with distance from the edge of the hole along the zero meridian. The axial strain at the three o'clock position under load was also zero. Upon unloading, the residual strain at the six o'clock position became strongly compressive, while that at the three o'clock position remained near zero. A necessary requirement for generating a residual stress is that there should be inhomogeneous plastic deformation. It is probable that the process of drilling generates time-dependent stresses which, when added to the applied stress, exceeds yield, or else the process of drilling the hole under load had momentarily exceeded yield. Since the observations have implications for gas pipeline technology, the experiments will be repeated with more rigorous control of materials and machining.

Through-Hole in 3 mm Thick Steel Plate

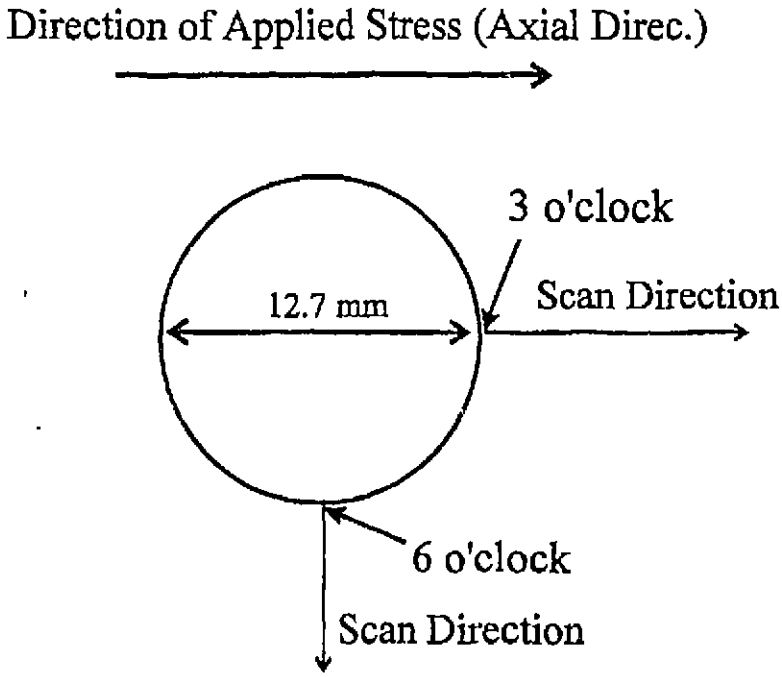

Fig. 2.3.1.32

2.3.1.36 **Residual Stresses in Welded Rails**

T.M. Holden *(AECL)*, P.J. Webster, G. Mills and X.D. Wang *(University of Salford)*

Wherever possible, railway rails are now joined by welding, which is a cheaper method than bolting and produces a superior joint. However, it is necessary to measure the welding residual stresses to ascertain the safety of the product. The standard technique for joining rail is alumino-thermic welding, in which the rails are aligned with a gap of about 24 mm between the ends. A mould is made around the gap and a mixture of iron alloy, iron oxide and aluminum powder is contained in a hopper above it. The mixture is ignited and molten steel flows into the gap to make the weld.

The samples were plate sections 10 mm thick, 156 mm high and 400 mm long, cut longitudinally from the rails with the weld near the center. This process substantially reduces the transverse stresses, but not the vertical and longitudinal stresses. Measurements were made with a spatial resolution of 2 mm at a grid of points separated by 10 mm on the L3 and E3 spectrometers.

Examples of longitudinal and vertical results for vertical, z, scans at four longitudinal, x, locations are shown in Fig. 2.3.1.33. The macroscopic stress distributions in each rail, at x = 70 mm, show mostly tension in the head and foot and compression in the web, as expected. In the weld, at x = 200 mm, the situation is largely reversed, with tension in the web and longitudinal compression at the top and bottom. Stresses are generally lowest near x = 135 mm, about 65 mm from the weld line. Boundary effects are observed near the ends. The stress pattern in the weld is generally beneficial, as it would tend to inhibit transverse surface cracks starting at the surface. Peak intensity data indicated some regions of preferred orientation within the weld. In the heat-affected zone, microstresses had been relieved presumably by heat from the weld.

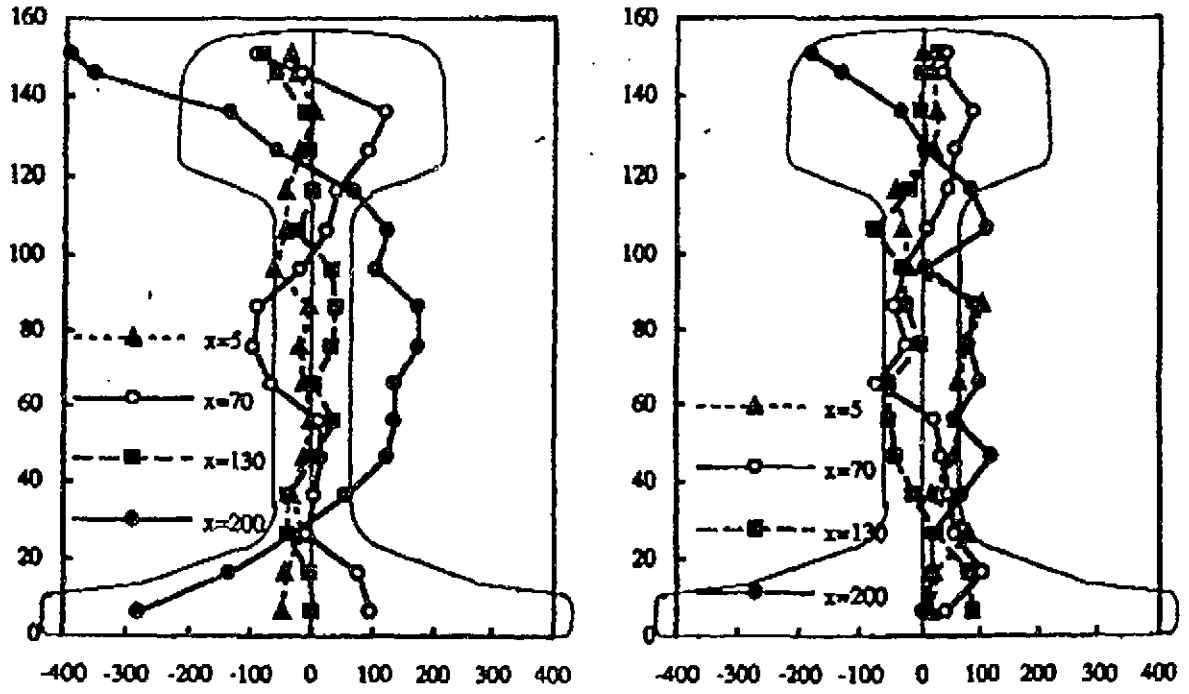

Fig. 2.3.1.33

2.3.1.37 Radial Residual Strain Distribution Through Extruded Al:SiC

T.M. Holden *(AECL)*, N. Towneley and D. Boyd *(Queen's University)*

The distribution of residual strains across the diameter of a 12.7 mm extruded rod of the metal matrix composite Al:SiC was measured by neutron diffraction. The experiments were carried out at the L3 spectrometer with neutrons of wavelength 1.96 Å reflected from the (331) planes of a Ge monochromator. Measurements were made with the Al (113) diffraction peak at 105° and

the SiC (220) peak at 75°. These peaks were chosen because neither one was overlapped by other diffraction peaks. Measurements were also made of the lattice spacing of SiC powder and a sample of the extruded Al alloy corresponding to the matrix. To within the experimental errors there was no radial strain variation in the extruded bar. The average radial and hoop strain in the Al matrix was $(1 \pm 0.5) \times 10^{-4}$ and in the SiC $(-4 \pm 1) \times 10^{-4}$. The average axial strains were $(-3 \pm 1) \times 10^{-4}$ and $(-8 \pm 1) \times 10^{-4}$. These results are very similar to the volume averaged strains in extruded bar observed previously. We conclude that the extrusion does not generate a macroscopic residual stress field in Al:SiC rod. The stresses observed are due solely to the interphase constraints. The anisotropy of the strain is attributed to the net difference in the spatial separation of the SiC particles in the radial/hoop and axial directions caused by extrusion, as well as the alignment of the fragments of SiC reinforcing material, with their long direction along the extrusion direction. Differences in aspect ratio parallel and perpendicular to the extrusion direction can generate average differences in strain.

2.3.1.38 Residual Stresses in Diffusion Bonded SiC/Mo Joints

A.E. Martinelli and R.A.L. Drew *(McGill University)*, R.B. Rogge and J.H. Root *(AECL)*

The use of ceramic-metal systems as structural components has gradually increased over the years. They are generally used as protective coatings for metallic structures, and in the fabrication of composites and joined components for fusion reactor technology, and the automotive and aircraft industries. An attractive ceramic/metal combination involves silicon carbide (SiC) and molybdenum (Mo). The joints are fabricated by solid-state diffusion bonding. Although temperature-resistant interfaces are established, high concentrations of residual stress are generally found near the ceramic-metal interface, due to a misfit in the thermal expansion coefficients. Thermal stresses reduce the mechanical strength of the joint and may result in failure of the component.

Neutron diffraction analyses were performed to measure the residual stresses near the interface of SiC/Mo specimens that were joined at temperatures ranging from 1200°C to 1500°C, maintained for different times. The results indicate that the level of stress (normal and in-plane components) increased with joining temperature and time, but the stress distributions are similar (Figs. 2.3.1.34 and 2.3.1.35). The shape of the stress curves, especially the in-plane component, showed reasonably good agreement with FEM (Finite Element Method) calculations obtained by Y.C. Kim, T. Yamamoto and T.H. North, (Trans. Japanese Welding Res. Inst. **21** (1992), 145). However, their model assumes complete bonding between ceramic and metal, which is not the case. In reactive ceramic systems such as SiC/Mo, the temperature and time necessary for complete bonding results in excessive growth of the interfacial reaction layer, which is extremely detrimental to the mechanical strength of the joint. It is believed that the presence of interfacial unbonded islands resulted in scatter of the neutron data. Further analyses are necessary to better understand the effect of unjoined islands. This information will be valuable in the optimization of fabrication parameters for SiC/Mo joints, improving the mechanical strength of the final components.

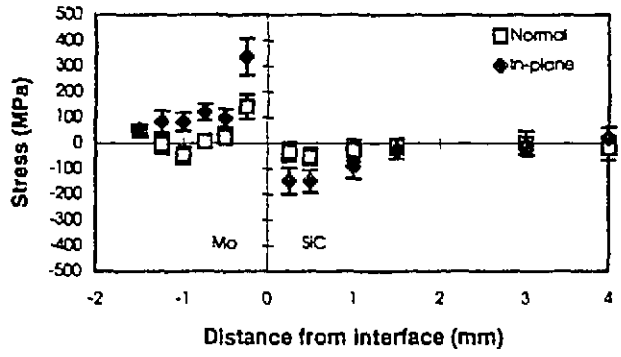

Fig. 2.3.1.34 Stress distribution for SiC/Mo sample hot-pressed at 1200°C for 1 hour.

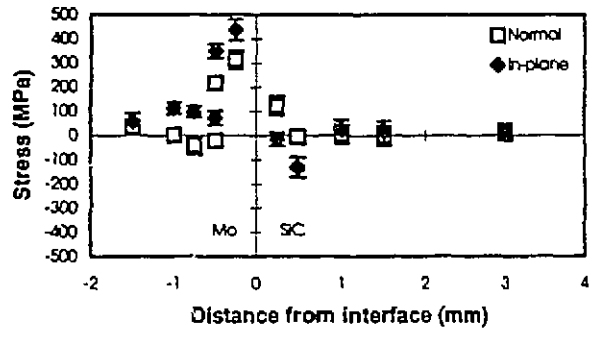

Fig. 2.3.1.35 Stress distribution for SiC/Mo sample hot-pressed at 1400°C for 1 hour.

2.3.1.39 Residual Stress and Texture in Extruded Aluminum Bar

S.R. MacEwen and A. Langille *(ALCAN International)*, J. Savoie *(McGill University)* and J.H. Root *(AECL)*

The extrusion of aluminum billet results in high deformation, high shear rates and significant amounts of dissipative heating in the vicinity of the die bearing. Despite its importance in the design of extrusion dies, it has not been possible to measure directly the precise nature of the shear in a die during operation. However, neutron diffraction has provided a non-destructive map of the residual strain gradients and texture gradients across the diameter of a cylindrical, extruded aluminum bar. The symmetry axis of the texture rotates monotonically about the hoop direction, from the axial direction, at the centre of the bar, to a direction in the axial-radial plane (about 16° from the axial direction) near the surface of the bar. This pattern is linked to the streamlines of the metal flowing through the extrusion die. The residual axial strains exhibit a pattern that is typical of a quench, slightly tensile at the centre of the bar, and compressive towards the surface.

This pattern arises from the water-cooling of the hot bar after it exits from the extruder. The results on texture and residual strain indicate that neutron diffraction provides a good *post mortem* tool to analyze the process of extrusion.

2.3.1.40 Mullite Fibre-Reinforced Aluminum Piston Head

A.P. Clarke and T.M. Holden *(AECL)*

A 12 cm diameter aluminum piston-head casting was obtained from General Motors. It had been cast with a reinforcing ring preform of mullite mineral fibre (cross-section = 10 mm x 15 mm) at the outside top corner of the piston head. Using the E3 spectrometer at NRU, the three principal strains (Hoop, Radial and Axial) in the aluminum matrix were determined every millimetre on 4 loci running from the outside top surfaces of the piston (Fig. 2.3.1.36) through the reinforced ring and into the pure Al casting.

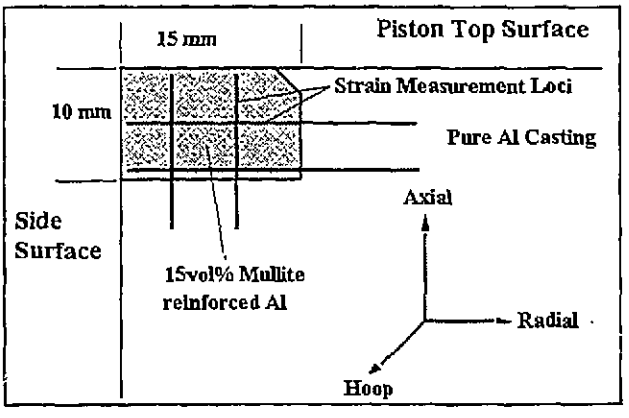

Fig. 2.3.1.36

The strain measurements contained a large amount of scatter in excess of the estimated statistical precision, possibly due to grain size or uneven distribution of the reinforcing fibres. As a result, any differences between parallel loci were not resolved and, to calculate the principal stresses, measurements along parallel loci were averaged and smoothed. The calculated stresses for the average of the two loci running parallel to the top surface are shown in Fig. 2.3.1.37 (closed data points). These indicate the expected tensile residual stresses in the reinforced region due to the large coefficient of thermal expansion (CTE) difference between the Al and mullite fibre (CTE = 21 x 10^{-6} and 3 x 10^{-6}, respectively). The total stresses decline to zero at large distances into the pure Al region of the casting.

The total stress is a superposition of the micro-stresses, due to the CTE difference between the Al and Mullite phases within the composite, which are balanced over the grain size, and long-range stresses due to the difference in average CTE of the Al/mullite composite region and the adjoining pure Al region. From strain measurements on a piece of reference composite, it was possible to estimate the micro-stresses and to calculate the long-range stress field (open data points) by subtraction. A linear variation of the microstress between the maximum value inside

the reinforcing ring, and zero outside, was assumed. The results indicate the presence of a significant compressive Hoop stress in the composite region, balanced by a tensile stress in the pure Al region. Both the Axial and Radial long-range stresses appear to be smaller, and this is consistent with the results from the loci running parallel to the outside surface of the piston, which show only small, long-range tensile stresses in the pure Al region below the composite ring.

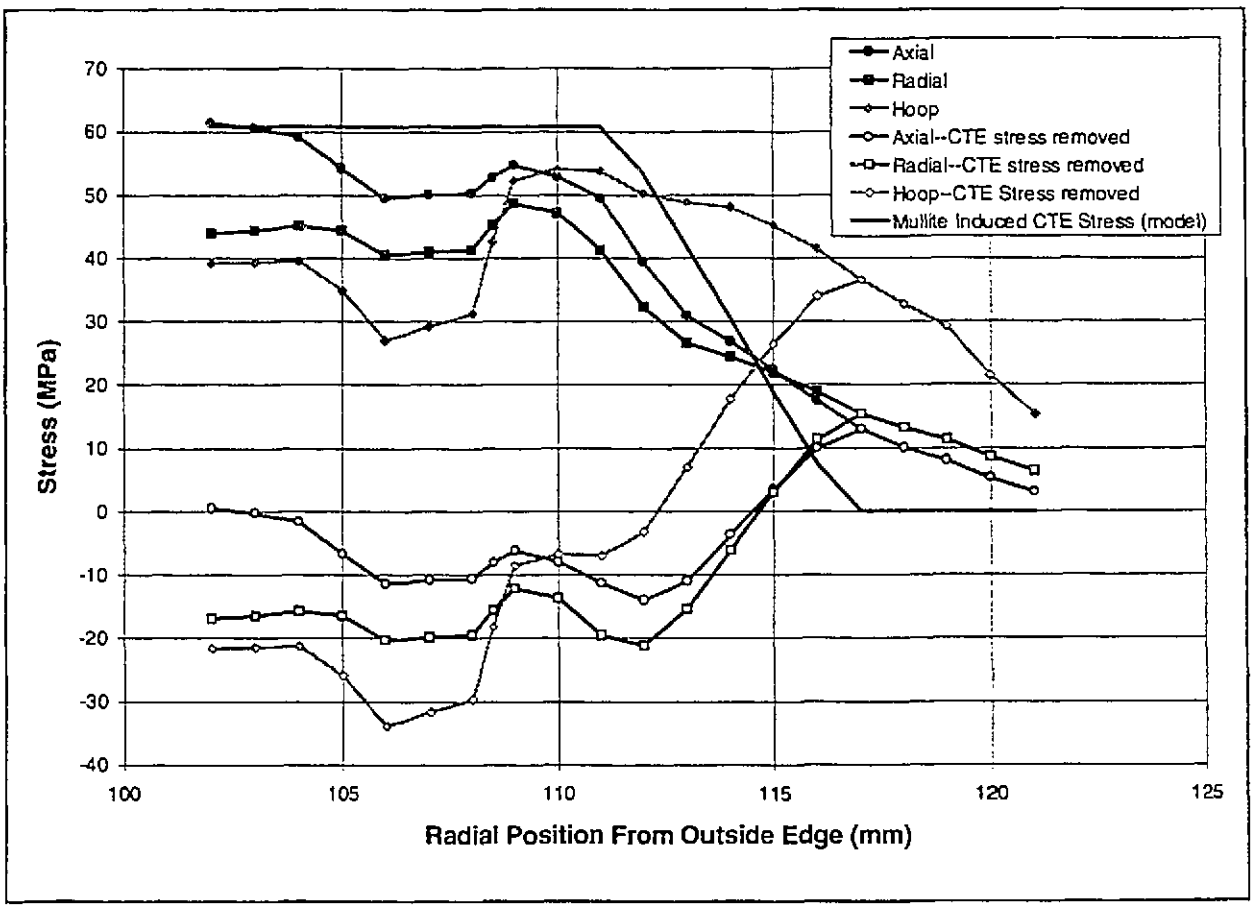

Fig. 2.3.1.37

2.3.1.41 Lattice Strain Measurements of SiC Fibre Reinforced Titanium During Tensile Testing

A.P. Clarke *(AECL)* and P.J. Withers *(University of Cambridge)*

To investigate the details of load transfer to the strong reinforcing phase of a continuously reinforced composite, strain measurements were made on Ti tensile samples reinforced with continuous SiC fibres, while cyclic tensile tests were performed on the L3 spectrometer at NRU. Strain measurements were made with both the SiC phase and several reflections of the Ti phase, with the samples oriented so that the scattering vector was in the direction of the applied stress. Three samples were tested: (1) SiC fibres aligned along the stress direction; (2) SiC reinforcing fibres aligned transversely to the applied stress; (3) unreinforced Ti standard.

The results show the development of large compressive residual strains at zero load in the Ti matrix due to the transfer of stress to the SiC phase. These strains are apparent even with cycling to very low loads in the nominally elastic/linear region of the true stress versus strain curve, and equivalent tensile shifts were measured in the SiC fibres. The results from the sample loaded parallel to the fibre direction are shown in Fig. 2.3.1.38. The SiC data were shifted by a strain of 0.001 for clarity. The shifts indicate that an extra 240 MPa was transferred to the SiC fibres from the Ti matrix at the point of failure. The unreinforced Ti showed development of strain offsets with the different reflections as well. This was attributed to intergranular stresses due to different orientations of crystallites sampled with different reflections.

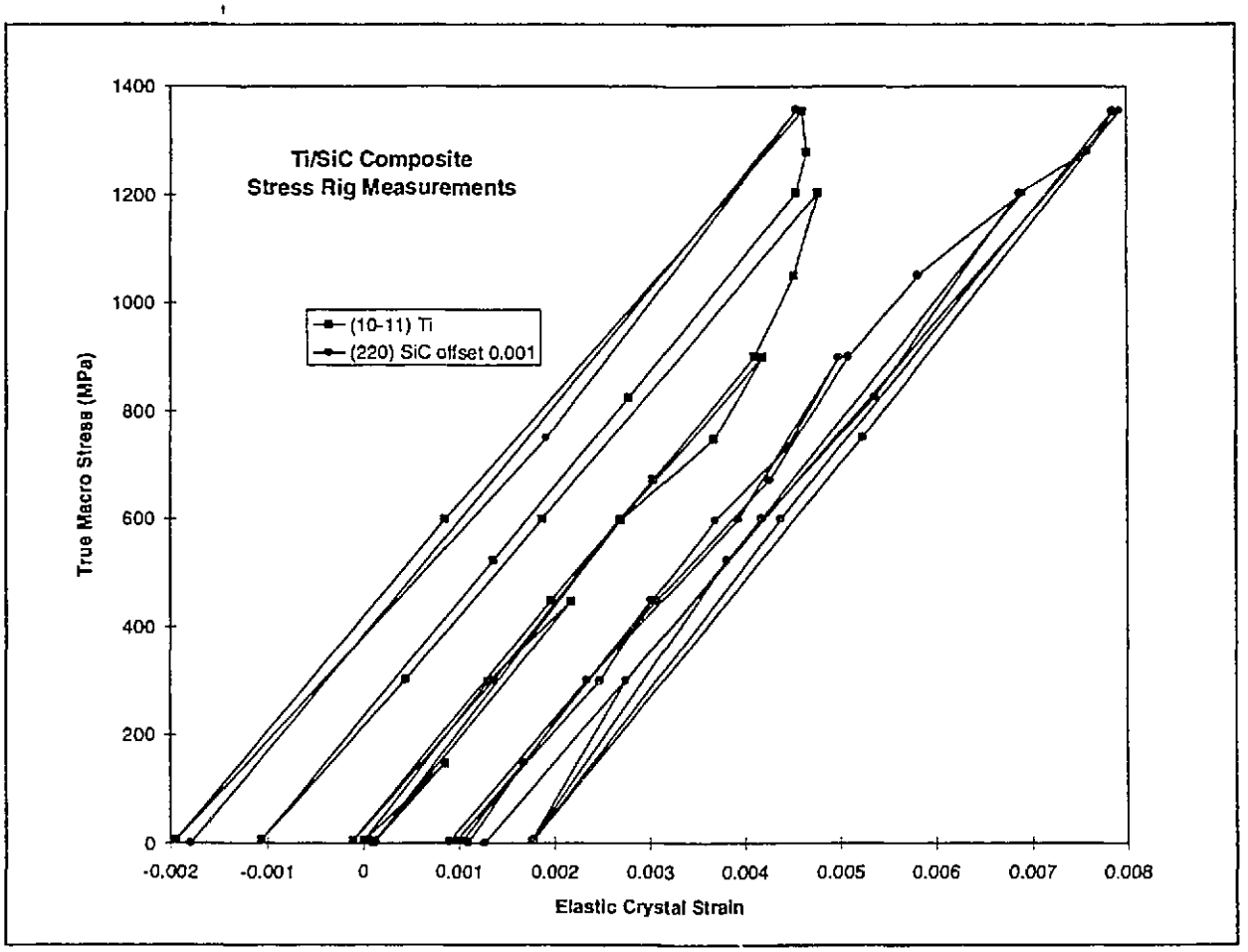

Fig. 2.3.1.38

2.3.1.42 Stresses Near Fatigue Cracks in Particulate SiC Reinforced 2124 Al

A.P. Clarke *(AECL)* and P.J. Withers *(University of Cambridge)*

Standard edge-notched bend (SENB) samples were cut from unreinforced and 20 wt% 3 μm SiC particulate reinforced 2124 Al alloy plates, that had been water quenched from 505°C to induce

a parabolic residual strain field through the thickness of the plate. After fatigue testing the bars in a 4-point bend apparatus, the form of the elastic strain variation in the vicinity of the fatigue crack was investigated using the L3 spectrometer at NRU and an *in situ* 4-point bend apparatus. The strain distribution was measured along the crack axis with the crack fully open (K_{max}--maximum applied stress intensity) and fully closed (K=0--minimum applied stress intensity) within the Al matrix for both the composite and unreinforced bars, and within the reinforcing particles for the composite bar. The role of quenching-induced residual stresses was also examined by making equivalent strain measurements away from the crack.

The strain measurements far from the crack show the expected parabolic strain variation due to the quench. Subsequent metallographic inspection confirmed that the parabolic strain field had produced a linear crack front through the thickness of the bar. Figs. 2.3.1.39 and 2.3.1.40 show the strain measurements along the crack axis for the unreinforced and composite bars, respectively. In both cases, large tensile residual stresses are observed near the crack tip at K_{max}. The presence of significant stresses at K=0 in the unreinforced bar indicates the presence of significant crack closure in the unloaded case. This effect is magnified in the composite bar and is attributed to the role of the interphase stresses induced by the SiC. The observed K=0 tensile stress effectively reduces the applied stress intensity range (ΔK), which is the critical factor in fatigue crack growth rate, and explains the generally observed reduction in fatigue crack growth in metal matrix composites.

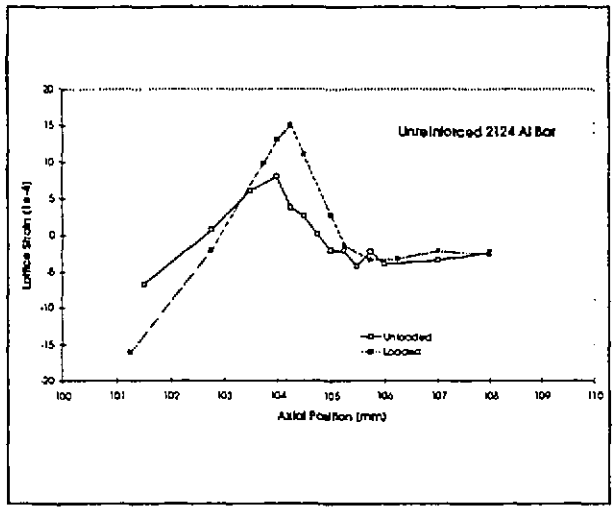

Fig. 2.3.1.39 The matrix strain in the crack opening direction along the crack axis. Crack tip pos. = 104.6 mm.

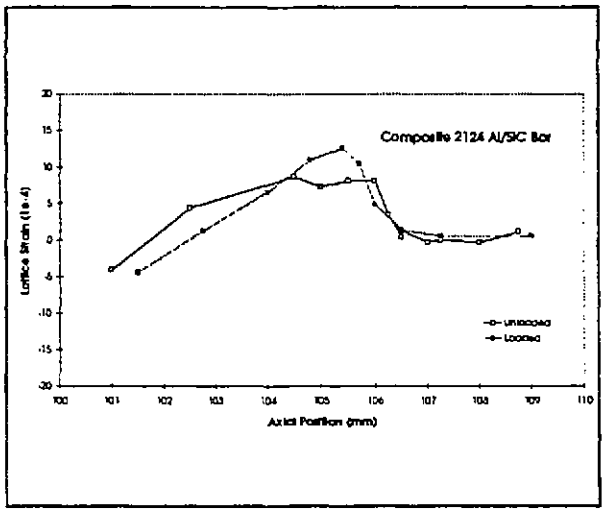

Fig. 2.3.1.40 The matrix strain in the crack opening direction along the crack axis. Crack tip pos. = 106.2 mm.

2.3.1.43 **Thermal Expansion Strains in Extruded SiC Particulate Reinforced Al(Cu)**

T.M. Holden and A.P. Clarke *(AECL)*, N. Towneley and D. Boyd *(Queen's University)*

To investigate the effect of thermo-mechanical treatments on the details of inter-particle thermal expansion stresses, samples of Al(4wt% Cu) reinforced with 20vol% SiC particulate composite were received from Alcan in the as-cast condition, along with samples of the virgin matrix alloy and quantities of the SiC powder. Rods were extruded from the cast composite with an extrusion ratio of 20:1 at 400°C. Five sets of samples (as-cast, extruded, and unreinforced Al) were prepared and four were annealed at 510°C for seven hours and then slowly cooled (1.5°C/min) to 510, 410, 307 and 250°C, respectively, followed by a water quench. After performing strain measurements, the samples that had been slow cooled to 307 and 410°C were quenched in liquid nitrogen and reheated to room temperature for further measurements.

Using the E3 spectrometer at NRU, the lattice parameters in the extrusion and transverse orientations were measured in both the Al(Cu) and SiC phases, and the residual strains were calculated using lattice parameter measurements from the SiC powder and unreinforced Al(Cu) alloy that had received the same heat treatment.

The results showed the expected compressive strains ($\varepsilon_{ext} \approx -7 \times 10^{-4}$) in the SiC particles balanced by a tensile strain in the Al(Cu) matrix. In the extruded samples there were distinctly higher residual strains in the extrusion direction than the transverse ($|\varepsilon_{ext}-\varepsilon_{trans}| \approx 3 \times 10^{-4}$) for both phases. This difference was not present in the as-cast samples. Since the extended anneals at 510°C did not remove this asymmetry, it was concluded that the difference in the residual strain

was not due to the effect of plastic flow during extrusion, but to either the alignment of the small aspect ratio (≈1.8) in the particles with the extrusion direction, or the alignment of particles in extended chains with a small extrusion direction spacing and larger transverse spacing. Work is continuing to quantify these morphological effects metallographically, and to model their effects on the strains in the composite.

There was a small, measurable effect of the quench temperature. The strain in the SiC phase was found to be 2×10^{-4} more compressive in the samples quenched at 510°C than in the samples quenched at 250°C. This was consistent with the expected coarsening of the Cu precipitates at the lower quench temperatures, resulting in a lower matrix strength. Finally, the liquid nitrogen treatment reduced the strains by 2×10^{-4} without altering the extrusion-transverse asymmetry.

2.3.1.44 Near-Surface and Near-Interface Strain Measurements by Neutron Diffraction

R.B. Rogge and T.M. Holden *(AECL)*, X.D. Wang, G. Mills and P.J. Webster *(University of Salford)*

The non-destructive determination of residual stress by diffraction techniques has traditionally been separated into two regimes, (1) measurements very close to the surface (typically of order μm) with X-rays and (2) measurements at depth (typically of order mm) utilising the high penetration of neutrons. Investigation of the region between these extremes had previously required the systematic removal of surface layers, thereby destroying the specimen. We have successfully developed a neutron scattering technique to probe continuously from the surface, providing a continuous link between neutron and X-ray data.

The ability to perform these measurements inside the specimen also provides the opportunity to investigate interfaces. This is not possible with X-rays, unless the mating material is a very thin surface layer. But the physical properties of this interface may vary significantly from the ultimate industrial application for which the interface may be between relatively large components. Since a thick layer of both materials is present, strain measurements can be performed in each material, providing additional information about the bond.

We have previously reported (PR-PHY-7: 2.3.1.20; AECL-11016) that various sources of systematic errors, wavelength distribution across the beam, geometrical offset, and peak-clipping, have been reduced to the level of the statistical error in the measurements. The new 32-wire detector has further improved data collection efficiency. Standard mode data collection is improved by a factor of 3 and the special data collection mode (previously reported above) is now a factor of 10 better than a single detector (previously a factor of 5 was realised). Test measurements on a strain-free Ni powder show that the conventional multiwire method can be used as long as the gauge volume is at least half filled, provided the exit slit to gauge-volume center distance remains small. If the gauge volume is less than half filled, the special scan method must be used. This combination of scan methods further reduces the total measurement time, making the technique economically feasible.

Measurements on WASPALOY plate samples of heavy, medium and light shot peening intensity have been performed. Data for the heavy peened sample are shown in Fig. 2.3.1.41. The

measured stress profile, namely near-yield compressive in-plane stress just below the surface going to a peak tensile in-plane stress, is characteristic of shot peening.

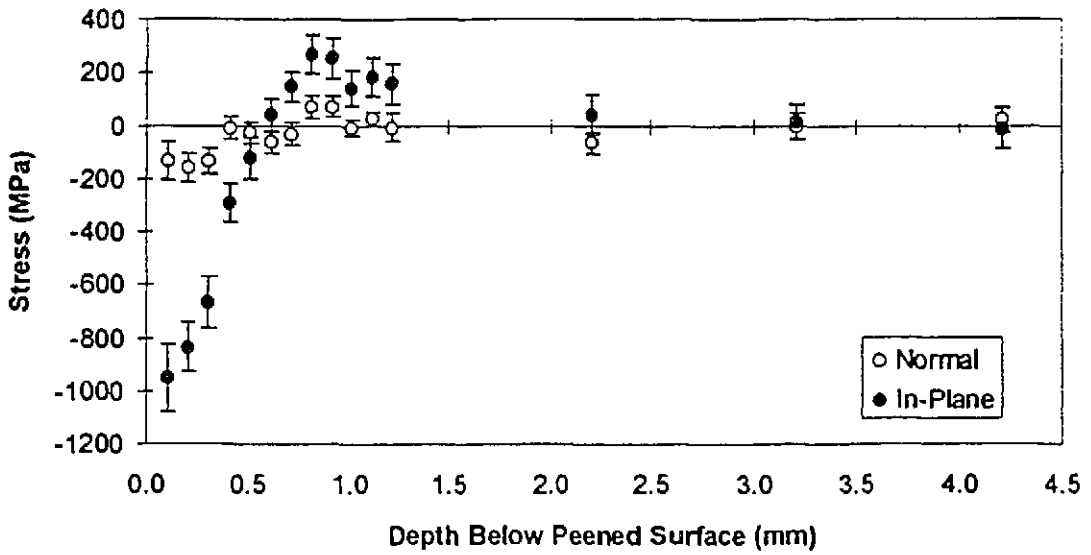

Fig. 2.3.1.41 Measured stress distribution in heavy-peened WASPALOY.

2.3.1.45 **Diffraction Measurements of Linewidth in Plastically Deformed and Fatigued HY-80**

T.M. Holden and J.H. Fox *(AECL)*, J. Pineault and M. Brauss *(Proto Manufacturing)*

Non-destructive methods of measuring plastic deformation or fatigue damage in marine components which have been subjected to stresses beyond the yield point and cyclic loading, are of importance to estimates of remaining life in naval vessels. Plastic deformation affects the width of diffraction lines, partly because of the distribution of elastic strains left after deformation, and partly because of dislocation broadening. Measurements were made of the linewidth of the (110) diffraction peak of deformed HY-80 steels with a high resolution experimental configuration using 1.974 Å neutrons reflected from the (331) planes of a silicon monochromator at a take-off angle of 105°. The instrumental linewidth was 0.282 ± 0.003°. Standard "dogbone" shaped samples 4.9 mm thick, 25.4 mm wide and 190.5 mm long were machined from HY-80 stock, and the surfaces were electro-etched with a grid of circles along their length. The samples were plastically deformed by different amounts and the plastic strains were obtained from the dimensions of the deformed etch-patterns. The variation of intrinsic linewidth, Δ, with plastic strain, ε, from five different samples was described by an exponential function

$$\Delta = K\varepsilon^n$$

with K = 0.310 ± 0.007 deg. and n = 0.130 ± 0.008. It was noted, however, that a much more sensitive measure of plastic strain is given by the change in intensity of the (110) diffraction peak. This varied by 200%, compared with the 14% increase in linewidth. The variation of intensity with plastic strain is linear and given by

$$I = (8.1 \pm 0.6) \times 10^4 + (4.3 \pm 0.1) \times 10^5 \varepsilon.$$

Contrary to the observations for plastically deformed samples, there was no change in the linewidth or intensity of samples fatigued for a large number of cycles at a maximum stress of 550 MPa (which is 2% below the yield point of HY-80 steel).

2.3.1.46 Effects of Hot-Deformation Parameters on the Recrystallization Texture of Aluminum Alloy AA5182

M.A. Wells, I.V. Samarasekera, E.B. Hawbolt and J.K. Brimacombe *(University of British Columbia)*, D.J. Lloyd and G. Burger *(Alcan International)*, J.H. Root and W. Ferris *(AECL)*

The volume fractions of various texture components will influence the final properties of aluminum sheet in deep drawing applications such as can making. These volume fractions can be influenced by the parameters of the hot rolling process through which the sheet material is made, such as total strain, strain rate and temperature. Specimens that spanned a wide range of hot-deformation parameters were analyzed for texture with the E3 neutron diffractometer. They were subsequently isothermally heat treated at 400°C, to study the evolution of the texture during static recrystallization.

Using data from the study, a modified form of the Johnson-Mehl-Avrami (JMAK) equation was developed, to model how each of the individual texture components (V_i) appeared or disappeared after a certain length of isothermal annealing time (t), as shown below:

$$V_t = V_\infty - (V_\infty - V_0)\exp(-0.693(t / t_{0.5})^n)$$

where V_∞ is the volume fraction of the texture component after recrystallization is complete; V_0 is the volume fraction of the texture component in the as-deformed sample; $t_{0.5}$ is the time when $V_{0.5} = 0.5 | V_0 - V_\infty |$; and n is the JMAK exponent.

The effect of hot deformation parameters (strain, strain rate and temperature) on V_0, V_∞, $t_{0.5}$ and n for a given texture component was correlated by using a least squares fit to the data. This approach appeared reasonable as the experimental data fit the model well and simulation of a 4-stand industrial hot tandem mill produced final texture predictions which were similar to those measured in industry. In terms of the individual hot deformation parameters, the deformation temperature and total strain had a significant effect on the final recrystallization texture, whereas the strain rate did not.

2.3.1.47 Texture Relationships of Hydrides with the Metal Matrix in Zr-2.5Nb

P. Gangli *(McGill University)*, R.W.L. Fong and J.H. Root *(AECL)*

Historically, the preferred orientations of hydrides in zirconium alloys have been linked to the texture of the predominant α phase of the metal matrix. The habit plane of the hydrides has been found to be nearly parallel to the (0002) plane of the hexagonal close-packed metal. Therefore, efforts are underway to fabricate pressure tubes with favourable α-phase textures that suppress delayed hydride cracking.

Measurements with the E3 neutron diffractometer have provided a simultaneous analysis of the crystallographic texture of the α (hcp) and β (bcc) phases of the metal matrix in typical CANDU® pressure tube material. The material contained a high concentration of hydrides, (0.4 mol%) predominantly in the δ (fcc) phase, and the texture of the hydride phase was also measured. The metal phases exhibit textures that are typical of drawn or extruded hcp and bcc materials. The hydrides exhibit a texture that is typical of drawn fcc metals. This is surprising, because the hydrides are introduced by an electrolytic process long after the metal is deformed. However, it is reasonable that the hydrides have formed within the lattice of one or both of the parent metal phases, and thus would mirror the original drawn-metal texture. Indeed, the texture of the bcc β phase can be transformed to the texture of a corresponding fcc phase through the Kurdjumov-Sachs relationship. The resulting fcc texture is very similar to what is observed in the δ hydride. The β zirconium and δ hydride textures are qualitatively more similar than the α and δ textures, suggesting that the β phase may play a more important role in the formation of hydrides in these alloys.

2.3.1.48 Real-Time Study of Oxidation of Iron at 1200°C

H. Abuluwefa and R. Guthrie *(McGill University)*, J.H. Root, D.C. Tennant, J.A. Rollings, D.A. Doering, and L.E. McEwan *(AECL)*

At the high temperatures of steel casting, the reaction of the metal with oxygen creates a scale that is composed of a mixture of oxides. The rate of reaction and volume fractions of the various oxides (FeO, α-Fe_2O_3, β-Fe_2O_3, Fe_3O_4, etc.) is dependent on the reaction temperature and the concentration of oxygen in contact with the surface. A special "hostile-environment insert" was made for the vacuum furnace and allowed the introduction of gases with a controlled concentration of oxygen. The specimen was oxidized at 1200°C and diffraction patterns were acquired every 10 minutes for up to 3 hours, at which time there was an oxide scale on the specimen with thickness between 1 and 3 mm. The intensities of the diffraction peaks provided a measure of the growth rate of each oxide in the scale. The analysis of the patterns by the Rietveld profile refinement method is continuing.

2.3.1.49 Variation of the Lattice Parameter with Location in a Stainless-Steel Weldment

S. Spooner *(Oak Ridge National Laboratory)*, I.P. Swainson and J.H. Root *(AECL)*

The fusion zone of a stainless-steel weldment experiences high energy inputs and rapid cooling from the liquid phase through a high-temperature bcc phase (ferrite) to a low-temperature fcc phase (austenite). Some of the high-temperature phase remains at room temperature in the fusion zone, with volume fractions that depend on the cooling rate at a particular location. The lattice parameter of the majority phase also varies with position in the fusion zone, possibly because of phase-interaction stresses with the metastable phases, or because of unequal partitioning of alloy elements between the two phases.

The fusion zone of a 1/2"-thick stainless-steel multipass weld was sectioned into rectangular prisms of dimensions $3 \times 3 \times 20$ mm^3, with the long dimension parallel to the line of the weld. Because these specimens have been removed from the surrounding material of the weldment, they are assumed to be free from macroscopic residual stresses. The lattice parameter of the austenite is larger in the fusion zone than in the parent material. The highest value is found near the last pass of the weld, and corresponds to a lattice strain of $+2 \times 10^{-4}$. Clearly, the evaluation of residual stresses in weldments by neutron diffraction must take account of location-dependent shifts in stress-free lattice parameters to obtain stress maps of high accuracy. The diffraction pattern from each specimen was analyzed by Rietveld refinement to determine the volume fraction of ferrite as a function of location in the fusion zone. Within the last pass of the weld, this volume fraction was nearly 8%. Elsewhere in the fusion zone, the volume fraction of the ferrite phase was typically 4%.

2.3.1.50 Multiple Scattering and Wavelength Dependent Scattering in Steel Plates

T.C. Hsu, F. Marsiglio, J.H. Root and T.M. Holden *(AECL)*

The work reported initially in the previous progress report (PR-PHY7:2.3.1.33; AECL-11016) has been completed. In this work strain measurements using neutron diffraction were carried out on steel plates. Further measurements with better counting statistics were performed to verify the effect of wavelength-dependent scattering in thick steel plates. A long series of measurements also showed that multiple scattering was not a cause of aberrations in strain measurements on thick plates.

2.3.1.51 Retained Austenite Stability in TRIP Steels

A. Di Chiro, A. Zarei-Hanzaki and S. Yue *(McGill University)* and J.H. Root *(AECL)*

TRIP steels contain a small volume fraction of a metastable austenitic phase that transforms during plastic deformation. The transformation process greatly improves the toughness of the material. The DUALSPEC powder diffractometer has provided the first direct evidence that the metastable phase disappears throughout the bulk of a specimen upon application of a large compressive strain. At intermediate strains, partial transformation is observed. The rate of

transformation with plastic strain is also observed to depend on the composition of the TRIP steel. These demonstration measurements have stimulated a thesis project, on the dependence of transformation-induced plasticity on strain, composition and microstructure.

2.3.1.52 Deformation Properties of a Two-Phase Magnesium Alloy

M. Gharghouri, G.C. Weatherly and J.D. Embury *(McMaster University)*, J.H. Root, M. Montaigne, L.E. McEwan and D.C. Tennant *(AECL)*

A magnesium alloy that contained about 10% of a hardening precipitate ($Mg_{17}Al_{12}$) was subjected to applied loads by the ATS stress rig on the L3 neutron diffractometer. The load was distributed unequally amongst magnesium grains of different orientations with respect to the stress axis. Also, the load was shared unequally between the matrix and the precipitates. At each value of applied load, a selection of diffraction peaks was measured in each phase. The peaks were fit by a gaussian function to determine the mean scattering angie, as well as the integrated intensity and full-width at half maximum. The total macroscopic strain was monitored by an extensometer, while the applied load was monitored by a load cell. The load-cycle went first into compression (maximum -130 MPa), then into tension (maximum +190 MPa), then to zero.

Two kinks in the macroscopic stress-strain curve correspond to loads where there is a dramatic change in the intensity of the (0002) diffraction peak, indicating that the deformation mechanism involves twinning of the magnesium matrix. The residual strain in the matrix at completion of the load cycle is slightly compressive, about -3×10^{-4}, while the residual strain in the precipitates is tensile, about $+13 \times 10^{-4}$. The peak widths in the precipitates increase at an applied load of +190 MPa, suggesting that the precipitates develop high concentrations of lattice defects at high loads. The detailed information provided *in situ* by neutron diffraction is valuable input for models that describe the deformation behaviour of polycrystalline aggregates.

2.3.1.53 Measurements of the Anisotropy of Magnetic Domain Orientations in Motor Core Steel

M. Birsan and J. Szpunar *(McGill University)*, J.H. Root, Z. Tun, L.E. McEwan, H.C. Spenceley, M. Montaigne and M.M. Potter *(AECL)*

A series of experiments were completed to demonstrate the feasibility of measuring the statistical distribution of magnetic domain orientations in polycrystalline materials, by neutron diffraction. Preliminary tests were made with an unpolarized neutron beam at the E3 diffractometer, equipped with the Eulerian cradle that is typically used for the analysis of crystallographic texture. The specimen was held between two ferritic steel rods that reached across the diameter of the χ-circle. The rods were cores within electromagnetic coils through which a variable current was passed to generate an applied magnetic field parallel to the η-axis of the cradle. Specimens were either fine-grained steel rod, with a cylindrically-symmetric crystallographic texture, or the coarse-grained, so-called "non-oriented" steel that can be applied in some electric motor applications. There is a coupling between the magnetization, **M**, of a magnetic domain and the scattered intensity, expressed by the factor $\mathbf{Q} \times (\mathbf{M} \times \mathbf{Q})$. Even though the E3 neutron beam was unpolarized, differences in the $\mathbf{Q} = (110)$ diffraction peak intensity were observed as the magnetic

field was increased. However, the changes of intensity expected in an unpolarized experiment are small because the intensities are dominated by nuclear scattering.

To better separate the "magnetic" portion of the (110) diffraction peak from the "nuclear" part, a polarized neutron beam is necessary. The DUALSPEC polarized triple axis spectrometer was configured to perform polarized-neutron texture measurements. This involved development of hardware and software to run the Eulerian cradle on C5, and to apply magnetic fields to the specimen, parallel to the η-axis. The specimen was a single strip of very coarse-grained Goss-oriented silicon steel, of the type produced by Dofasco for electric motor cores. A typical pole figure is shown in Fig. 2.3.1.42. The statistical fluctuations of intensity due to the coarse microstructure are clearly evident.

To retain the polarization of the incident neutron beam as it approached the specimen, large Helmholtz coils were affixed to the inside of the χ-circle. As the specimen was tilted, the applied field rotated from being parallel to the scattering vector to being perpendicular to the scattering plane. The Helmholtz coils followed the specimen tilt, and created a guide field parallel to the applied field at the specimen position, but smoothly turning to join with the magnetic fields of the beam-channel neutron guides, which ended just inside the diameter of the coils. By thus eliminating discontinuities in the guide field before and after scattering from the specimen, neutrons either entered the specimen with their spins parallel to the applied field or antiparallel to the applied field. The difference in the intensities of the pole figures between $\uparrow\uparrow$ and $\downarrow\downarrow$ scattering is dominated by magnetic scattering, while the sum of the two pole figures is dominated by nuclear scattering. The required separation of the two signals is therefore accomplished. The magnetic scattered intensity was obtained from the ratio $(\uparrow\uparrow - \downarrow\downarrow)/(\uparrow\uparrow + \downarrow\downarrow)$, where the denominator is needed to remove the effects of crystallographic texture on the measured magnetic intensity. The resulting magnetic intensity distribution is surprisingly smooth (Fig. 2.3.1.43), despite the fact that the denominator contains large statistical fluctuations arising from the coarse-grained microstructure of the specimen. Further development of an analysis procedure is needed now to derive the underlying distribution of magnetic domain directions from the measured magnetic scattering distribution.

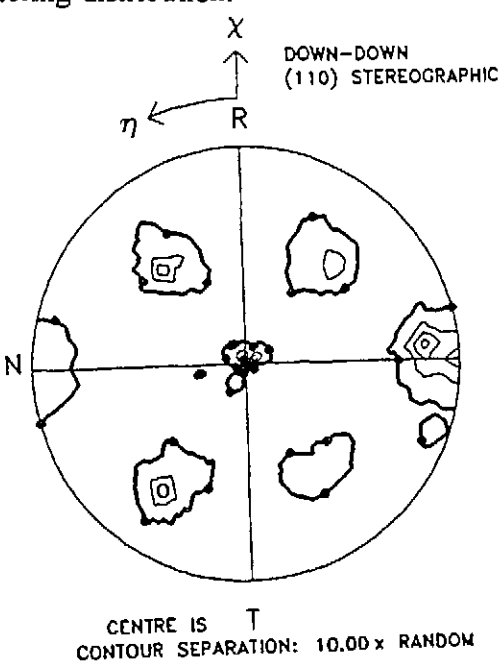

Fig. 2.3.1.42

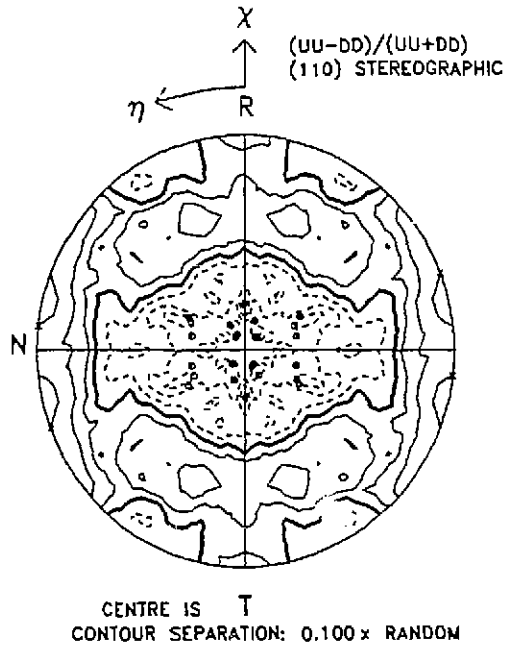

Fig. 2.3.1.43

2.3.1.54 Temperature Dependence of Neutron Diffraction in B2 NiAl Alloys

S.M. Kim *(AECL)*, M. Kogachi and Y. Takeda *(University of Osaka Prefecture)* and R.L. Donaberger *(McMaster University)*

Nearly stoichiometric NiAl is one of the promising candidate materials for high-temperature applications, due to their strength, high thermal conductivity and good corrosion resistance. The mechanical properties of these alloys, such as hardness and creep resistance, depend on the properties of vacancies and antisite defects. We have carried out neutron powder diffraction measurements on five Ni_xAl_{100-x} alloys (x = 47.7, 49.0, 50.0, 52.4 and 54.7) as a function of temperature from room temperature to 1400°C, in order to study these point defects. The measurements were made on the C2 DUALSPEC diffractometer located at the NRU reactor.

The data were first analysed assuming a uniform temperature factor, as is usually done in the analysis of the X-ray powder diffraction data at room temperature. A significant improvement in the fit, however, was obtained when different temperature factors were assigned for the atoms on the Ni sublattice and the Al sublattice. Because the minimum in the reliability factor R is not deep, it was necessary to vary the two temperature factors as well as the antisite concentrations manually, to obtain reproducible results. So far, the room temperature data for all the alloys have been analyzed together with the high-temperature data only for the stoichiometric alloy.

Taking into consideration previous lattice parameter and density measurements at room temperature in slowly cooled and quenched specimens, the following results were deduced from the room temperature data:

(1) In $Ni_{54.7}Al_{45.3}$ alloy, the Ni sublattice contains 1% Al antisite defects and the Al sublattice contains 5.7% Ni antisite defects.

(2) In $Ni_{52.4}Al_{47.6}$ alloy, the Ni sublattice contains no antisite defects and the Al sublattice contains 2.4% Ni antisite defects.

(3) In $Ni_{50}Al_{50}$ alloy, no antisite defects are present.

(4) In $Ni_{49}Al_{51}$ alloy, the Ni sublattice contains 2% vacancies and no antisite defects, and the Al sublattice contains no antisite defects or vacancies.

(5) In $Ni_{47.7}Al_{52.3}$ alloy, the Ni sublattice contains 3.6% vacancies and 1% Al antisite defects, and the Al sublattice contains 2% vacancies and no antisite defects. The estimated error limits are ± 0.2%.

Rietveld analysis of the high-temperature data for the $Ni_{50}Al_{50}$ alloy shows that no vacancies or antisite defects are present at temperatures below 1000°C. Above 1000°C, Al vacancies and Al antisite defects were observed to form. At 1400°C, the Al vacancy concentration reaches 2.6% and the Al antisite defect concentration reaches 0.9%. For many years it was believed that only Ni antisite defects and Ni vacancies form in NiAl alloys. The present neutron measurements are inconsistent with these expectations. It appears that since the lattice parameter increases from 2.8875 (1) Å at room temperature to 2.9457 (1) Å at 1380°C, the bond strength between two Ni atoms, which are smaller than the Al atoms, decreases, while that between the two Al atoms increases, as the temperature is increased. Thus above 1000°C, the bond strength between two Al atoms becomes stronger than that between two Ni atoms, resulting in the formation of vacancies on the Al sublattice.

2.3.1.55 Lattice Site Location of the Third Alloying Elements in the Binary $L1_2$ Ordered Alloys

S.M. Kim *(AECL)* and M. Kogachi *(University of Osaka Prefecture)*

Some years ago, Ochiai et al. (S. Ochiai, Y. Oya and T. Suzuki, Acta Metall. **32** (1984), 289) showed that, in adding a third component to an ordered binary alloy, such as Ni_3Al and Ni_3Ga, if the three interaction energies between the two atoms are known, it is possible to predict the sublattice where the third element will locate. The various interaction energies can be estimated using Miedema's semi-empirical formula for the alloy heat of formation (A.R. Miedema and P.F. de Chatel, in Theory of Alloy Phase Formation, edited by L.H. Bennet, p. 344 (1980), Metall. Soc. AIME). For an $L1_2$ phase A_3B ordered alloy, the alloy heat of formation is equal to three times the interaction energy v_{AB}.

We have applied this method to the $L1_2$ phase of Al_3TiX alloys where X is a transition metal, to test whether the theory correctly predicts the location of five alloying elements in Al-deficient Al_3TiX alloys (S.M. Kim, M. Kogachi, A. Kameyama and D.G. Morris, Proc. MRS 1994 Fall Meeting, to be published), as well as the location of Ni atoms in previously studied Ti-deficient $Al_{74.2}Ti_{19}Ni_{6.8}$. We have found that the formulation described by Ochiai et al. is in error, since they have compared total energies of two different alloys - alloys made with different starting

compositions. Wu et al. (Y.P. Wu, N.C. Tso, J.M. Sanchez and J.K. Tien, Acta Metall. **37** (1989), 2835) later corrected the errors made by Ochiai et al, but they also failed to note that there is a third region in the phase space spanned by v_{AC}/v_{AB} and v_{BC}/v_{AB} axes, where the third alloying elements form precipitates. Chiba et al. (A. Chiba, D. Shindoand, S. Hanada, Acta Metall. **39** (1991), 13) also derived conditions for the location of the third alloying elements, which is a hybrid between the original work of Ochiai et al. and the later revision by Wu et al.

Since several authors have tried to predict the location of the third alloying elements and have obtained incorrect results, we have carried out our own theoretical analysis. The results obtained for Al-deficient Al_3TiX alloys are shown in Fig. 2.3.1.44. The theory correctly predicts that all five alloying elements studied previously should locate on the Al sublattice. For Ti-deficient Al_3TiNi alloy, the theory also correctly predicts that the Ni atoms should occupy the Ti sublattice, as observed experimentally (P.R. Munroe and I. Baker, J. Mater. Res. **6** (1991), 943).

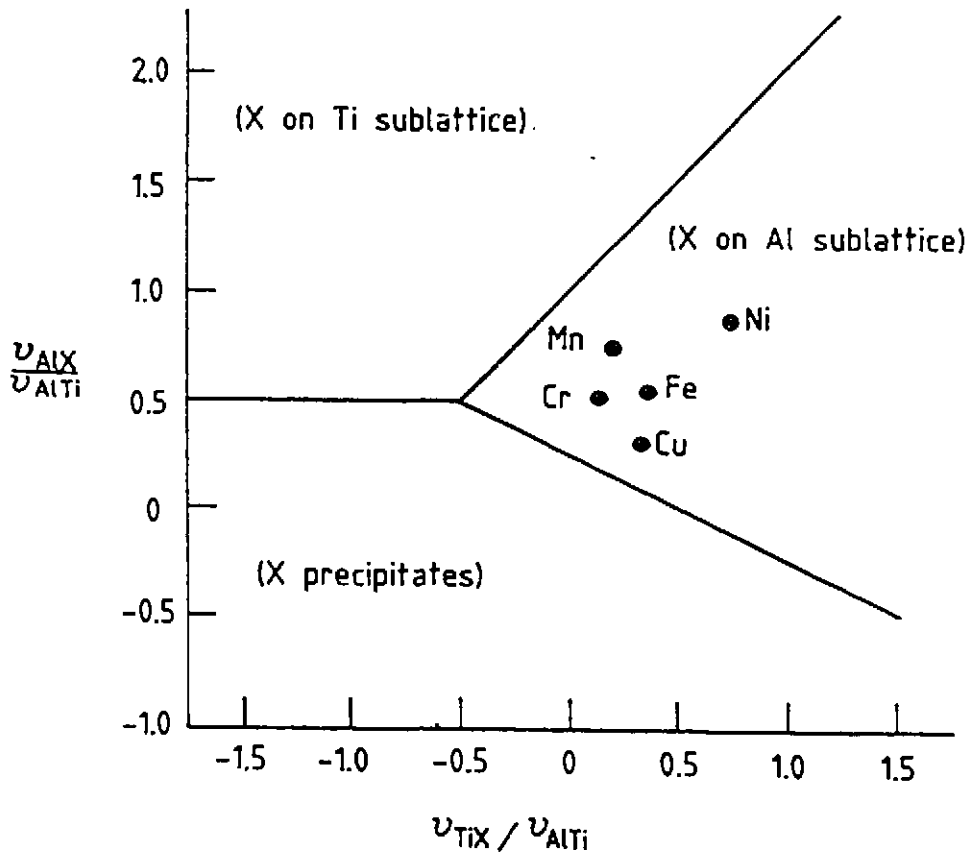

Fig. 2.3.1.44 The predicted lattice site location of the five alloying elements in Al_3TiX alloys.

2.3.1.56 **Accurate Measurement of α-Zr Lattice Parameters**

Z. Tun, J.H. Root and D.C. Tennant *(AECL)*

Accurate knowledge of α-Zr lattice parameters between room temperature and 850 K is of fundamental importance in understanding the behaviour of Zr-2.5Nb alloy for the CANDU®

industry. The information is required for modelling the residual stresses in extruded and annealed reactor pressure tubes.

Room temperature lattice parameters of an as-crystallized single-crystal specimen were obtained with the E3 spectrometer configured as a two-axis diffractometer. By calibrating the neutron wavelength against the standard Si powder from NIST, the hexagonal lattice parameters a and c of Zr were found to be 0.32340 (3) nm and 0.51479 (5) nm, respectively.

Lattice parameter measurements at elevated temperatures were made with a different crystal. This crystal was previously used for experiments at Risø and at CRL, but never subjected to temperatures > 850 K. There was a slight discoloration of this crystal, suggesting that it might have been contaminated with oxygen. However, the presence of an oxide contamination is not expected to affect the bulk lattice parameters. The sample was mounted inside the special spherical furnace (Ref: PR-PHY-7:2.3.4.2; AECL-11016), attached directly to the Eulerian cradle. At each experimental temperature, selected Bragg reflections were "centered" by rocking through angles χ and η to maximize the intensity, followed by a θ-2θ scan to determine the lattice parameter. Centering scans and the θ-2θ scan were repeated until the mean value of 2θ converged typically to within $\pm 0.005°$. The lattice parameter c was determined from (002) and (004) reflections, while (100), (110) and (200) were measured for the parameter a.

Plots of thermal strain for c and a, defined with respect to the values measured at 307 K, are shown in Fig. 2.3.1.45. Both lattice parameters are seen to vary linearly with temperature. The linear behaviour of c contradicts the generally accepted results (J. Goldak, L.T. Lloyd and C.S. Barrett, Phys. Rev. **144** (1966), 478). The thermal expansion coefficients deduced from the slopes of the best-fit lines in Fig. 2.3.1.46 are

$$\alpha_a = 5.4(1) \times 10^{-6}/\mathrm{K}$$

$$\alpha_c = 10.1(2) \times 10^{-6}/\mathrm{K}$$

A second series of measurements were made with the same setup, but with an automatic centering algorithm, where the center of a peak is located by the center-of-mass method, instead of fitting a Gaussian. The thermal expansion coefficients thus obtained are

$$\alpha_a = 5.8(1) \times 10^{-6}/\mathrm{K}$$

$$\alpha_c = 10.3(4) \times 10^{-6}/\mathrm{K}$$

The above values of α_a and α_c can be compared to the results of S.R. MacEwen, C. Torne and J. Faber (Acta Metall. **37** (1989), 979) for a "single grain" of Zircaloy-2. The a axis coefficient is in reasonable agreement, but our values of c axis coefficient are significantly smaller. It is not clear why our conventional diffraction technique and the time-of-flight technique employed by MacEwen et al. give agreement for one crystal direction but not for the other. However, the current data set fills in the interesting region between 300 and 600 K, proving that α_c (T) is a constant.

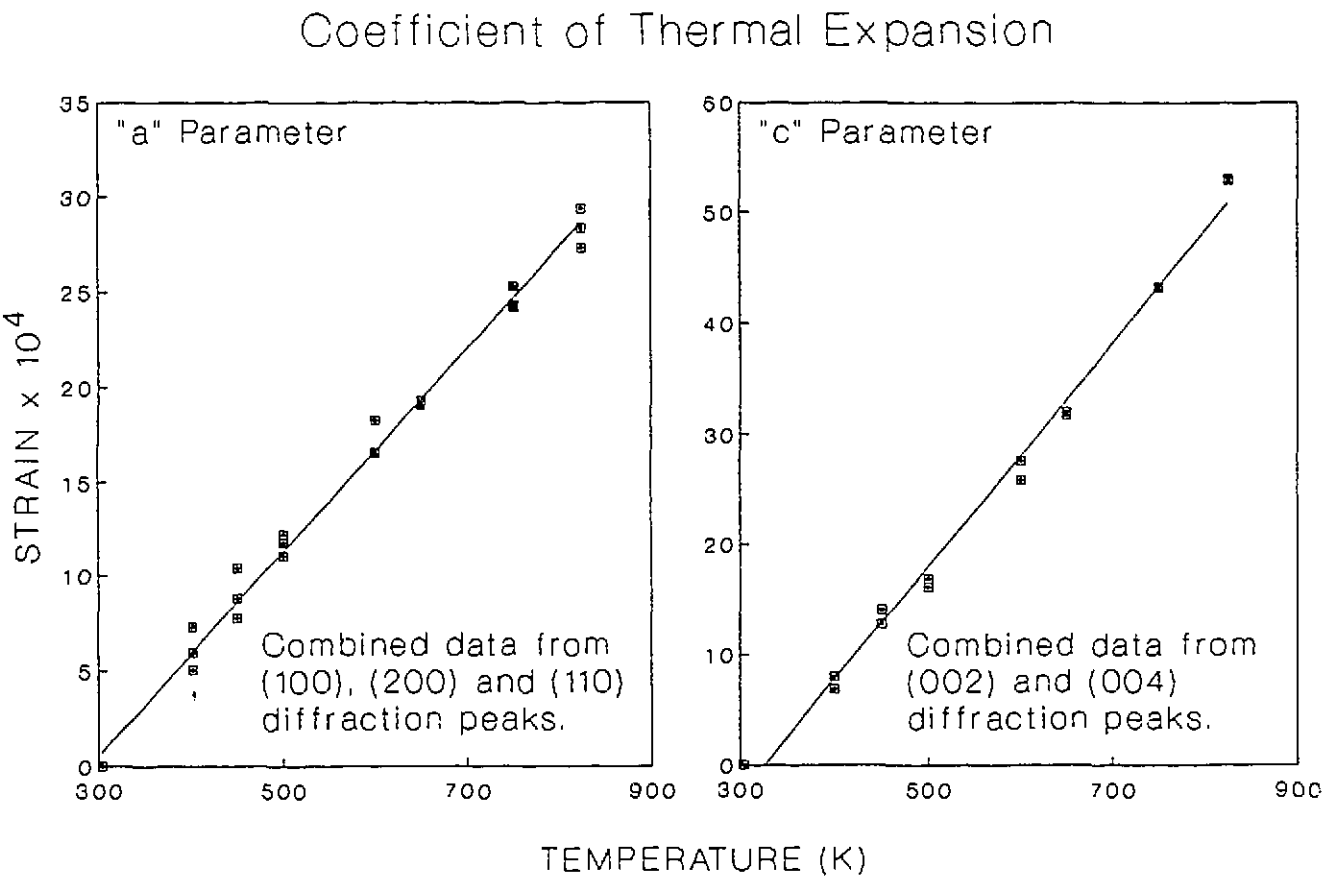

Fig. 2.3.1.45

Theory

2.3.1.57 **Small Moments in Heavy Fermions: A Model Hamiltonian**

A.E. Sikkema and J. Gan *(University of British Columbia)*, W.J.L. Buyers *(University of British Columbia; AECL)* and I. Affleck *(University of British Columbia; Canadian Institute for Advanced Research)*

We have examined a model Hamiltonian for the heavy-fermion compound URu_2Si_2, based on two crystal-field-split singlets for the uranium spin coupled by on-site exchange to the conduction electrons. It is equivalent to an Ising-Kondo lattice with transverse magnetic field. Within the mean-field approximation, we find a logarithmic response of the conduction electrons to moment formation. Over an appreciable range of parameters, the moments in the antiferromagnetic state are anomalously small as observed, and a reasonable Néel temperature is obtained. The model

also gives a qualitatively correct temperature-dependence, but not magnitude, of the specific heat, and we find that the majority of the specific heat jump at the Néel temperature arises from the formation of a spin gap in the conduction electron spectrum.

2.3.1.58 Neutron Scattering Lengths and Cross Sections

V.F. Sears *(AECL)*

For the past ten years, we have been maintaining a database of the best current values of the bound coherent and incoherent scattering lengths, and of the corresponding scattering and absorption cross sections, of the elements and their isotopes. The most recently published versions of these tables are in Neutron News **3** (1992), 26 and in Vol. C of the International Tables for Crystallography (Kluwer, Dordrecht, 1992). Even though both versions were published in 1992, there are numerous differences in the values, because the manuscript for the one in the International Tables for Crystallography was submitted in 1986 and many new values have been reported in the intervening years. A second edition of Vol. C is planned for 1996, and we have further updated these tables with new values for titanium and manganese for inclusion in this new edition. This most recent version will also be included in a new edition of Kohlrausch's "Praktische Physik" — a popular German handbook — in a section that is being edited by R. Scherm.

2.3.1.59 Correction of Neutron Scattering Lengths for Electromagnetic Interactions

V.F. Sears *(AECL)*

The scattering of thermal neutrons by a non-magnetic material is due almost entirely to the strong interaction between the neutrons and the nuclei of the atoms in the system. In a magnetic material, the magnetic dipole interaction between the neutrons and the magnetic electrons gives a contribution to the scattering that is comparable in magnitude to that from the nuclear interaction. However, even in non-magnetic materials, there is an electromagnetic interaction between the neutrons and the atoms which depends on the atomic form factor $f(q)$ ($\hbar q$ being the momentum transfer), and gives a q-dependence to the effective bound coherent scattering length of an atom which, while small (typically 1% or so), is nonetheless important in many kinds of experiments. We have developed two simple methods to correct for this effect that are adequate for most purposes.

For a neutral atom with atomic number Z, the effective bound coherent scattering length is of the form

$$b_c(q) = b_c(0) - b_e Z[1 - f(q)], \tag{1}$$

where $b_c(0)$ and b_e are constants, and the atomic form factor $f(q)$ is the Fourier transform of the electron number density in the atom and is normalized such that $f(0) = 1$. The quantity $b_c(0)$ is the bound coherent scattering length that determines the index of refraction for neutrons. This

is the quantity that is accurately measured in neutron optical experiments and is listed in tables of neutron data. The second term in Eq. (1) describes the interaction of the neutron with the electric field of the atom, and b_e is the neutron-electron scattering length. This term is mainly due to a relativistic quantum effect, the Foldy interaction between the neutron magnetic dipole moment and the electric field, but also includes a small contribution from the intrinsic charge distribution of the neutron.

The most accurate atomic form factors available today are those given in the International Tables for Crystallography, which are based on relativistic Hartree-Fock calculations and are tabulated for all the atoms and chemically important ions in the periodic table. The ad hoc expression (V.F. Sears, Phys. Rep. **141** (1986), 281)

$$f(q)=\frac{1}{\sqrt{1+3(q/q_0)^2}}, \tag{2}$$

where $q_0 = \gamma Z^{1/3}$ is the half width of $f(q)$ and $\gamma = 1.90 \pm 0.07$ Å^{-1}, provides an approximate fit to the Hartree-Fock results for all $Z \geq 20$, and is accurate enough for calculating $b_c(q)$ in most cases. Alternatively, the Thomas-Fermi model (see the following report), can be used for which $f(q)$ is, rigorously, a universal function of $qZ^{-1/3}$.

Fig. 2.3.1.46 shows the $b_c(q)$ curves for lead (Z = 82) that we have calculated using three different models for the atomic form factor $f(q)$: the Hartree-Fock approximation, the Thomas-Fermi model, and the ad hoc model (2). The calculations were performed with $b_c(0) = 9.405(3)$ fm and $b_e = 1.32(4) \times 10^{-3}$ fm, and the error bars show the uncertainty in $b_c(q)$ that arises from the errors in $b_c(0)$ and b_e. The Hartree-Fock result is the most accurate of the three, but it is clear that, for many practical purposes, either of the other more convenient models could be used instead.

In the past, experimenters have tended to ignore the correction of coherent scattering lengths for electromagnetic interactions. This was certainly justified in the early days of neutron scattering, when the experimental uncertainty in $b_c(0)$ was much larger than the value of b_eZ. However, except for some of the lighter elements, this is no longer true today, and this correction should be made routinely in all experiments where an accurate determination of the scattered-neutron intensity over a wide range of q values is important. The Thomas-Fermi model and the ad hoc model (2) provide two simple ways of making this correction, either of which will be adequate in most cases.

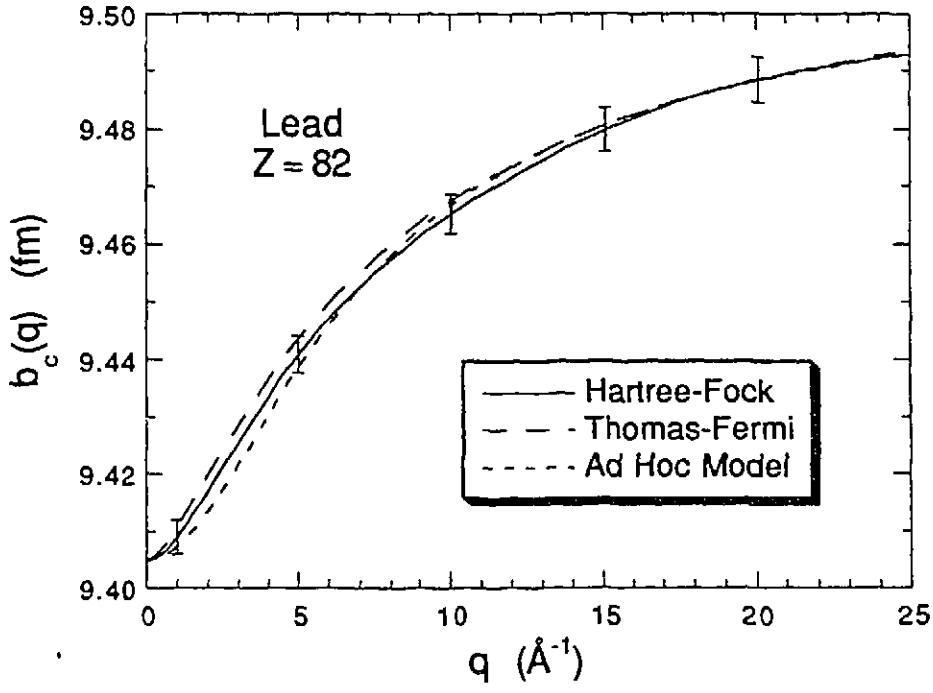

Fig. 2.3.1.46 Bound coherent scattering length of lead, as a function of q, calculated from Eq. (1) using three different models for the atomic form factor $f(q)$. The error bars show the uncertainty in $b_c(q)$ that arises from the errors in $b_c(0)$ and b_e.

2.3.1.60 **Atomic Form Factors in the Thomas-Fermi Approximation**

V.F. Sears *(AECL)*

The Thomas-Fermi model of the atom has a Z-scaling property that makes it very convenient for many applications, and it continues to find uses in areas where high accuracy is not required (see previous report). Existing numerical solutions of the Thomas-Fermi equation for a neutral atom all date from the period 1927 to 1935 and, with one exception, were performed manually. We have obtained a new solution of this equation, correct to six decimal places, using modern computing facilities and the program Mathematica. By Fourier transforming this solution we have also obtained the atomic form factor $f(q)$ correct to four decimal places. Bragg and West had calculated the atomic form factor $f(q)$ in 1929 from the numerical solution of the Thomas-Fermi equation given by Thomas in his original paper in 1927. All subsequent tabulations of the atomic form factor for a neutral atom in the Thomas-Fermi theory have been taken either directly or indirectly from Bragg and West's paper. All the early work mentioned above agrees, to within about 1%, with our more accurate results.

The advantage of using the Thomas-Fermi model lies in the fact that $f(q)$ is then a universal function of $qZ^{-1/3}$, so that you need only store a single table of $f(q)$ values in your computer, rather than 92 such tables. Fig. 2.3.1.47 compares the atomic form factors $f(q)$ as a function of

$qZ^{-1/3}$ for the Hartree-Fock approximation (shown for the values Z = 20, 25, ...90), the Thomas-Fermi model, and the ad hoc model (2) in the previous report. The Hartree-Fock results are seen to be in approximate agreement, not only with the above Z-scaling law, but also with the other two models. More precisely, we see that the Thomas-Fermi model is in good average agreement with the Hartree-Fock results for $qZ^{-1/3} > 4$ Å^{-1}, but is slightly lower than the Hartree-Fock results below about 2 Å^{-1}. In contrast, the results for the ad hoc model lie slightly above those for the Hartree-Fock approximation below 2 Å^{-1} and above 6 Å^{-1}.

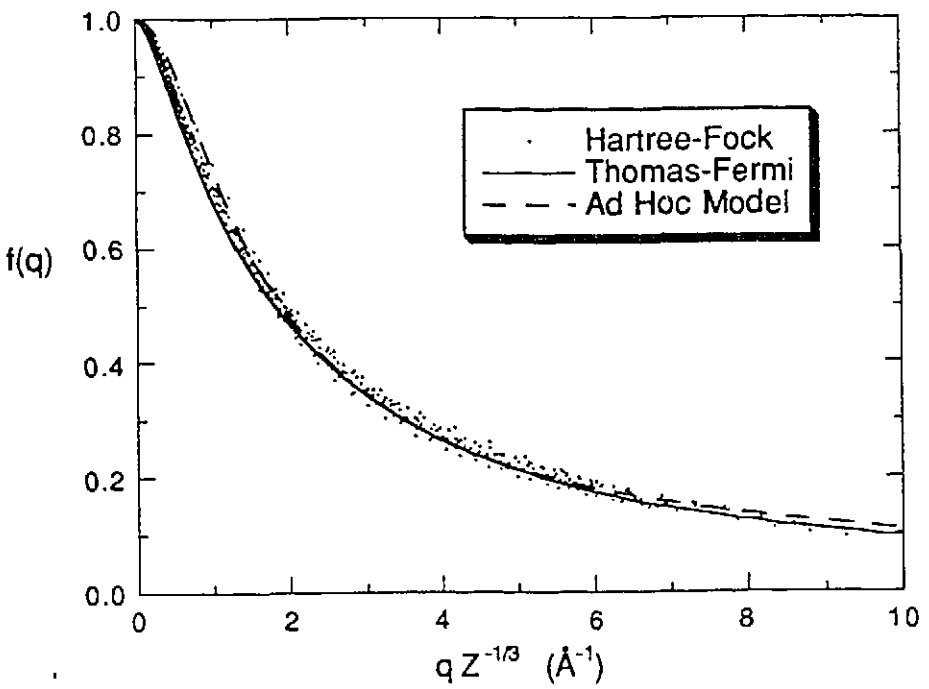

Fig. 2.3.1.47 Comparison of the atomic form factors $f(q)$ as a function of $qZ^{-1/3}$ for the Hartree-Fock approximation (shown for the values Z = 20, 25, ... 90), the Thomas-Fermi model, and the ad hoc model.

2.3.1.61 **Polaron Properties of the Holstein Model of Electron-Ion Interactions**

F. Marsiglio *(AECL)*

The following progress has been made on continuing work on the polaron properties of the Holstein model of electron-ion interactions:

i) We have implemented a Lanzcos algorithm for diagonalizing large matrices. Such an algorithm "filters" out low-lying eigenvalues (and eigenstates) by repeated application of the matrix (stored in advance). Whereas matrices of order 400 X 400 could be diagonalized previously, we now routinely diagonalize matrices of order 100,000 X 100,000. This permits us to explore the strongly polaronic regime, i.e. where

the phonon frequency is low and the electron-ion coupling strength is large. Calculations with larger system sizes are also possible, and work on two-dimensional lattices has commenced. All of this work is carried out in momentum space, so that block diagonalization can be done, by taking advantage of translational invariance. We have also performed (necessarily bigger) calculations in real space, where the role of impurities can also be studied. We find that in the strong-coupling regime, only a very small degree of impurity is required to localize the electron in the lattice.

ii) We have utilized weak coupling and strong coupling expansions, using perturbation theory from either the independent itinerant electron plus ion state (weak coupling) or the localized electron state (strong coupling). The latter is easily achieved by first using the Lang-Firsov transformation to decouple the electrons and ions to first order. We have found that the strong coupling perturbation calculation reproduces the exact results over a wide range of coupling strengths. This is fortunate, since this expansion can easily be carried out for an infinite lattice.

iii) We have used the "adiabatic" or "Born-Oppenheimer" approximation, where the ions are treated as being very slow compared to the electrons ($\omega_E << t$). This approach also simplifies the calculation. The agreement with exact results is very good for $\omega_E \lesssim 0.5t$. This approach thus constitutes a good description of the polaron in the physical regime ($\omega_E << t$).

iv) The three types of calculation outlined above have been extended to the case of two electrons, and (instantaneous) Coulomb interactions have also been included. In this way we have been able to study the competition between the electron-electron attraction (mediated by the ions) with the direct electron-electron repulsion. Because of the retardation of the attractive interaction, pair binding (i.e., superconductivity) is possible even in systems where the direct Coulomb repulsion exceeds the ion-induced attraction. We have also studied the isotope effect on the pair binding, and have found an inverse isotope effect (the binding *decreases* with increasing ion frequency). These and other properties will help to decide if this phonon mechanism is a viable possibility for the high-temperature superconducting oxides.

2.3.1.62 Investigation of the Labbé-Friedel-Barisic Model of Electron-Ion Interactions

F. Marsiglio *(AECL)*

As ions vibrate in a metal, the distance between neighbouring electron orbitals is modulated. Thus, modes of vibrating ions (i.e., phonons) couple to electrons in a manner which is physically very different from the Holstein coupling described in the previous section. As yet, it is not known which type of coupling is more important for the high-temperature superconductors. We have written programs to perform exact diagonalizations, weak coupling perturbation expansions and adiabatic expansions for one electron. The latter calculations are especially important, since we have already found that finite size effects are much more significant in this model. It is hoped that a comparison of properties in the two models can make an unambiguous choice between them.

2.3.1.63 Tight-Binding Calculation of the Upper Critical Field (H_{C2}) in the High-Temperature Superconductors

F. Marsiglio *(AECL)* and J.E. Hirsch *(University of California, San Diego)*

One of the interesting experimental facts in some of the high-temperature superconductors is that the measured upper critical field, H_{C2}, exhibits positive curvature as a function of temperature, in contrast to the conventional theory of Werthamer, Helfand, and Hohenberg (WHH) (Phys. Rev. **147** (1966), 295) where only negative curvature is predicted (and observed in conventional superconductors). We have carried out tight-binding calculations for a negative Hubbard model and found that well away from half-filling, the WHH theory is reproduced to a high degree of accuracy. At half-filling, however, a van Hove singularity is present in the electron density of states, and we find that H_{C2} has positive curvature, in agreement with experiment. Further analysis is required to determine what electron density range around half-filling yields positive curvature.

2.3.1.64 The Microwave Conductivity of Niobium

F. Marsiglio *(AECL)*, J.P. Carbotte *(McMaster University)*, R. Akis *(Concordia University)*, D. Achkir and M. Poirier *(Université de Sherbrooke)*

High-precision microwave measurements have recently been carried out on superconducting Nb samples (Phys. Rev. B **50** (1994), 7203). A BCS-like coherence peak has been observed below T_c. We find that a strong coupling (Eliashberg) calculation of the microwave conductivity, using electron-phonon spectral functions obtained from tunneling measurements, is unable to account for the height of the peak. All known modifications to the theory reduce the calculated peak height, so the observed peak height remains anomalous.

Calculations have also been carried out to explain how the height of the coherence peak measured by microwave measurements at lower frequency can be used to provide information about the low-frequency part of the electron-phonon spectral function and the associated inelastic scattering rate.

2.3.1.65 The S=½ Heisenberg Quantum Spin Chain and Quantum Affine Symmetries

M. Couture *(AECL)*

In the last two years, important new results on the S=½ Heisenberg quantum spin chain have been obtained by a group of mathematicians from Kyoto: B. Davies, O. Foda, M. Jimbo, T. Wiwa and A. Nakayashiki (Comm. Math. Phys. **151** (1993), 89). They have proposed a new, non-perturbative, approach for solving the Heisenberg chain which is totally independent of the Bethe Ansatz. They have shown that, in the thermodynamic limit (infinite chain), the quantum affine algebra sl(2) is an exact symmetry of the Hamiltonian. This result is central to their approach. Exploiting representation theory, the diagonalization of the Hamiltonian and evaluation of correlation functions are done in the thermodynamic limit. The use of the representation theory of the quantum affine sl(2) to describe the state of the system makes the concept of a

spinon very clear. These new developments are important and, following additional work which is being carried out here, this new theory should be experimentally verifiable.

2.3.1.66 A Braided Version of the S=½ Heisenberg Chain

M. Couture *(AECL)*

Several lattice models of condensed matter systems can be solved non-perturbatively in the framework of Yang-Baxter algebras (YBA). The S=½ Heisenberg quantum spin chain is an example of such a system. In this approach, known as the quantum inverse scattering method (QISM), to each system corresponds a particular YBA and the Hamiltonian of the model is just an element of that algebra. These algebras are examples of a more general algebraic structure known as Hopt algebra. Recently, it has been shown that Hopt algebras may be defined in the more general framework of braided spaces. Elements of these algebras obey statistics which are more general than the usual Bose-Fermi statistics. These are known as braid statistics. This raises the possibility of defining a braided version of the YBA's and thus of the QISM. The concept of braided spaces is very new in theoretical physics. The purpose of this project is to explore its meaning by using the Heisenberg chain as a test case. Significant progress has been made towards a braided formulation of the QISM. The YBA of the Heisenberg chain has been transformed, using Majid's transmutation theory, into one satisfying braid statistics. The braided Hamiltonian has been diagonalized and a modified set of Bethe equations were obtained. Their solution, in the thermodynamic limit, remains an open problem. The concept of hermiticity, in the context of braided spaces, must be defined.

2.3.1.67 New Examples of Braided Hopt Algebras and Majid's Transmutation Theory

M. Couture *(AECL)*

In a previous work on the underlying mathematical structure of a class of solvable models of two-dimensional statistical mechanics (which includes the S=½ Heisenberg chain), we had found new examples of braided Hopt algebras. Certain properties of these algebras needed further investigation. Work on a braided formulation of the general linear group and its q-deformed version has been completed. We discuss this example in the context of the general theory of braided Hopt algebras recently formulated by S. Majid (Math. Proc. Comb. Phil. Soc. **113** (1993), 45). The case of super algebras is now being investigated. This work has allowed us to clarify the role Majid's transmutation theory could play in formulating a braided version of the QISM.

2.3.2 Neutrino Physics

2.3.2.1 ^{232}Th in SNO Material by NAA

E.D. Earle and E. Gaudette *(AECL)*

The levels of Th contamination in materials planned for the SNO detector continued to be measured by gamma-ray analysis of neutron activated samples. Monitoring of acrylic handled by Reynolds Polymer Technology (RPT) included Th measurements on thermoformed, sanded,

polished and bonded material. Levels of Th are below the SNO specifications (2 pg/g) and therefore acceptable but, in some cases, the levels are significantly (a factor of 5) higher than obtained for the virgin acrylic. Some Th is being introduced, particularly during the thermoforming process, and steps have been taken to improve cleanliness at RPT. No significant increase in Th is observed following sanding and polishing. While the Th concentration in the bonds is higher than in the bulk acrylic, the total bond volume in the vessel is very low and so the increase in total Th inventory is not substantial.

Samples of kevlar fibre and ropes to be used to support the acrylic vessel contain ^{232}Th and ^{238}U below 200 pg/g, acceptable to SNO. The kevlar to acrylic mass ratio in the detector is much less than 100.

2.3.2.2 D_2O Test Facility

E.D. Earle and R.J.E. Deal *(AECL)*

A water purification plant has been constructed and installed. It consists of two, 1 Mg capacity, polyethylene tanks between which water can be transferred through filters. The filters can be removed and checked for contaminants, particularly Th and U decay chain daughters. Operating procedures have been written. After the tanks receive a final cleaning, the system will be commissioned with H_2O. Eventually, 1 Mg of D_2O obtained from the Bruce Heavy-Water Plant will be delivered to the plant for measurements.

2.3.2.3 A Production Plant to Produce MnO_2 Coated Beads

E.D. Earle, E. Gaudette, and M.M. Choi *(AECL)*

During operation the SNO laboratory will require up to 10 kg/wk of MnO_2 coated acrylic beads as part of the purification and assaying of the light and heavy water. A production plant, operating in a batch mode, to coat beads with MnO_2 has been designed in Chemical Engineering Branch and a 1/5 size prototype plant has been built and the design principles checked. The object of the full-scale plant is to replace the labour-intensive methods currently being used to produce these beads with a one man-day per week method, a manpower saving of about 80%.

The prototype plant is currently producing beads for the SNO project. The construction of the full-scale plant awaits completion of additional R & D work on the beads at CRPP, Ottawa.

2.3.2.4 Radon Cryodetectors

B. Sur, E. Gaudette and R.J.E. Deal *(AECL)*, and E. Bonvin and A. Hamer *(Queen's University)*

The SNO water group commissioned five cryo-detector systems in the fall of 1993. These cryo-detectors will be used for detecting very small quantities (a few atoms) of radon gas, emanated from MnO_2 columns which have been exposed to a few tonnes of ultra-pure H_2O or D_2O. The

counts, together with the known efficiencies and backgrounds from the detector system and the column, will quantify the radium (and thus the "bottom of the chain") contamination of the assayed water.

Since the commissioning, the cryo group has worked towards making the transition of the cryo-system from an experimental device to an integrated, semi-automated instrument, capable of routine, repeatable and stable operation. To this end a prototype system has been developed, procured, assembled and operated at CRL.

The heart of the cryo-detector system is the cryo-cell. It is a 1 cm^3 liquid nitrogen-cooled vacuum cell, with 50% wall coverage provided by silicon PIN diode detectors. Individual radon atoms can be cryo-trapped, and their α-decays detected in the silicon diodes with good energy resolution and timing information. We are now using a fifth-generation device. The indium vacuum seal on the PIN diode detector surface is made by deforming a 0.020" wire seated in a precisely machined stainless-steel middle layer, with welded pre-formed thin-walled stainless-steel inlet and outlet tubes. We are currently using 300 micron thick, 20 mm × 10 mm active area, bare PIN photo-diodes manufactured by Hamamatsu. The cryo-cell in the prototype system is mounted on the side-looking cold finger of a 30 liter liquid nitrogen dewar. A gas recirculation loop, with pure nitrogen gas at 30 torr pressure, carries emanated radon atoms from the MnO_2 column to the cryo-cell. An intermediate cold trap at 130 K intercepts other emanated species, such as water vapor, which would otherwise freeze in the cryo-cell and degrade its energy resolution. The loop is completed by connecting the outlet of the cryo-cell to the MnO_2 column via an ultra-clean sealed recirculation pump.

Most of the components for the five production systems have been developed and procured. We now have three fully assembled cryotrap systems, and the rest are close to completion. Remaining problems are (a) the air-leak rate in the present diaphragm recirculating pump (leading to an injection of about ten ^{222}Rn atoms per day into the system); and (b) drying of the porous acrylic beads of the MnO_2 filters to a level sufficient to avoid overloading the water trap in the loop. Meanwhile, further uses of the cryodetector system in the SNO experiment have been identified. These are (a) quality control (cleanliness) of plastic piping before installation in the water systems, (b) large-scale experiments to study the plate-out characteristics of uranium and thorium decay chain contaminants on plastic pipe surfaces.

2.3.2.5 Gas Transport Calibration System for SNO

B. Sur, E.D. Earle, K. Murghanan, E. Gaudette, R.J.E. Deal, V.T. Koslowsky and E.G. Hagberg *(AECL)* and E.B. Norman, *(Lawrence Berkeley Laboratory)*

A system to produce and deliver short-lived radioactivities for calibrating the SNO detector has been developed. Radioactivities are to be produced utilizing a small 14 MeV neutron D-T generator, which is located about 50 m away from the detector. The activities will be rapidly transported to a decay chamber inside the detector by a laminar gas stream flowing through a capillary tube. The following calibration sources have been proposed: (a) ^{16}N ($t_{1/2}$ = 7.13 s, 6.13 MeV γ-ray source) made by $^{16}O(n,p)$ and using O_2 gas as both target and gas stream; (b)

^{8}Li ($t_{1/2}$ = 0.84 s, β's with a 13 MeV endpoint) made as recoils from $^{11}B(n,\alpha)$ and transported by aerosols in a He stream; and (c) ^{17}N ($t_{1/2}$ = 4.4 s, β-delayed neutron source) made by $^{17}O(n,p)$ using $^{17}O_2$ gas in a recirculating loop.

All three calibration schemes have been successfully tested at the D-T generator facility of the Health Physics Branch. Production rates and delivery efficiencies have been measured and found to be adequate for use in SNO. As a result of the ^{17}N test, our measurement of the $^{17}O(n,p)$ cross-section has removed a previous discrepancy in the literature. The design and operating parameters (i.e., dimensions, flow rates, gas pressures, etc.) of the systems have been optimized. The D-T generator of choice has been identified and will be procured. The goal is to have a fully functional calibration system in SNO by the fall of 1995.

2.3.2.6 SNOMAN

B. Sur, E.D. Earle and M.M. Potter *(AECL)*

SNOMAN is the collective name for the "official" data simulation and analysis software for SNO. Our group has joined the software group within the SNO collaboration, and as a first step we have installed and successfully run a development version of SNOMAN on VMS. In order to further our participation, the SNO Institute has funded a large part of a new DEC Alpha computer for NCMS branch, as well as deputing a SNO Research Associate to work on data acquisition and analysis with our group at Chalk River.

2.3.3 Nuclear Data and Modelling

2.3.3.1 Temperature Coefficient of Radiative Neutron Capture Cross Sections

M.A. Lone, P.Y. Wong and P.J. Laughton *(AECL)*

For continued enhancement of CANDU®, advanced fuel concepts are being investigated for reduction of void coefficient and enhancement of negative temperature coefficient. One advanced fuel concept is to use a mixture of high-temperature coefficient absorbent materials in a slightly enriched uranium (SEU) fuel, to enhance the negative temperature coefficient of reactivity.

For a systematic investigation of suitable absorbent materials, the temperature coefficients were calculated with the aid of NJOY and WIMS-AECL codes. A total of eleven candidate materials were selected based on the presence of resonances at epithermal neutron energies near the upper edge of the thermal-neutron energy range.

Temperature-dependent point-wise neutron cross sections were generated at 296, 450, 600, 900, 1500 and 2400 K with the NJOY code using the ENDF /B-6 data libraries. These cross sections were binned in various energy groups using weighting factors computed from a neutron flux spectral distribution calculated for a heavy-water moderator temperature of 70°C.

The calculated temperature coefficients for various energy bins over the temperature range 20 to 2100°C are listed in Table 2.3.3.1. The ^{113}Cd and ^{176}Lu isotopes have the highest temperature

coefficient for the dominant thermal energy neutron group. The radiative capture cross sections for this energy group are plotted in Fig. 2.3.3.1.

Practical considerations require optimization of life-cycle burnup of fuel constituents. This would hinder the usefulness of ^{113}Cd, and ^{176}Lu would be a better choice.

Table 2.3.3.1 Temperature coefficient of neutron capture cross section (ppm/°C). (temperature range 20-2100 K)

Element	0.001 - 0.5 eV	0.5 - 1 eV	1 - 10 eV	10 - 100 eV
^{103}Rh	3.21	41.3	-4.46	-0.053
^{113}Cd	21.6	10.4	3.42	-0.125
^{113}In	1.27	3.99	0.938	0.218
^{115}In	2.5	14.9	0.673	-0.32
^{123}Te	1.78	2.71	0.877	-0.184
^{167}Er	4.43	11.5	-0.045	-0.023
^{176}Lu	20.3	6.32	3.99	-7.05
^{177}Hf	2.03	136	-13.2	-0.099
^{230}Th	1.24	7.86	0.52	-0.172
^{237}Np	-0.187	42.4	3.17	-5.54
^{240}Pu	2.14	24.2	-75.1	-0.184

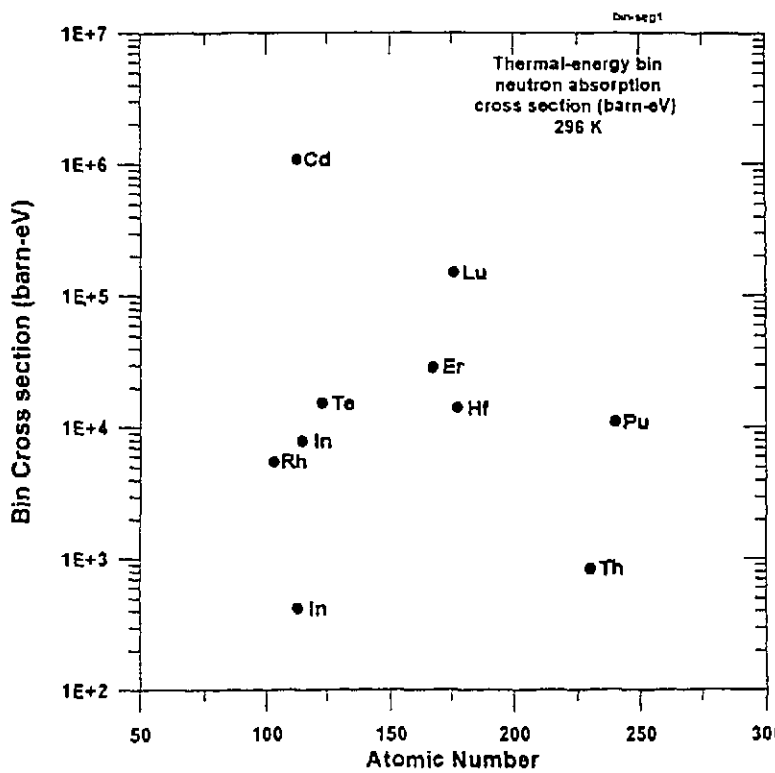

Fig. 2.3.3.1

2.3.3.2 Bremsstrahlung Converter Studies for Multi-Mode IMPELA Concept Design

M.A. Lone and P.Y. Wong *(AECL)*

For the concept design of multi-mode operation of the Irradiation Materials Processing Electron Linear Accelerator (IMPELA), characteristics of secondary electron and photon radiation were investigated for medium Z Fe and high Z Ta materials. These data are needed for the evaluation of optimum configurations of a high-power bremsstrahlung converter for radiation processing with direct electrons or photons of energy range between 5 and 10 MeV.

Angular and spectral distributions of bremsstrahlung and electrons from bombardment of converter assemblies with 5 and 10 MeV electrons were computed with the Monte Carlo code ITS. Four configurations, displayed schematically in Fig. 2.3.3.2, were studied. Results are summarized in Table 2.3.3.2.

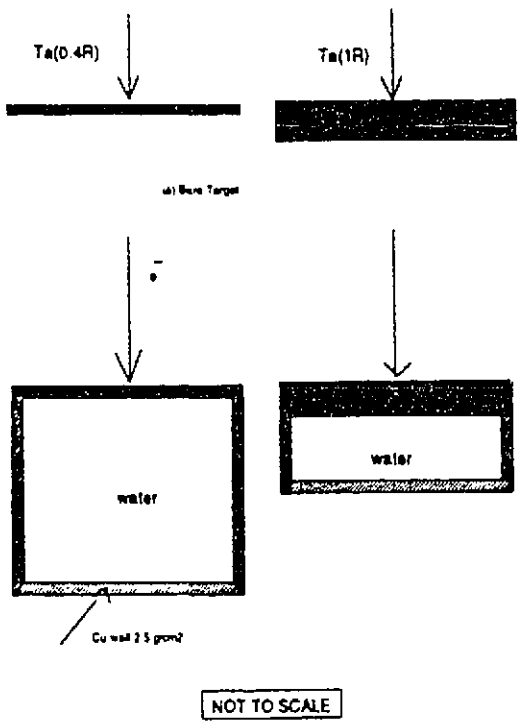

Fig. 2.3.3.2

Electron Beam Energy	10 MeV				10 MeV				5 MeV				5 MeV			
Configuration	Bare Converter				Cooled Converter				Bare Converter				Cooled Converter			
Converter material	Ta	Ta	Fe	Fe	Ta	Ta	Fe	Fe	Ta	Ta	Fe	Fe	Ta	Ta	Fe	Fe
Converter thickness	1R	0.4R	1R	0.4R	1R	0.4R	1R	0.4R	1R	0.4R	1R	0.4R	1R	0.4R	1R	0.4R
A. Forward Bremsstrahlung																
No. of forward photons (photons/source)	0.95	1.32	0.99	1.12	0.86	0.92	0.77	0.68	0.38	0.57	0.40	0.47	0.33	0.37	0.29	0.25
Total photon energy (MeV/source)	1.50	1.81	1.05	1.10	1.36	1.31	0.91	0.78	0.40	0.48	0.25	0.28	0.33	0.32	0.20	0.18
Average photon energy (MeV/photon)	1.57	1.37	1.06	0.98	1.59	1.42	1.17	1.15	1.05	0.84	0.64	0.60	1.00	0.86	0.70	0.71
Efficiency (%)	15.0	18.1	10.5	11.0	13.6	13.1	9.1	7.8	8.0	9.6	5.0	5.6	6.6	6.4	4.0	3.6
B. Backscattered Electrons																
No. of backward electrons (electrons/source)	0.13	0.13	0.035	0.036	0.13	0.13	0.034	0.032	0.24	0.24	0.083	0.078	0.24	0.25	0.081	0.081
Total electron energy (MeV/source)	0.49	0.50	0.075	0.086	0.48	0.48	0.077	0.070	0.61	0.61	0.14	0.013	0.59	0.63	0.14	0.14
Average electron energy (MeV/electron)	3.83	3.83	2.16	2.41	3.78	3.82	2.27	2.22	2.53	2.53	1.70	1.67	2.47	2.57	1.69	1.72
C. Backward Bremsstrahlung																
No. of backward photons (photons/source)	0.44	0.35	0.27	0.20	0.45	0.38	0.29	0.29	0.29	0.27	0.15	0.14	0.31	0.29	0.17	0.19
Total photon energy (MeV/source)	0.41	0.35	0.12	0.10	0.42	0.35	0.12	0.12	0.19	0.18	0.057	0.055	0.19	0.18	0.062	0.068
Average photon energy (MeV/photon)	0.93	1.00	0.46	0.50	0.94	0.91	0.43	0.42	0.65	0.65	0.37	0.40	0.61	0.63	0.36	0.35

* Ta(1R) and Fe(1R) include cooling of 0.6 g/cm2 of H2O and 2.5 g/cm2 Cu; Ta(0.4R) and Fe(0.6R) include 4 g/cm2 H2O nd 2.5 g/cm2 Cu where R = electron range.

Table 2.3.3.2

The bremsstrahlung yield from a high Z Ta is 1.5 times higher than that from a medium Z Fe converter. This is primarily due to the higher average photon energy from Ta. Because of the cooling needed for the high-power assemblies, there is little difference in the net yield of bremsstrahlung from an optimum and a full-range thick converter. The yield of back-scattered electron and backward bremsstrahlung from high Z Ta is a factor of 3 to 4 higher than from the medium Z Fe converter.

Further studies of the utilization efficiency of forward bremsstrahlung are in progress and the results, in conjunction with these data, will help in the optimization of converter design.

2.3.3.3 Fission ^{99}Mo Production with Aqueous Fuel Systems

M.A. Lone and P.Y. Wong *(AECL)*

Nuclear fission is the most prolific source of high specific activity ^{99}Mo, and the bulk of the current supply is produced by this process in a batch-mode method employing the irradiation of solid U-Al targets of 93% enriched ^{235}U, followed by dissolution in nitric acid and separation of ^{99}Mo by alumina chromatography.

We have investigated the dynamics of several concepts for the production of fission ^{99}Mo. These included methods based on accelerator-based subcritical or critical reactors, using batch-mode extraction from irradiation of a solid-target, or continuous-mode extraction from a homogeneous aqueous uranyl nitrate core reactor.

2.3.4 Instrumentation

2.3.4.1 Angular and Time Resolution of Neutron Time-of-Flight Spectrometers

E.C. Svensson *(AECL)*, R. Crevecoeur, I. de Schepper and L. de Graaf *(Delft University of Technology)*, W. Montfrooij *(Risø National Laboratory)* and C. Carlile *(Rutherford Appleton Laboratory)*

In our earlier study (PR-PHY-5:2.5.1.2; AECL-10775) of the multiexcitation scattering by superfluid ^{4}He using the IRIS time-of-flight (TOF) spectrometer at the ISIS spallation-neutron facility of the Rutherford Appleton Laboratory, we also measured the single-excitation scattering by the superfluid ^{4}He. During the analysis of the results of this study, we have realized that the single-excitation scattering by superfluid ^{4}He at low temperatures (where these excitations have negligibly small intrinsic widths) can be used to accurately determine both the angular resolution, $\Delta\phi$, and the time resolution, Δt, of a TOF spectrometer. While the energy resolution at zero energy transfer, ΔE_0, (which is related to Δt) of a TOF spectrometer can be determined readily by using an elastic incoherent scatterer such as solid vanadium, previously there has been no standard experimental procedure for determining $\Delta\phi$ (which is related to the wave-vector resolution Δq).

The frequencies, $\omega_s(q)$, of the single-excitation modes in superfluid ^{4}He obtained from our measurements on the IRIS spectrometer are shown in Fig. 2.3.4.1. The measurements were carried out at saturated vapor pressure (SVP) and T = 0.5 K, where the intrinsic widths of the modes are negligibly small compared to the energy resolution (ΔE_0 = 15 μeV [FWHM]) of the IRIS spectrometer. The solid curve in Fig. 2.3.4.1 represents a 7th-order polynomial fit to the dispersion relation, constrained to have the same slope as the velocity-of-sound line (dashed curve) in the limit $q \rightarrow 0$.

The widths (FWHM) of the single-excitation peaks observed in our measurements are shown in Fig. 2.3.4.2. Since the intrinsic widths are negligible, these widths directly reflect the combined effect of the true energy resolution of the spectrometer and the finite angular resolution (i.e., finite q resolution). The oscillatory behaviour exhibited by the observed widths is simply a result of the oscillating value of the modulus of the slope of the dispersion relation (Fig. 2.3.4.2) and the finite angular resolution of the instrument. The solid curve in Fig. 2.3.4.2 represents a best fit to the data of a model which uses slope values taken from the solid curve in Fig. 2.3.4.1, and in which $\Delta\phi$ and Δt are adjustable parameters. It gives a very good description, and the values (FWHM) $\Delta\phi$ = 0.118 rad (6.8°) and Δt = 212 μs. The two minima in Fig. 2.3.4.2 correspond to the positions where the dispersion relation has zero slope (i.e., to the well-known maxon and roton excitations in superfluid ^{4}He) (Fig. 2.3.4.1). The observed widths at these positions give values of the energy resolution of the spectrometer at the finite-energy transfers of the maxon and roton modes. As expected, these are somewhat larger than the value 15 μeV at zero energy transfer determined from measurements on vanadium, and they serve to establish experimentally the energy dependence of the energy resolution up to an energy transfer of 1.2 meV (the maxon energy).

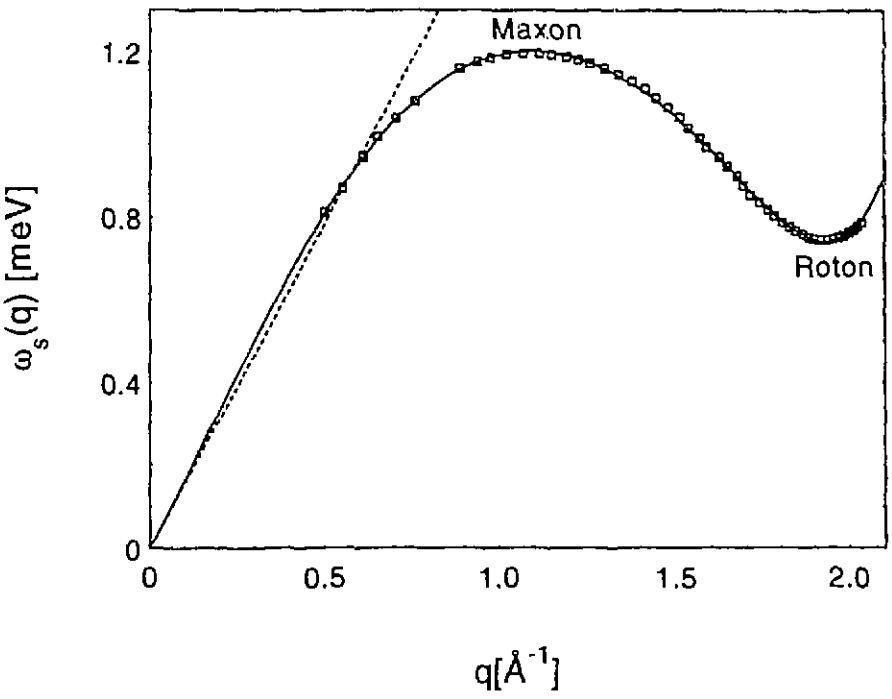

Fig. 2.3.4.1 The dispersion relation for superfluid ^{4}He at SVP and 0.5 K (see text).

For comparison with our measured value, we have estimated $\Delta\phi$ for the IRIS spectrometer from geometrical considerations (the divergence of the incident beam, the mosaic spread of the analyzers, and the spatial widths of various instrument components such as the neutron guide, the sample and the detectors), a complex and rather unreliable procedure. We obtain $\Delta\phi = 0.097$ rad, somewhat smaller and much more uncertain than the value $\Delta\phi = 0.118$ rad given by our measurements on superfluid ^{4}He. The contribution from the mosaic spread of the analyzers, which we estimate to be 0.084 rad, is the dominant contribution to the overall angular resolution of IRIS. The difficulty of estimating $\Delta\phi$ from the known geometry of the spectrometer shows the great advantage of having a technique that directly determines $\Delta\phi$ from experiment, such as the technique we have described above. While we used measurements at T = 0.5 K for our determination, the intrinsic widths of the excitations in superfluid ^{4}He increase sufficiently slowly with increasing T that our technique is generally applicable for T < 1.3 K.

This work has allowed us to explain the recent puzzling results of Blagoveshchenskii et al. (N.M. Blagoveshchenskii, I.V. Bogayavlenskii, L.V. Karnatsevich, Zh.A. Kozlov, V.G. Kolobrodov, A.V. Puchkov and A.N. Skomoroknov, JETP Lett. 57 (1993), 428) for superfluid ^{4}He. They are simply a consequence of the angular resolution of their TOF spectrometer, rather than being evidence for a previously unobserved intrinsic property of superfluid ^{4}He, as they had proposed. For many studies using TOF techniques, it is essential to know accurately the angular resolution of the spectrometer, and to understand in detail how this will affect the results obtained.

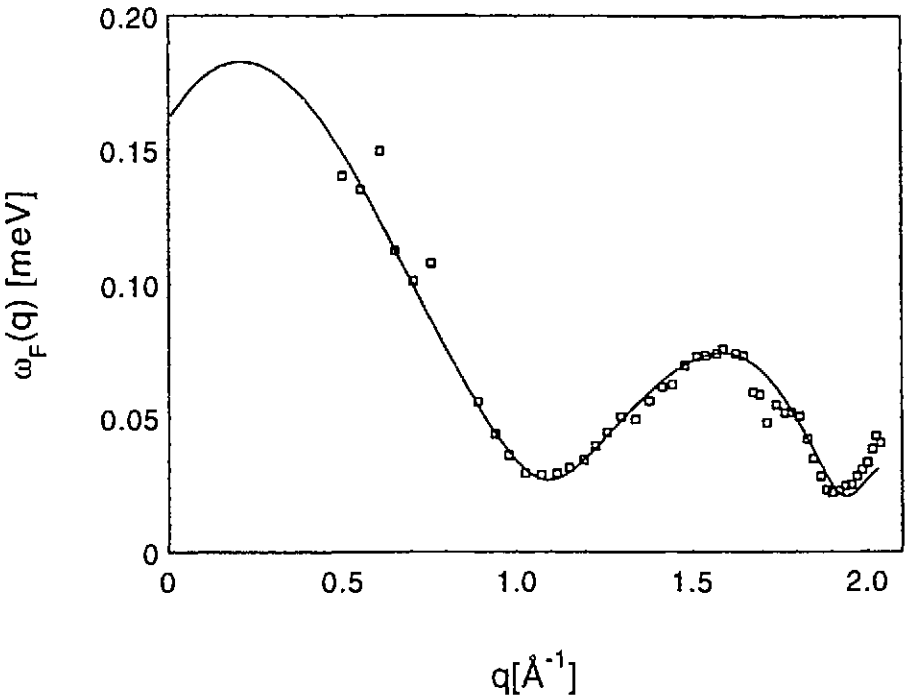

Fig. 2.3.4.2 The observed widths of the single-excitation peaks for superfluid ^{4}He at SVP and 0.5 K (squares). The solid curve shows the result of a least-squares fit to a model (see text).

2.3.4.2 The Small Angle Neutron Spectrometer, T3

J. Katsaras, D.C. Tennant, W.J.L. Buyers and J.A. Rollings *(AECL)*

The T3 Small Angle Neutron Spectrometer (SANS) has been redesigned in order to make it more suitable for the study of biologically relevant materials. The most drastic change to the spectrometer concerns the sample holder "assembly", which consists of the sample chamber, and two translation devices. The new sample chamber, for aligned multilayers, will be capable of maintaining a constant humidity and temperature, critical for the study of these systems. One translation along with one rotary device will be interfaced to a control computer, and will be menu driven to facilitate alignment of the sample with respect to the incident beam. A temperature-controlled sample holder has been designed for non-aligned samples. In addition, the neutron beam path extending 4.5 m from near the sample position to near the detector has been enclosed and the air replaced by helium. The absorption and scattering of helium at low angles is much less than air. At a scattering angle of 1° the use of helium has been observed to reduce the background by a factor of 7, from 350 to 50 counts/minute per degree. This result has led to a redesign of the incident beam channel in which air is replaced by vacuum. The changes described above will make the T3 SANS spectrometer internationally competitive in this area of research.

2.3.4.3 L-3 Spectrometer Jib Crane Proposal

J.H. Fox *(AECL)*

The L-3 neutron spectrometer has no hoisting capability above the sample table. Samples studied by the ANDI group are often heavy and require counterweighting by a balance beam suspended over the sample table. A one-ton capacity jib crane pivoting off the L or M face of the reactor biological shield is required. Two layout proposal drawings were produced and submitted to NRU Operations. The proposal is currently in Engineering and Design's Civil Section awaiting a detailed structural analysis.

2.3.4.4 ANDI Set-up Utilities for E3 and L3 Spectrometers

R.B. Rogge, J.H. Fox and L.E. McEwan *(AECL)*

The ANDI program requires precise centering of the sample on the sample table and precise alignment of the incident and scattered beam slits over this center in order to define the sampling volume. A requirement for robust, accurate and reproducible set-up utilities was identified. A stretched wire holder, pin holder, plate holder, stretched foil holder and cadmium mask on interchangeable tapered mounts were conceived, designed and manufactured. Their use has made the alignment procedure significantly faster and more accurate.

2.3.4.5 X-Y-Z Translation of Universal Test Machine (Stress Rig)

J.H. Fox and L.E. McEwan *(AECL)*

An experiment to study stress concentrations around a hole in a steel plate while under a tensile load required that the entire stress rig be translated in X, Y and Z directions. Rotation of the sample about its vertical axis was not required, allowing removal of the sample table at the N-5 spectrometer. The cavity thus created permitted the mounting of a low-profile elevating stage at the center of the scattering angle axis, directly on the monochromator platform. Custom mounting plates and hold-down clamps were designed and manufactured. An X-Y table assembled from two single axis stages was mounted atop the elevating stage via an adaptor plate. The rated load-carrying capacity of the X-Y-Z translators was 50 kg, requiring that the 200 kg stress rig be counterweighted using a balance beam suspended from the X-Y crane above the N-5 spectrometer.

2.3.4.6 Alignment of the C2 Si (531) Focussing Monochromator

I.P. Swainson *(AECL)*

The C2 focussing monochromator was aligned using the C5 spectrometer and a z-translator. Each of the elements was aligned both in the horizontal and vertical planes, with the use of slits placed in the incident and the diffracted beams. One element was found to be weakly reflecting and will be replaced in the future. The monochromator is now ready to use for C2 experiments.

2.3.4.7 Spectrometer Control System

M.M. Potter and M. Montaigne *(AECL)*

Software that enables users to control the spectrometer from off-site has been installed on nodes CM7 (C5 control), CM9 (C2 control) and CM19 (T3 control). The software, called CHALKTALK, is a product of Symark Software Inc. With CHALKTALK any off-site terminal can be made as the control console for a spectrometer. Users can monitor the progress of an experiment and change experimental parameters from off-site.

The scan mode known as E-mode, which is used to measure the sample texture with the Eulerian Cradle, has been added to the DUALSPEC control program.

An Emergency Stop module has been designed and installed on the DUALSPEC control system. The module has a front panel pushbutton and an input for a remote pushbutton, either of which will inhibit all the motors on the spectrometer when it is depressed momentarily. Although the main function of the module is to provide an emergency stop for all motors, it has front panel toggle switches to disable each motor individually. These toggle switches are used to protect equipment that would be damaged if a motor was driven inadvertently during an experiment.

The General Structure Analysis System program (GSAS) from Los Alamos has been installed on an Alpha computer at CRL. The program which is used to analyze data from the C2 powder diffractometer is very fast on the Alpha computer; therefore, it can be used in the on-line mode. This contrasts with the application on slower systems, where the jobs must be submitted to a batch queue.

2.3.4.8 DUALSPEC Beam Gate Control

M.M. Potter and W. Mellors *(AECL)*

The Beam Gate was controlled by optical switches triggered by vanes on the rotating gate. It has been found that the optical switches were damaged by radiation even after additional shielding had been added (PR-PHY-6:2.3.4.5; AECL 10878). New vanes and a switch pack made of miniature micro switches were designed and installed. The new system generates electrical codes identical to those of the optical switches; therefore, the Beam Gate Control did not need modifications.

2.3.4.9 Reactor Beam Hole Use

D.C. Tennant *(AECL)*

NRU operated for 276 days with an average power of 114.7 MW during the period of 1994, January 1 to December 31. Spectrometer use is given below (efficiency is % of available reactor operating time used for experiments).

Beam hole	No. of experiments	No. of participating CRL scientists	No. of participating non-CRL scientists	Efficiency
C2	34	11	24	88%
C5	11	6	14	93%
E3	27	7	20	98%
L3	17	6	11	97%
N5	13	7	14	98%

2.3.5 Support Services

2.3.5.1 Multiwire ^{3}He Neutron Detectors

G.A. Sims, J.J-P. Bolduc, D.C. Tennant, H.C. Spenceley and B.M. Powell *(AECL)*

This technical support group is responsible for the design, fabrication, testing and installation of multiwire detectors for the condensed matter science group. During the past year, the techniques used for constructing MWDs have undergone a rapid transformation. New materials of construction have made possible a number of improvements in detector fabrication. These have resulted in improved versatility and reliability, and these detectors are the most useful and efficient presently in service in the ANDI (Applied Neutron Diffraction for Industry) program.

The following is an update of the progress made and the present status of the various detectors under construction or completed.

1) 32-Wire Detectors (Grounded Anode)

a) MA-93-32-GA

This detector has passed extensive testing on the bench and at the NRU reactor. Its performance exceeds all expectations since it was installed in the L3 spectrometer (1994 April). It demonstrates that excellent progress has been made in the fabrication procedures, materials selection and that a sound, reliable design has been achieved.

Background noise measurements over a 52-hour period varied from 1.54 counts/hour to 0.68 counts/hour, with an average of ~ 1 per channel/hour.

b) MA-94-32-GA-B

This unit is identical to MA-93-32-GA, and has been completely assembled and bench tested. It also exhibits excellent operating characteristics and stable performance. The results of the noise background tests (66 h) are shown in Fig. 2.3.5.1.

The manufacturing techniques and design concepts of the 32 MWD have made this the most promising diagnostic tool specific to the needs of the ANDI group to date. It meets or exceeds all specifications and will replace the conventional 13-wire detectors now in service. The detector is scheduled to be installed in E3 at the NRU reactor by the end of 1994, to undergo further tests under experimental conditions.

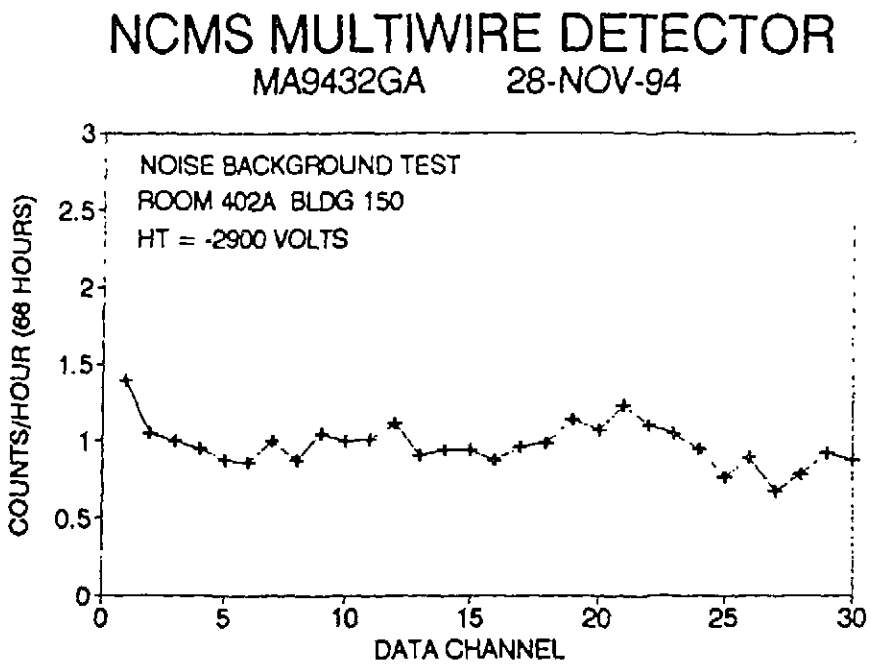

Fig. 2.3.5.1

c) MA-94-32-GA-A

This detector is also a twin to MA-93-32-GA, and incorporates the same mechanical and electronic components that have led to the success of this type of detector, both in the techniques employed in their construction and in their use in experiments. It is now in the process of being assembled. The value of this style of detector is increasing and has led to requests for additional units.

Vacuum and pressure tests, along with the appropriate bench tests, will be conducted early in 1995. Upon acceptance, it is planned to install this detector in N5 at the NRU reactor.

2) 13-Wire Detectors

a) MAC-1-9-13

This unit is used primarily as a bench mark for testing associated electronic components.

b) MA-2-9-13, MA-3-9-13

These detectors have been taken out of service and replaced by the 32-wire grounded anode detectors MA-93-32-GA. They have been in service since 1989 August, and their performance exceeded all expectations.

c) MS-1-8-13 (DC Grounded Anode Prototype)

This detector has been removed from L3 and at the present time is being shared between E3 and N5, as required.

2.3.5.2 Elastic Recoil "Backgammon Detector"

G.A. Sims, H.C. Spenceley and J.S. Forster *(AECL)*

Construction details, design modifications, experimental tests and operational data can be found in PR-TASCC-8:3.2.8; AECL-11132 and PR-TASCC- 9:3.1.30; AECL-11239.

2.3.5.3 Ge Detector Repairs

J.J-P. Bolduc *(AECL)*

Nine Ge detectors were serviced during the reporting period.

2.3.5.4 Electronic Communication Services for the Neutron Scattering Community: ANDInet and CINSnet

R.B. Rogge, T.M. Holden and W.J.L. Buyers *(AECL)*

Two electronic communications services have been established. They provide similar services, but the details of their use differ. For each there is a single electronic mail address (ANDInet@crl.aecl.ca and CINSnet@crl.aecl.ca), which is used to direct e-mail to all net members, and a shared anonymous ftp site, which provides abstract and information data bases.

The first system was set up for the Applied Neutron Diffraction for Industry (ANDI) group, and is known as ANDInet. By creating such a communication network, we position ourselves as an international "*nerve centre*" for applied neutron diffraction. Initial response to this network has

been positive and many invitations have been sent around the world by regular post to boost membership further. Early responses to this indicate a promising growth in the ANDInet subscription.

All members of the Canadian neutron scattering community are represented by the Canadian Institute for Neutron Scattering (CINS). The CINSnet has provided, in addition to the central e-mail address, a set of stable e-mail addresses for the executive members. As well, the ftp site makes available information on the facilities at CRL and at McMaster University, proposal forms, CINS information data bases, etc. Overall, CINSnet provides a convenient communication channel for open discussions of the many issues which face CINS (like the need for a new reactor to replace NRU). CINSnet was started in December and the initial response has been very positive.

2.3.5.5 **Mechanical Laboratories**

H.C. Spenceley and L.E. McEwan *(AECL)*

In Building 459 Mechanical Laboratory, the following work was completed. A new rotary beam gate switch package was designed, manufactured and installed on C2, C5 rotary gates.

The heavy link for C2 was manufactured off-site and is now installed. The new beam channel shielding components for C5 were machined in the workshops and are also being installed.

A small set of single directional slits (jaws) which fit down the diffracted beam channel for C5 were designed and manufactured and are now in use. A new set of dovetail clamps for C5 beam channel components were designed, built and installed. A more compact design for the C2, C5 instrument stacks has been developed and some of the required machining has been started. This should be completed in 1995.

Modifications were made to the jaws of the ANDI stress rig and adaptor plates, and clamps were made to hold the stress rig in different positions. Components were manufactured for the ANDI program, to be used as set-up tools for the spectrometer prior to an experiment. A set of tapered nose snounts were machined for use by ANDI.

A third large furnace has been started and will be commissioned in 1995.

Specimen environment equipment has been designed and built as part of the upgrade to the T3. A rotary table and X translator plus adaptor plates will be installed at the small-angle spectrometer T3 in 1995.

Other work completed in this period includes 32 vanadium cans for powder samples, 12 crystal mounts and 24 varied sample preparations and specimens for ANDI.

Work in Building 116 Mechanical Laboratory was divided as follows:

60% of the time was spent in fabricating detectors, two sets of the B.T.I. detectors, and two 32 multiwire detectors.

30% of the time was spent on work for Nuclear Physics Branch, including fabricating of the Accelerator Mass Spectrometry detector and the Backgammon detector (elastic recoil).

The remaining time was spent on several small jobs for SNO, jigs for holding glass and quartz for the Glassblowing Laboratory, and cutting of crystals with the diamond cutting tools.

2.3.5.6 Glassblowing Laboratory

D.A. Doering and P.A. Moss *(AECL)*

Major jobs completed during the period are listed below:

Chemical Operations

Two hundred and fifty-two alumina columns and fifty-five product recovery headers were made for the ^{99}Mo isotope-production facilities.

Two prototype quartz product recovery headers were fabricated.

Twelve small resin columns were modified to fit into the ^{90}Y extraction line.

Fuel Engineering

Twenty-five quartz glass baskets and six quartz portable oxygen sensors were fabricated to allow the branch to continue their research on new reactor fuels.

System Chemistry and Corrosion

Two hundred and three thin-walled NMR vials with #7 "O" ring joints were fabricated, to continue studies of irradiated water solutions.

Two new types of closed circulating systems were fabricated with a glass impeller enclosed, to collate results of irradiated water solutions, with Dr. J. LaVerne of Notre Dame University.

A platinum wire was sealed into a pyrex #9 "O" ring joint for experimental gas rack.

Physical Chemistry

Several quartz glass furance tubes were fabricated to recover ^{60}Co.

General Chemistry

Four pyrex cells were fabricated and a hole of diameter 0.004" and four other cells with a hole of diameter 0.007" drilled through the glass wall were fabricated. These small holes were drilled with the help of small drills from D. Weisenberg (Fuel Materials Branch).

Nuclear Physics

Three new water-cooled quartz aerosol generators were fabricated and four were repaired. They form an integral component of a gas transport system for the on-line isotope separator at TASCC.

Health Physics

In order to analyse for ^{239}Pu, much glassware was fabricated on a high-priority basis.

Fuel Channel Components

Thirty glass hooks were fabricated, to enable experimental data to be collected from fixed-end burst tests on calandria tubes removed from the Pickering reactor.

Chemical Engineering

Six quartz plasma tubes were fabricated with tangential entrances, and six were repaired. They allow experiments to continue on the decomposition of H_2S.

Two rectangular water cooled columns and two vapour phase reactor columns were fabricated.

Accelerator Physics

Forty-six quartz holders were made to measure high-temperature dielectric properties of various samples.

Environmental Research

Two electrolysis cells for an IAEA Romanian contract were constructed.

One hundred and thirty-two traps, eighteen quartz sample tubes, one hundred and eighty glass funnels and ten glass freezing traps were fabricated to conduct a controlled tritium release into the environment.

Fourteen 30 mL boiling flasks, sixteen 20 mL boiling flasks, twelve 75 mm bulbs, sixteen glass vials, sixteen 9 mm break seals and forty charcoal traps were all fabricated from Corning 1724 (aluminosilicate) glass, to allow long-term experiments in the studies of plant adsorption of ^{3}H gas.

A large glass cyclone was constructed for the SNO experiments.

Four seven-inch-diameter beakers were fabricated to clean parts needed for fabrication of detectors.

2.4 PUBLICATIONS AND LECTURES

Publications

β^+ DECAY AND COSMIC-RAY HALF-LIVES OF ^{143}Pm AND ^{144}Pm
M.M. Hindi, B. Sur, A.E. Champagne, M.T.F. da Cruz, R.-M. Larimer, K.T. Lesko and E.B. Norman
Phys. Rev. C **50** (1994), 728

SIGNALS, BACKGROUNDS AND CALIBRATIONS IN THE SUDBURY NEUTRINO OBSERVATORY
B. Sur
Proceedings of the 5th International Conference on the Intersections of Particle and Nuclear Physics, A.I.P. Conference Proceedings Series (1994)

LOW-FREQUENCY MODES IN AMORPHOUS ICE
E.C. Svensson, W. Montfrooij, V.F. Sears and D.D. Klug
Physica B **194-196** (1994), 409

EVIDENCE FOR SOFT-MODE BEHAVIOR OF THE ROTON AT HIGH DENSITY
W. Montfrooij and E.C. Svensson
Physica B **194-196** (1994), 521

LOW-FREQUENCY MODES IN HIGH-DENSITY AMORPHOUS ICE
D.D. Klug, E.C. Svensson, W. Montfrooij and V.F. Sears
AIP Conf. Proc. No. 309, Part 1, "High-Pressure Science and Technology-1993" (1994), 405

THE STRUCTURE OF PUMICE BY NEUTRON DIFFRACTION
M.A. Floriano, A.M. Venezia, G. Deganello, E.C. Svensson and J.H. Root
J. Appl. Cryst. **27** (1994), 271

ULTRA TRACE ANALYSIS OF ACRYLIC FOR ^{232}Th and ^{238}U DAUGHTERS
G.M. Milton, S.J. Kramer, R.J.E. Deal and E.D. Earle
Appl. Radiat. Isot. **45** (1994), 539

SUPERCONDUCTIVITY FROM RETARDED INTERACTIONS IN THE PRESENCE OF ELECTRON-HOLE ASYMMETRY
F.J. Marsiglio and J.E. Hirsch
Phys. Rev. B **49** (1994), 1366

SUPERCONDUCTIVITY FROM ELECTRON-PHONON INTERACTIONS IN THE ABSENCE OF ELECTRON-HOLE SYMMETRY
F. Marsiglio and J.E. Hirsch
Physica B **199-200** (1994), 338

ELIASHBERG TREATMENT OF THE MICROWAVE CONDUCTIVITY OF NIOBIUM
F. Marsiglio, J.P. Carbotte, R. Akis, D. Achkir and M. Poirier
Phys. Rev. B *(RC)* **50** (1994), 7203

POLARIZATION ANALYSIS OF MAGNONS IN $CsMnI_3$
Z. Tun and T.C. Hsu and J-G. Lussier
J. Appl. Phys. **75** (1994) 6063

MAGNETIC STRUCTURE OF THE SPIN-LIQUID STATE IN THE FRUSTRATED PYROCHLORE $CsNiCrF_6$
M.J. Harris, M.P. Zinkin, Z. Tun, B.M. Wanklyn and I.P. Swainson
Phys. Rev. Lett. **73** (1994), 189

MAGNETIC ORDER AND SPIN-FLOP TRANSITION IN Co-Re MULTILAYERS
Z. Tun, W.J.L. Buyers, I.P. Swainson, M. Sutton and R.W. Cochrane
J. Appl. Phys. **76** (1994), 7075

MAGNETISM OF SYNTHETIC AND NATURAL ANNITE MICA: GROUND STATE AND NATURE OF EXCITATIONS IN AN EXCHANGE-WISE TWO-DIMENSIONAL EASY-PLANE FERROMAGNET WITH DISORDER
I.A.D. Christie, G. Lamarche, I.P. Swainson and S. Flandrois
J. Magn. Magn. Mater. **138** (1994), 31

NEUTRON DIFFRACTION STUDY OF MAGNETIC PHASES IN POLYCRYSTALLINE Mn_2SiS_4
A.-M. Lamarche, G. Lamarche, C. Church, J.C. Woolley, I.P. Swainson and T.M. Holden
J. Magn. Magn. Mater. **137** (1994), 305

NON-DESTRUCTIVE ANALYSIS OF RESIDUAL STRESS AND TEXTURE IN MMCS BY NEUTRON DIFFRACTION
J.H. Root and H.J. Rack
In Recent Developments in Light Metals, Proc. Int. Symp. on Research and Development in Light Metals, M. Gilbert, P. Trembly, E. Ozberk eds., Metallurgical Society of CIM, Montreal (1994) p. 35

NEUTRON DIFFRACTION MEASUREMENTS OF TEXTURE IN SILICON CARBIDE WHISKER-REINFORCED ALUMINUM COMPOSITES
J.H. Root and H.J. Rack
Materials Science Forum **157-162** (1994), 1475

RESIDUAL STRESS CHARACTERIZATION OF FERRITIC WELDMENTS
J. Schröder, J.H. Root, T.M. Holden and M. Koçak
GKSS 93/E/82
Available from GKSS Forschumgszentrum Geesthacht GmbH, Max-Planck-Strape, D-21502, Geesthacht, Germany

ULTRASONIC CHARACTERIZATION OF TEXTURE IN PURE AND ALLOYED ZIRCONIUM
A. Moreau, P.J. Kelczynski, J.F. Bussière and J.H. Root
Nondestructive Characterization of Materials VI (1994) p. 119

SENSITIVITY OF SELF-POWERED DETECTOR PROBES TO ELECTRON AND GAMMA-RAY FIELDS
M.A. Lone, P.Y. Wong and K. Ajmani
Nuclear Instruments and Methods in Phys. Res. A **349** (1994), 563

ACCELERATOR NEUTRON SOURCES FOR RADIOSCOPY
M.A. Lone and B.G. Chidley
In Proc. Neutron Radiography System Design and Characterization, editors G.M. MacGillivray and J.S. Breceizer Jr., Canadian Nuclear Society, Toronto (1994), 23

DETAILS OF THE MAGNETIC PHASE DIAGRAM OF HOLMIUM FROM NEUTRON DIFFRACTION IN b-AXIS FIELDS
D.A. Tindall, C.P. Adams, M.O. Steinitz and T.M. Holden
J. Appl. Phys. **75** (1994), 6318

THE APPLICATION OF NEUTRON DIFFRACTION TO STRESS MAPPING AROUND A BLIND-HOLE DEFECT IN STRESSED PIPELINE STEEL
L. Clapham, T.W. Krause, H. Olsen, B. Ma, D.L. Atherton and T.M. Holden
J. of Stress Analysis **29** (1994), 317

NEUTRON DIFFRACTION INVESTIGATIONS OF INTERNAL STRESS IN MATERIALS
T.M. Holden
Nukleonika **39** (1994), 91

SPIN WAVE COLLAPSE AND INCOMMENSURATE FLUCTUATIONS IN URu_2Si_2
W.J.L. Buyers, Z. Tun, T. Petersen, T.E. Mason, J.-G. Lussier, B.D. Gaulin and A.A. Menovsky
Physica B **199-200** (1994), 95

THE TRANSITION IN THE HEAVY-FERMION SYSTEM URu_2Si_2: SPIN OR MULTIPOLAR?
M.B. Walker, Z. Tun, W.J.L. Buyers, A.A. Menovsky and W. Que
Physica B **199-200** (1994), 165

Reports

PRELIMINARY ESTIMATES OF NUCLEON FLUXES IN A WATER TARGET EXPOSED TO SOLAR-FLARE PROTONS: BRYNTRN VERSUS MONTE CARLO CODE
J.L. Shinn, J.W. Wilson, M.A. Lone, P.Y. Wong and R.C. Costen
NASA Technical Memorandum 4565 (1994)

SENSITIVITY OF SELF-POWERED DETECTOR (SPD) PROBE TO ELECTRON AND GAMMA RAY FIELDS
M.A. Lone and P.Y. Wong
Proc. 1994 Symp. Appl. Math.
RC-1221, CMS-94-02

^{17}N: A TAGGED NEUTRON SOURCE FOR SNO
E.B. Norman and B. Sur
SNO Scientific and Technical Report SNO-STR-94-037 (1994)

INTERIM REPORT ON THE SNO CRYO-DETECTORS
B. Sur, E. Bonvin, A. Hamer, R. Deal and E. Gaudette
SNO Scientific and Technical Report SNO-STR-94-059 (1994)

Lectures

NEW VISTAS IN MATERIALS SCIENCE THROUGH NEUTRON DIFFRACTION
J.H. Root
McGill University, Dept. of Mining and Metallurgical Engineering
1994 January 14

CRYSTALLOGRAPHIC TEXTURE
J.H. Root
Physics Department, Queen's University
1994 March 30

ORDER-DISORDER TRANSITION IN CALCITE ($CaCO_3$)
I.P. Swainson
Canadian Society for Chemistry Conference, Winnipeg, 1994 May 29 - June 2

SIGNALS, BACKGROUNDS AND CALIBRATIONS IN THE SUDBURY NEUTRINO OBSERVATORY
B. Sur
5th International Conference on the Intersections of Particle and Nuclear Physics,
St. Petersburg, Florida, 1994 June 1-6

EXACT CALCULATIONS FOR THE HOLSTEIN POLARON
F. Marsiglio
Workshop on Strongly Correlated Exotic Materials: Organic, Heavy Fermions and High Temperature Superconductors, Queen's University, 1994 June 6

HOW TO TELL A NEUTRINO FROM A HOLE IN THE GROUND
B. Sur
Colloquium to Triangle Universities Nuclear Laboratory, Duke University,
Durham, North Carolina, 1994 July 15

CRYSTALLOGRAPHIC TEXTURE ANALYSIS BY NEUTRON DIFFRACTION
J.H. Root
Summer Workshop on Neutrons in Materials Science, CRL
1994 August 18

ELECTRON-PHONON INTERACTIONS IN HIGH-T_c: PROGRESS REPORT ON THE HOLSTEIN MODEL
F. Marsiglio
VIIIth International Conference on Recent Progress in Many-Body Theories, Schloss Seggau, Austria, 1994 August 25

INDUSTRIAL APPLICATIONS AND NEUTRON DIFFRACTION
T.M. Holden
Frank Laboratory of Neutron Physics, Dubna
1994 September 20

CLUSTER STUDIES OF THE HOLSTEIN MODEL
F. Marsiglio
Workshop of the Institute for Scientific Exchange, Torino, Italy, 1994 September 29

ANSWERS TO INDUSTRIAL QUESTIONS BY NEUTRON DIFFRACTION
J.H. Root
Materials Week - 1994 October 2-6
Rosemont, Illinois

RESIDUAL STRESS AND TEXTURE: THE FINGERPRINTS OF EXTRUSION
S.R. MacEwen, A. Langille, J. Savoie and J.H. Root
Materials Week - 1994 October 2-6
Rosemont, Illinois

APPLIED PHYSICS RESEARCH WITH THERMAL NEUTRONS
T.M. Holden
Saclay, France
1994 October 3

TOWARDS A PHASE DIAGRAM FOR THE HOLSTEIN MODEL
F. Marsiglio
Euroconference on: Cross-Over Phenomena in Solid State Physics, Torino, Italy, 1994 October 4

INDUSTRIAL APPLICATION OF NEUTRON DIFFRACTION
T.M. Holden
University of Reims at Charleville-Meziers
1994 October 4

CRYSTALLOGRAPHIC TEXTURE ANALYSIS BY NEUTRON DIFFRACTION
J.H. Root
Physics Department, Dalhousie University
1994 October 19

GAS TRANSPORT CALIBRATION SOURCES FOR THE SUDBURY NEUTRINO OBSERVATORY DETECTOR
B. Sur
Annual Meeting of the Division of Nuclear Physics, American Physical Society, Williamsburg, Virginia, 1994 October 26 - 29

APPLIED NEUTRON DIFFRACTION PROGRAM
J.H. Root
University of Toronto Materials Institute
1994 November 29

Cat. No. /No de cat.: CC2-11234E
ISBN 0-660-16249-0
ISSN 0067-0367

To identify individual documents in the series, we have assigned an AECL- number to each.

Please refer to the AECL- number when requesting additional copies of this document from:

Scientific Document Distribution Office (SDDO)
AECL
Chalk River, Ontario
Canada K0J 1J0

Fax: (613) 584-1745 Tel.: (613) 584-3311
ext. 4623

Price: C

Pour identifier les rapports individuels faisant partie de cette serie, nous avons affecté un numéro AECL- à chacun d'eux.

Veuillez indiquer le numéro AECL- lorsque vous demandez d'autres exemplaires de ce rapport au:

Service de Distribution des Documents Officiels
EACL
Chalk River (Ontario)
Canada K0J 1J0

Fax: (613) 584-1745 Tél.: (613) 584-3311
poste 4623

Prix: C